PACKAGING TECHNOLOGIES FOR MILLIMETER SCALE MICROSYSTEMS IN HARSH ENVIRONMENT APPLICATIONS

by

Yushu Ma

A dissertation submitted in partial fulfillment
of the requirements for the degree of
Doctor of Philosophy
(Mechanical Engineering)
in the University of Michigan

2016

Doctoral Committee:

Professor Yogesh B. Gianchandani, Co-Chair
Assistant Research Scientist Tao Li, Co-Chair
Professor Wei Lu
Professor Khalil Najafi

ACKNOWLEDGEMENTS

I want to express my deepest gratitude to my advisor Prof. Yogesh Gianchandani. His tremendous enthusiasm, keen vision in research direction, and super high efficiency in enforcing research plans, have kept inspiring me through my Ph.D. study. Under his guidance, I become a better researcher. I am also grateful to my co-advisor and mentor Dr. Tao Li for his constant guidance in my research. He always provides valuable ideas and plenty of encourages when I am faced with difficulties. I would also like to thank the other

TABLE OF CONTENTS

LIST OF FIGURES

LIST OF TABLES

ABSTRACT

Microsystems capable of sensing temperature, pressure and other parameters are needed for many applications, for example, gathering information in downhole environments for oil and gas exploration. Certain target locations limit the size of the microsystems to millimeter or even sub-millimeter scale. In addition, the high temperature, high pressure, and corrosive ambient environments are challenging for microsystems. Target environments include 125°C temperature, 50 MPa pressure, and salinity standards consistent with American Petroleum Institute (API) brine (8% NaCl + 2% $CaCl_2$). Other chemicals including hydrocarbons and cement slurry are also found in these environments.

The system package plays a critical role as it protects the system components against environment, while also providing the physical coupling to the environment, e.g., for communication modules and pressure sensors. The package must be made of mechanically and chemically robust materials. High temperature assembly steps must be avoided in the packaging process (such as bonding above 200°C), because these steps are generally incompatible with embedded batteries and polymer-based sensors. The development of system package and relevant technologies is the focus of this dissertation.

This dissertation first describes the design and fabrication of sapphire-on-steel packages in two sizes (0.8 mm and 8 mm), which are capable of isolating high pressure while allowing optical communication. These packages have been operated with embedded electronics at 125°C and ≈70 MPa in API brine, hydrocarbons, and cement

slurry. Additionally, polymer-in-tube packages are reported, which allow the embedded pressure sensors to couple with the environment. These packages have been successfully operated with embedded electronics and sensors at 125° C and 50 MPa in API brine. A third approach of encapsulation that is reported involves polymer film encapsulation, which has the potential to significantly improve the chemical resistance of microsystems. Finally a batch-mode packaging process is presented based on micro-crimping, enabling room temperature assembly for sub-millimeter scale packages made by metal alloys. This packaging process has been demonstrated by a 5×5 array of 0.5 mm packages. These packages have survived at least 200 MPa pressure and at least 72 h in API brine.

CHAPTER 1:

INTRODUCTION

Microsystems are miniaturized functional systems based on microelectronics, microelectromechanical systems (MEMS), communication, and packaging technologies [Tum01]. A typical microsystem may contain a microcontroller, a set of transducers usually based on MEMS technology, interface circuits, communication circuits, a battery and a system package (Figure 1.1). Small size, diverse functions and low cost are the prominent advantages of microsystems, enabling their prevalent applications in medical, consumer, and industry markets [Tum01, War01, Wis09].
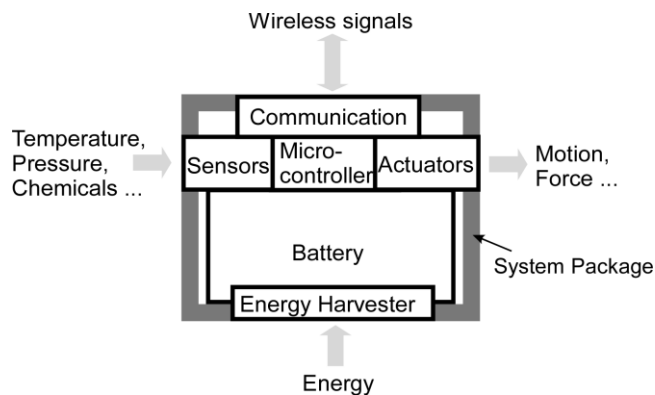
Figure 1.1: Schematic drawing of an autonomous microsystem

The system package is a critical part for the microsystem, because it not only protects all other components against the environment, but also provides the interface to the environment, e.g. for communication modules, pressure sensors, and chemical sensors. The system package is particularly important when the target application environment involves harsh factors, for example, high temperature, high pressure, various chemicals,

abrasion and impact, etc. The development of system package and relevant technologies is the focus of this dissertation.

1.1. Microsystems for Harsh Environment Applications

Microsystems are gaining significant interests in many industrial applications, because they can acquire detailed information that could not be obtained by traditional methods or by large size sensor systems. This previously unattainable information may save significant cost in industrial processes, from production to maintenance. However, in many industrial applications, the environments can be harsh for microsystems, with high temperature, high pressure, corrosive chemicals, abrasion, vibration, etc. [Wij11, Lee09].

1.1.1. Oil Production

One example of the harsh environment application is environmental sensing for oil production, and is also the target application of this dissertation. The exploration and production of fossil fuels presents an important opportunity and need for sensing microsystems. Figure 1.2 is a typical scenario of downhole environment for oil production. Oil and gas typically exist in reservoirs which are deeply underground. To reach there, wellbores are drilled, and fractures are induced by hydraulic process. Data on temperature, pressure and other variables in the wellbore, hydraulic fractures, and eventually in the reservoir, are valuable for maintaining quality, efficiency, and safety [Wij11, Cha12, Cha15]. Current data collection methods, including well logging, crosswell imaging, and seismics studies, can only provide aggregate information (Figure 1.3a). These could be supplemented by sensing microsystems with data logging capabilities.
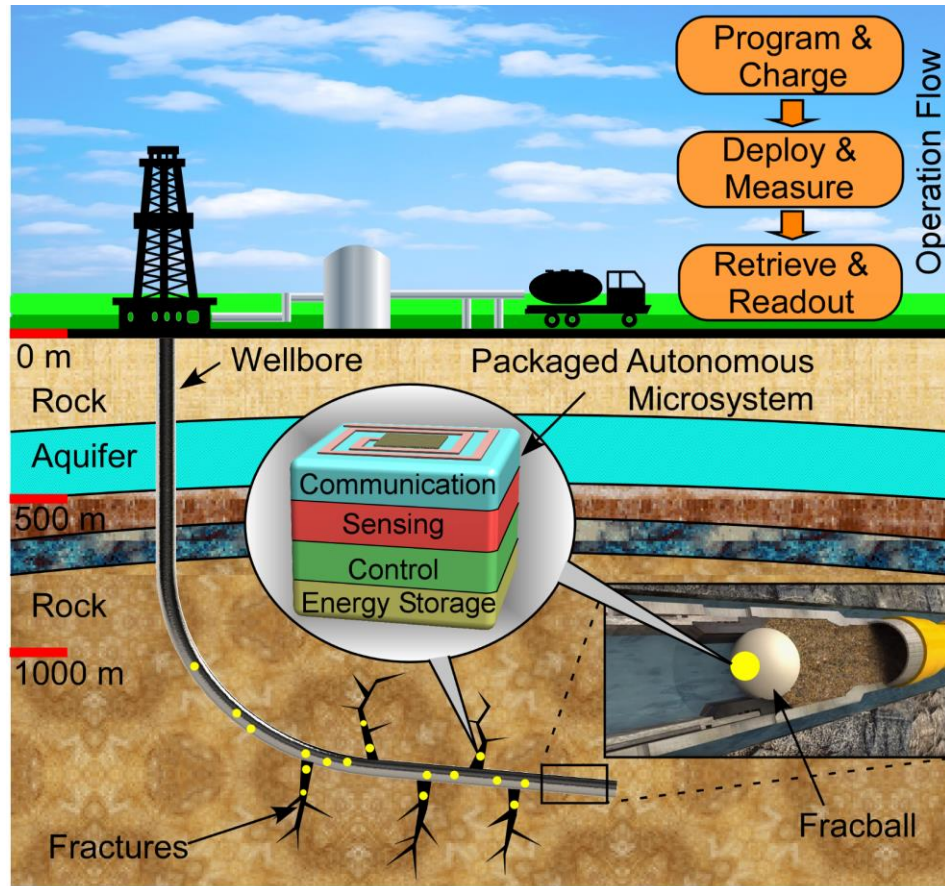
Figure 1.2: Typical scenario of downhole environment for oil production. Two possible ways that microsystems can be used: integrated with fracballs and injected into fractures. Courtesy of Mr. Yu Sui. The fracball insert part is from SMT Learning Chanel [Web-Hyd].

There are many possible ways that microsystems can be used, and two of them are shown in Figure 1.2. The first way is to integrate microsystems with fracballs. Fracballs are spherical tools used during the process of generating fractures. The size of a fracball is a few inches, and to avoid mechanically weakening the fracball, the microsystem to be integrated should be in millimeter scale. State-of-the-art microsystems can meet this size requirement. Detailed data of the fracturing process can be acquired from the microsystems integrated in the fracballs, which are valuable for oil production. The second way is to use very tiny microsystems that can be directly injected into fractures to collect

data and subsequently retrieved by carrier fluids for interrogation. However, the fracture size limits the size of microsystems and the packages for the them. The typical fracture sizes generated by the commonly used 20/40 and 40/60 proppants are 1.5 mm and 0.75 mm, respectively. This strict size limitation not only requires miniaturization of sensors, circuits, and batteries, but also system packages protecting them. The package size should be smaller than the fracture size, in order to allow the microsystems to be easily transported by fluid flow within the fractures.

In either way of using the sensing microsystems, the system packages need to provide protection against the harsh downhole environments. For oil reservoirs that are typically 0.6-6 kilometers deep underground, high temperature of 75-125°C, high pressure of 17-52 MPa, and high salinity of 5-15% (50,000-150,000 ppm) are typical in downhole environment, as listed in Table 1.1 [Cha12]. In some cases, hydrocarbons also take a significant portion in the fluids in downhole, which should also be considered.

(a) (b)
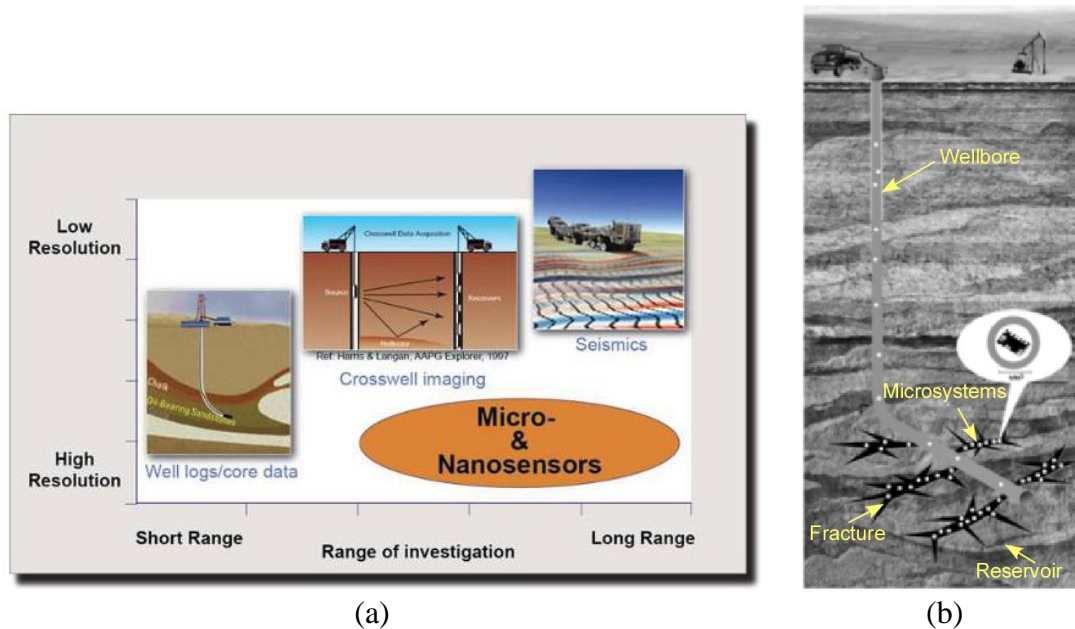
Figure 1.3: (a) Comparison of different subsurface investigation techniques in respect of resolution and range; (b) illustration of microsystems in wellbore and fracture. Revised from [Cha12].

Table 1.1: Typical Environmental Parameters and Size Constraint in Fractures. Revised from [Cha12].

Parameter	Typical Range	Maximum Value
Temperature	75 - 125°C	200°C
Pressure	17 – 52 MPa	183 MPa
Salinity	5 – 15% as NaCl	30% as NaCl
Fracball size	0.875" – 4.5"	/
Fracture Size	With 20/40 proppants, 1.5 mm With 40/60 proppants, 0.75 mm	/

There is few ongoing research in this area. One research group has developed a 7.5 mm diameter spherical microsystem which is capable of sensing temperature and pressure in wellbores [Yu12, Shi15]. This microsystem includes a digital temperature sensor, a pressure sensor for up to 100 MPa, a micro-controller, and a battery. These components are potted into a sphere shape with polymer. The concept of this microsystem design was successfully tested for operation in the wellbores. However, the packaging approach is not reliable, as three out of the six retrieved systems were broken into pieces after the test [Shi15].

1.1.2. Other Harsh Environment Applications

Microsystems are also useful in many other applications involving harsh environments, for example, marine applications. One scenario is the exploration of hydrothermal vents in sea floor [Li12]. As a source of energy and nutrients, hydrothermal vents support more than 1300 previously-unknown biological species living without the sun. This unique ecosystem can be better understood with better knowledge of chemical components and distributions in these locations. These data can be obtained by sensing microsystems capable of surviving the harsh factors there, including high temperature, high pressure, and corrosive chemicals. Another scenario in marine applications is monitoring fish behavior and population [Hyl05]. Excessive fishing activity may endanger certain fish

species. By placing microsystems on a number of individual fish, detailed information about their behavior, migration and population can be acquired. These data are valuable in making sustainable fishing plans. In this case, requirements for microsystems are more on chemical resistance.

The automotive industry, which has already equipped cars with many microsensors, will benefit more from sensing microsystems that can survive harsh environment. One example is combustion monitoring in automotive engines. The combustion process can be affected by many factors, including internal temperature, pressure, air-to-fuel ratio, fuel properties, etc [Wij11]. Traditional monitoring methods are indirect; with stricter emission standards and more competition on fuel efficiency among auto manufacturers, better monitoring methods are necessary. Microsystems are small enough to be integrated directly inside the combustion chamber to get precise and timely parameters, and are therefore expected to improve combustion control.

The various harsh environment applications not only require research efforts on new sensors and electronics that are resistant to these environments, but also call for investigations on robust packages that can protect the microsystems from the hostile factors.

1.2. Packaging and System Integration

Proper packaging of MEMS devices and microsystems can efficiently ensure their functions and increase their service life in target environments. Packaging is the most costly step in MEMS and microsystems manufacturing, which can account for up to 80% of the entire cost [Gil05, Lau10]. It is also a step with high failure rate. Although many of the MEMS packaging technologies are adapted from the integrated circuit (IC) industry,

it is widely acknowledged that packaging MEMS devices and microsystems is much more difficult than packaging ICs [Naj03, Lee09]. This is because that, compared to most IC devices which are planar, stationary, solid, and purely working in electrical domain, most MEMS devices have 3D structures, include moving parts, require interaction with complex domains, such as physical (pressure, acceleration, fluidics), chemical (chemical species, concentrations, reactions) etc. Packaging has three major tasks: protection for delicate structures, connection between signals and sensing environment, and assembly of multiple devices in a systematic manner [Naj03].

1.2.1. Levels of Packaging

Microsystems packaging can be divided into three levels: die level, device level and system level [Hsu08].
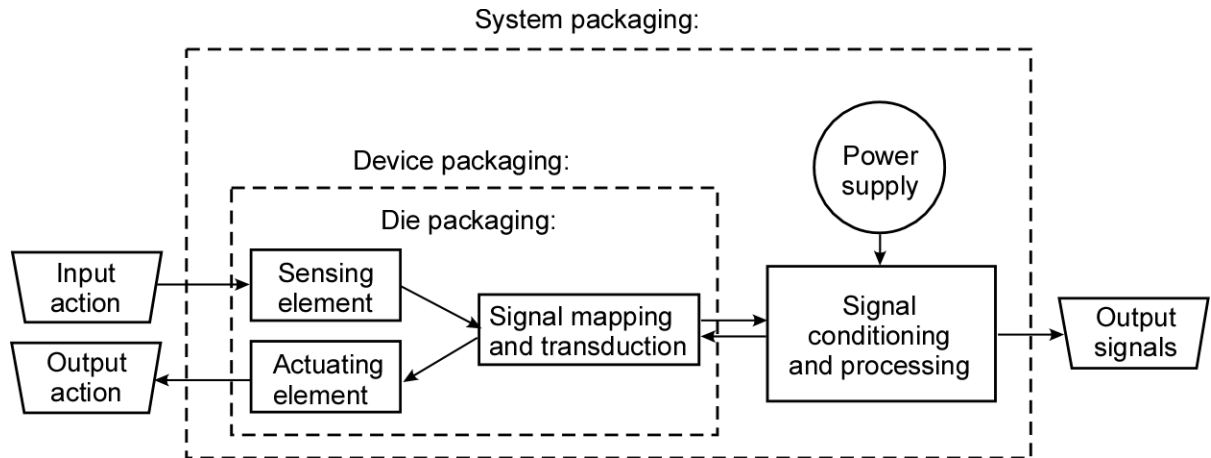
Figure 1.4: Three levels of microsystem packaging [adapted from Hsu08].

Die level packaging is to form functional chambers, channels and other geometries, and to protect the delicate core elements such as cantilevers, membranes and proof mass. Typically, either another cap wafer or a thin film deposition on the device wafer are used. This step should also accommodate vacuum or other special operation requirements for the

MEMS structures. Lead transfer is also an important task in this level to enable electrical signal connection to the sensing or actuating part from outside the die-level package.

Device level packaging is to include proper conditioning and processing circuit with the sensor or actuator. The circuit can be either on the same chip with the MEMS part or on a separate one. Interface circuits placed adjacently are especially important for high-impedance devices like capacitive sensors to maintain high performance. Metal pads should be formed outside the device-level package for lead transfer to the microcontroller and other components.

System level packaging is to integrate all individually packaged devices into a functional system, and provide the entire system enough protection and proper interface with target environment. Various types of devices can be integrated: sensors, actuators, microcontrollers, communication circuits, batteries, energy harvesters, and any other useful devices. In the case of harsh environment applications, the system level package is the major protection against adverse environmental factors, especially high pressure, corrosive chemicals, and abrasion. Thermal isolation is almost impossible for high temperature applications due to the small system size; while for low temperature applications, keeping the devices at constant higher temperature is possible and has been demonstrated [Lee09].

General requirements on the system package are: (1) mechanical protection from exterior pressure and abrasion; (2) resistance to chemicals in target environments; (3) water or gas tight depending on the application; (4) proper sensor interfaces to exterior environments. Requirements on the packaging process are: (1) relatively low temperature

to avoid deterioration of battery and polymeric sensors; (2) good manufacturability and scalability.

1.2.2. Traditional Packaging Technologies

Many of the packaging technologies for MEMS have been adapted from those developed for integrated circuits [Naj03]. In these, the device wafers are diced into chips, which are then individually attached, wire bonded and finally encapsulated in standard or customized dual in-line packages, ball grid arrays, etc. The packages made in this manner usually have footprints ranging from tens to thousands of mm^2. Some of these technologies require high temperature bonding steps (e.g. 200-500°C) [Min89]. Although these temperatures are compatible with most semiconductor electronics, microsystems with embedded batteries and sensors with polymeric materials typically require lower temperatures.

Various wafer level packaging (WLP) approaches have also been demonstrated with the goals to reduce both the size and unit cost of each package. In a typical implementation of WLP, the device wafer is bonded to a cap wafer before singulation [Cha08, Esa08, Lee10, Lap11, Naj07]. The substrates of the device wafer and the cap wafer form the package enclosure for each individual device. The material of the cap wafer is usually silicon or glass, which allows the use of traditional wafer level bonding methods, e.g., anodic, eutectic or polymer adhesive bonding techniques. Electrical signals are usually routed using compact methods such as through-wafer vias. These allow the package size to be significantly reduced compared to those from older technologies [Zos14, Tum01]. In some of the WLP approaches, the bonding steps require temperatures exceeding 200°C, eliminating the possibility of embedding batteries and certain polymer-

based sensors. Further, although WLP has been used to package MEMS and microsystems for use in standard environments [Yaz98, Kaa06, Mur09, Lee13], this approach has not been widely used for harsh environments, particularly those where high pressure and severe abrasion exist.

As stated in Section 1.1, there is an increasing interest for microsystems in harsh environment applications, where high temperature, high pressure, corrosive chemicals and abrasions typically exist. To meet the requirements of these harsh environment, metal or ceramic packages are superior to silicon, glass or plastic packages that are widely used in MEMS community. However, traditional fabrication methods, such as deep drawing for metal case formation and tape casting for ceramic case formation are difficult to make packages in sub-millimeter size. Micro electrodischarge machining (μEDM) and micro ultrasonic machining (μUSM) are capable of machining structures in this size on metals and ceramics, respectively. More details about μEDM technology, which has been extensively used in this work, are introduced in Section 1.4.

1.2.3. Integration Approaches for Electronics and Sensors

Traditionally, electronics and sensors are assembled onto a flat printed circuit board (PCB) for electrical connection. A microsystem integrated by this method occupies relatively large area. It is not suitable when the microsystem has a size limit in all three dimensions.

Four integration approaches that arrange components into a nearly cubic shape are shown in Figure 1.5. In this figure, a microsystem with cubic shape and a wall-mounted pressure sensor is assumed to exist. In the "plug-in" approach (Figure 1.5a), device chips

plug into a supporting layer with plug-in slots. This approach accommodates complex electrical routing, and the plugging step is self-aligned. However, the design and fabrication are complicated. In the "pin-hole stack" approach (Figure 1.5b), planar device chips with holes at corners are stacked together, and electrical connections among different chip layers are realized by metal pins penetrating the holes. This approach can achieve low connection resistance and high pin count. However, the system function relies on pin strength, the chips need perforation, and pin cut requires pre-planning. In the "staircase" strategy (Figure 1.5c), device chips with different lateral length are bonded into a chip stack, and electrical connections between different chip layers are realized by wire bonding. This approach is simple and mechanically robust, but has a limited space utilization, and the bond wires are fragile. In the "folded cable" strategy (Figure 1.5d), all the devices are first bonded onto a flat polymer cable, and then the cable is folded. This process does not require precise folding, and the assembly is mechanically robust. Disadvantages include the need of folding step and the cable is tightly curved. A comparison of the pros and cons of each approach is presented in Table 1.2.

Table 1.2 Comparison of four integrations strategies

	Plug-in	Pin-hole stack	Staircase	Folded cable
Pros	- Self aligned - Can allow complex electrical routing	- Low connection resistance - Can achieve high pin count	- Simple structure - Mechanically robust	- Do not require precise folding - Mechanically robust
Cons	- Complicated structure	- Pin strength - Requires perforated chips - Pin cut requires pre-planning	- Limited space utilization - Fragile bond wires	- Need folding step - Tightly curved cable

Considering the pros and cons of each integration strategy and the ease of fabrication, all the microsystems supported by packages described in this dissertation use the folded cable approach for component integration.
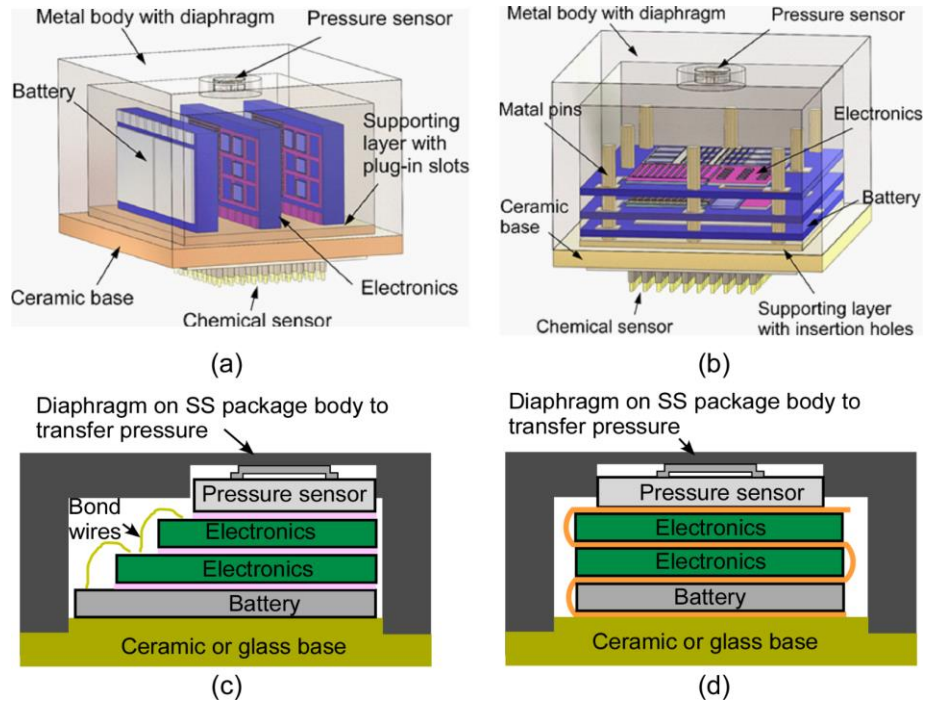
Figure 1.5: Four integrations strategies for a cubic shape microsystem: (a) plug-in; (b) pin-hole stack; (c) staircase; (d) folded cable.

1.3. Relevant Micromachining Technologies

Advancement in micro electro-discharge machining (µEDM) enables metal package fabrication in sub-millimeter size. This microfabrication method can be implemented in batch mode, and can therefore potentially increase fabrication throughput. Thin film coating materials, including atomic layer deposited (ALD) Al_2O_3 and Parylene-C^{TM}, can help preventing corrosive chemicals from diffusing into the package.

1.3.1. µEDM
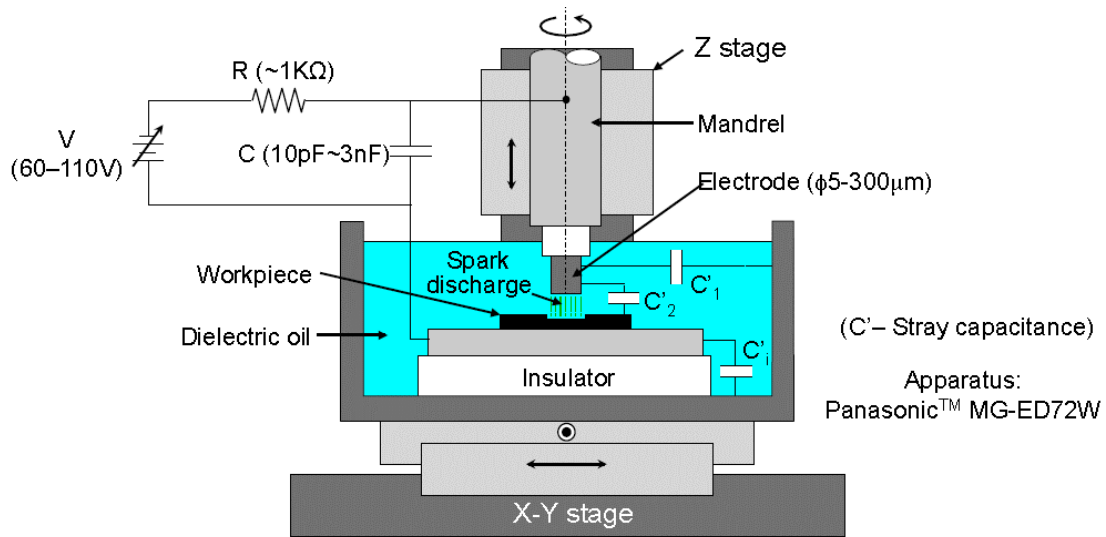
Figure 1.6: Schematic drawing of a µEDM tool [Tak05].

Electro-discharge machining (EDM) has been used to machine hard metals that are difficult to be machined by other methods since 1940s. Its miniature version, µEDM, was first demonstrated by Kurafuji and Masuzawa in 1968 with a 9 µm hole in 50 µm thick cemented carbide alloys [Kur68]. The µEDM process utilizes well-controlled electro-discharges between the electrode (tool) and any conductive materal to be machined (workpiece) to remove unnecessary volume of the workpiece. Dielectric oil or deionized (DI) water are usually used to flush away metal debris generated during machining. In traditional µEDM, the tool is a straight wire; the end of it approaches the workpiece to remove unnecessary volume. The wire is rapidly spinning during machining to avoid welding to workpiece and to facilitate debris flushing. It needs to be continuously fed into the workpiece to compensate for tool wear. The diameter of the wire and the discharge gap define the minimum cavity that can be made, which can be down to 5 µm with specially prepared tool by wire electro-discharge grinding (WEDG). By utilizing well-controlled

13

discharge circuitry and workpiece stage, µEDM can achieve accuracy down to 1 µm [Mas90, Web-Sma]. The machining speed and surface finish is affected by discharge energy. Higher discharge energy can result in higher machining speed, but rougher surface finish.

Traditional µEDM is essentially a serial fabrication method and therefore has a limited throughput. Efforts have been done to enable batch mode µEDM through tool electrode modification. LIGA-defined electroplated copper electrode arrays have been demonstrated to fabricate in parallel thirty-six 70 µm thick WC-Co gears with 300 µm outer diameter within 15 min [Tak02]. High-aspect-ratio silicon microstructures prepared by deep reactive-ion etching (DRIE) are also used as tool electrode for batch mode µEDM in die scale [Li13]. Minimum feature size of 7 µm and machining speed up to 5 µm/min has been achieved. Although many challenges exist in the development of batch mode µEDM process, such as adhesion issue of copper electrode on substrate, large tool wear of silicon electrode and debris accumulation in deep holes, batch mode µEDM is promising in increasing the µEDM throughput and reducing cost per unit in future.

1.3.2. Protective Coatings

Protective coatings can improve the survivability of the microsystem in harsh environments against various chemicals. For the microsystem with a system-level package, the assembly seam is the most vulnerable location where liquid containing chemicals can leak in. Protective coatings can block this diffusion route. The coatings can also protect non-chemical sensors that require direct interaction with environment. For downhole environment in oil exploration, concentrated corrosive brine and hydrocarbons are the major chemical concerns. The corrosive brine can be represented by American Petroleum

14

Institute (API) standard brine, which is 2 wt% of calcium chloride ($CaCl_2$) and 8 wt% of sodium chloride (NaCl) [Cha12]. The hydrocarbons are typically represented by Isopar[TM]-L.

Atomic layer deposition (ALD) of Al_2O_3 has been explored as protective coating against saline [Día11a, Día11b, Pot11]. For example, a 50 nm thick ALD alumina layer was shown to protect an aluminum alloy for at least 4 h under standard neutral salt spray testing at $35\pm2°C$ [Pot11]. The ALD is a well-controlled process to deposit highly conformal and pin-hole free thin films [Geo10]. In each step of the deposition, only a single-atom layer of aluminum or oxygen is deposited onto the previous layer due to a self-limiting chemical reaction; by alternating the two steps, highly conformal and pin-hole free thin Al_2O_3 layer can be deposited.

Many studies have shown that Parylene-C[TM] coating can protect substrate materials from corrosion in diluted saline solution (salinity$\leqslant$1.58 wt%) to some extent [Arn80, Li08, Ahm06, Cie11]. Parylene-C[TM] is a widely used coating polymer that can be deposited on samples at room temperature. It does not react with most chemicals at the room temperature and is considered to be biocompatible. Adhesion between Parylene-C[TM] and many substrate material is a concern. A thin layer of ALD Al_2O_3 under-layer is believed to improve the adhesion of the Parylene-C[TM] layer. An investigation shows that a 6 µm thick Parylene-C[TM] layer coated on a 52 nm-thick ALD Al_2O_3 layer was three times more resistant to 80°C 1xPBS (with salinity ≈1 wt%) than a standalone Parylene-C[TM] coating [Xie12]. Parylene-C[TM] coating also has very good chemical resistance to most organic solvents, including hydrocarbons. Immersion test of Parylene-C[TM] shows that its volume swelling is less than 3% in most organic solvents being tested [Bea02].

1.4. Goals and Challenges

This dissertation aims at developing system packages and relevant key technologies for microsystems to be used in harsh environments, particularly for downhole applications. The system packages need to protect microsystems from various harsh factors, including high pressure, various chemicals, abrasion and impact; meanwhile, it should allow physical coupling of the system with the environments for communication and sensing.

The design targets for the system package are 50 MPa pressure, 125°C temperature, a corrosive environment represented by API standard brine (8 wt% NaCl and 2 wt% $CaCl_2$), based on the typical environmental parameters in downhole (Table 1.1). Chemical compatibility with hydrocarbons is not defined as the required design target, but is explored as an additional factor that is potentially useful for some downhole applications. The targets for the exterior size of the package are less than 1.5^3 mm^3 for fracture applications and less than 10^3 mm^3 for fracball applications. These targets are listed in Table 1.3.

Table 1.3: Design targets of this dissertation

Parameter	Targets
Pressure	50 MPa (7,250 psi)
Temperature	125°C
Chemical	Corrosive brine represented by API standard brine (8 wt% NaCl and 2 wt% $CaCl_2$); Additional exploration: Hydrocarbons represented by Isopar^{TM}-L.
Exterior size of package	$<1^3$ mm^3 for fracture applications $<10^3$ mm^3 for fracball applications

To address these challenging requirements, several system packaging approaches and technologies are investigated with different goals.

The first goal is to design a system package to protect a temperature sensing and logging microsystem while allowing optical communication. To ensure the reliability of microsystem function, the system package should completely isolate the packaged system

from exterior high pressure and corrosive chemicals. Both sub-millimeter and millimeter scale packages need to be designed, for both fractures and fracball applications. Challenges of achieving this goal are in structural design and material selection to resist high pressure, sub-millimeter feature fabrication in metal, liquid-tight seal made at relatively low process temperature, and anti-corrosion protection. Efforts toward this goal are described in Chapter 2.

The second goal is to design and realize a system package that provides pressure transfer capability for pressure sensing. The package should protect system components from corrosive chemicals in environment, and allow optical communication as well. Challenges include how to effectively transfer pressure while minimizing temperature effects, and how to protect other components in the microsystem against pressure and corrosive chemicals in target environments. Efforts toward this goal are described in Chapter 3.

Chemical resistance is an important aspect of system package. Resistance to a wide range of chemicals is necessary for system reliability and lifetime in downhole environments, and is also relevant to other type of applications that involve corrosive chemical ambient. Although the coating approach described in Chapter 2 can provide good chemical protection, it still has some limitations, such as the use of certain combinations of materials that reduces the transparency of the optical window. To realize a general approach to provide chemical protection, the third goal is to investigate a film encapsulation approach. Challenges include selection of proper film materials, how to form a film layer that tightly surrounds the microsystem stack, and how to form a good seal that prevents any liquid leakage. Efforts toward this goal are described in Chapter 4.

The fourth goal is improving the manufacturability of the sub-millimeter scale package. In the intended applications, the quantity of sub-millimeter microsystems to be deployed will be significant, likely exceeding 10,000 – 100,000. Therefore, it is important to develop a batch mode packaging approach to reduce the cost-per-unit of the system package. In addition, the packaging approach should be at low temperature, because batteries and polymeric sensors are degraded after high temperature process. Challenges to achieve this goal include finding a low temperature sealing method, designing the batch mode schemes of package assembly, and developing a batch mode approach to integrate chip with package. Efforts toward this goal are described in Chapter 5.

1.5. Organization of Dissertation

This dissertation is arranged into six chapters. The packaging approaches and critical technologies presented in this dissertation are summarized and compared in Table 1.4.

Chapter 1 gives an introduction to the topic, including microsystems for harsh environment applications, microsystems packaging and relevant micromachining technologies.

Chapter 2 describes a sapphire-on-stainless steel package design with optical communication capability for target applications ("sapphire-on-steel" in Table 1.4). This is suitable for microsystems with temperature sensors, inertial sensors, magnetic sensors, and other sensors that do not require direct contact with the environment. It applies to two package sizes, the sub-millimeter one is for the fracture application, while the millimeter one is for the fracball application. Design, fabrication, and test results for both packages

are presented. Active microsystems are packaged in the millimeter packages, and tested in laboratory conditions that mimic the downhole environment.

Chapter 3 describes a polymer-in-tube package design with pressure transfer capability ("polymer-in-tube/steel" and "polymer-in-tube/ceramic" in Table 1.4). The mechanical behavior and parasitic capacitance are investigated by finite element analysis. Active microsystems with pressure sensors are encapsulated in these packages, and tested in laboratory conditions that mimic the downhole environment.

Chapter 4 describes a polymer film encapsulation approach intended to significantly improve the chemical resistance of the package against a wide range of chemicals ("polymer film encapsulation approach" in Table 1.4). Three packaging approaches using this are demonstrated ("film", "film-in-tube/steel", and "film-in-tube/ceramic" in Table 1.4). Test results regarding the chemical resistance and liquid leakage of the film encapsulation are presented.

Chapter 5 describes a low temperature batch mode packaging process for sub-millimeter microsystems in harsh environment applications. The process is demonstrated by a 5×5 array of sub-millimeter packages. Test results of the fabricated packages are presented.

Chapter 6 provides the conclusions from this dissertation, and proposes future work for a system package that only transfers pressure to the pressure sensor while isolating all other components from high pressure.

Table 1.4: An overview of packaging approaches and critical processes in this dissertation.

	Design	Mechanical protection	Chemical protection	Optical Interaction	Pressure Interaction
Packaging approach	Sapphire-on-steel	Yes	Yes	Yes	No
	Aluminum-in-steel	Yes	Yes	No	No
	Polymer-in-tube/steel Polymer-in-tube/ceramic	Yes	Limited	Yes	Yes
	Film	No	Yes	Yes	Yes
	Film-in-tube/steel Film-in-tube/ceramic	Yes	Yes	Yes	Yes
	Process	Function			
Critical process	Polymer film encapsulation process	• Significantly improves chemical protection. • Compatible with multiple packaging approaches. • Low cost and rapid manufacturing.			
	Micro-crimping process	• Compatible with sub-millimeter scale packages made by metal. • Reduces packaging process temperature to room temperature. • Improves packaging process scale			

CHAPTER 2:

SAPPHIRE-ON-STEEL PACKAGES WITH PRESSURE ISOLATION AND OPTICAL COMMUNICATION CAPABILITY

This chapter describes sapphire-on-stainless steel (SS) packages intended for microsystems in downhole applications. Two sizes of the packages have been designed: 8 mm and 0.8 mm. The 8 mm package is for fracball applications. The 0.8 mm package is for fracture applications, and the lid is made of glass instead of sapphire because smaller lids are subjected to smaller force under the same pressure. Both packages are capable of optical communication. The 0.8 mm package houses dummy Si chip stacks, demonstrating the electronics and sensors integration method using folded flexible cables. In the 8 mm packages, the first generation of environmental logging microsystems (ELM1.0) that includes a temperature sensor and no pressure sensor are packaged. Both packages survived high pressure and high temperature conditions, and the ELM1.0 systems successfully performed the temperature logging and reporting functions. This packaging approach is suitable for microsystems with temperature sensors, inertial sensors, magnetic sensors, and other sensors that do not require direct contact with the environment.

2.1. Design and Modeling

The 8 mm and 0.8 mm packages have the same structural design. The schematics of a package with a square footprint are shown in Figure 2.1(a). The square footprint is used for demonstration in this work; it allows better utilization of the internal volume, given

the shape of most electronic chips. Other shapes can also be envisioned to provide special benefits. For example, a circular footprint can reduce stress concentrations and allow the package to roll more easily within narrow fractures.
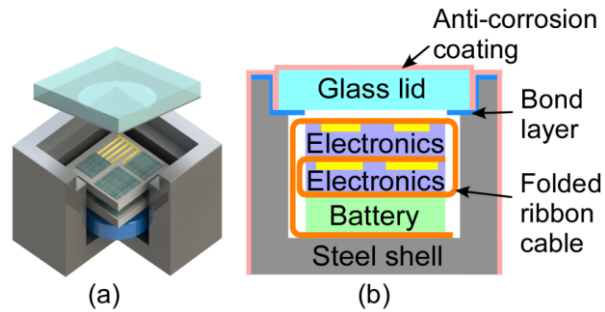
Figure 2.1: System design for the sapphire-on-SS package: (a) 3D view; (b) cross-sectional view.

The packages investigated in this study consist of two elements that are bonded together to form a sealed cavity: a metal shell made of stainless steel (SS) 17-4 PH and a lid made of borosilicate glass (for 0.8 mm packages) or sapphire (for 8 mm packages). The SS17-4 PH provides high yield strength, while the transparency of the borosilicate glass and sapphire allow optical communication with the microsystem within the package. For 0.8 mm packages, the lids were made of borosilicate glass instead of sapphire; although borosilicate has lower material strength than sapphire, it is adequate for 0.8 mm packages, because smaller lids are subjected to smaller force under the same pressure. Typical properties for these three materials are listed in Table 2.I. The package cavity is formed within the metal sheet (as shown in Figure 2.1), instead of in glass or ceramic substrates, because this provides higher robustness in the target high pressure environments. This stands in contrast to electronic packages. For the 0.8 mm packages, the outer dimensions are $0.8 \times 0.8 \times 0.8$ mm^3, and the inner dimensions of the cavity are $0.4 \times 0.4 \times 0.45$ mm^3. For the 8 mm packages, the outer dimensions are $8.8 \times 8.8 \times 6.85$ mm^3, and the inner dimensions

of the cavity are $6.8 \times 6.8 \times 4.6$ mm^3. The sidewall thicknesses are selected based on the finite element analysis (FEA) described below. Bonding and other process details are described in Section 2.2 and 2.4. The packages have anti-corrosion coatings on the outer surfaces to protect the bonding layer from the corrosive environment; these are described in Section 2.2.3.

Table 2.1: Typical properties of the chosen materials.

	SS 17-4 PH	Borosilicate	Sapphire (c plane)
Density (g/cm^3)	7.75	2.53	3.98
Strength (MPa)	760 - 1100 (Yield)	20-200 (Tensile)	1060 (Tensile) [Fis90] 2000 (Compressive)
Young's Modulus (GPa)	200	77.5	345
Long-Term Usage Temperature(°C)	<1400	<500	<2000

The approach selected for integration of components in the package is shown in Figure 2.1(b). A flexible cable provides electrical interconnections among electronic chips, sensor chips and the battery. The cable-component assembly is folded into a stack for integration into the package. This approach allows easy and reliable attachment of the components to the cable in a planar form before folding, and provides structural robustness.

The mechanical modeling of the package under the target pressure (50 MPa) was performed using COMSOL® 4.3. This was done for two purposes. First, to determine the minimum wall thickness for given exterior dimensions. Second, to identify the value and the location of the maximum deformation of the package under the target pressure with the selected dimensions. The package geometry used for modeling is parameterized as shown in Figure 2.2 (a).

The minimum wall thickness is limited by the maximum stress in the metal shell under the target pressure. For the 0.8 mm packages, a large safety margin between the

maximum stress and the yield strength of the material is provided, considering that the simulation is only an approximation and many factors could affect the real geometry (*e.g.*, machining precision) and material properties (*e.g.*, defects, temperature change, etc.) for these sub-millimeter scale structures. A series of simulations were performed with the sidewall thickness of the metal shell varying from 0.10 mm to 0.25 mm as shown in Figure 2.2 (b). A 50 MPa pressure was applied to all the exterior surfaces of the package in all simulations. The simulation results show that the maximum stress in the metal shell ranges from 323 MPa to 905 MPa, while the maximum deformation ranges from 0.18 µm to 0.64 µm. The safety factor, defined as the ratio of the yield strength to the maximum stress, was chosen to be 2.4 for the metal shell. As indicated in Figure 2.2 (b), the corresponding sidewall thickness is 0.20 mm and the bottom thickness is 0.15 mm. The maximum stress for this dimension is 416 MPa, and the maximum deformation in the metal shell is 0.22 µm. For the 8 mm packages, a smaller safety margin is selected. The selected thickness for all the walls is 1 mm. Simulation results for this selected dimension at 50 MPa pressure are summarized in Table 2.2. The maximum stress in the SS shell is 662 MPa, resulting in a factor of safety of 1.77.
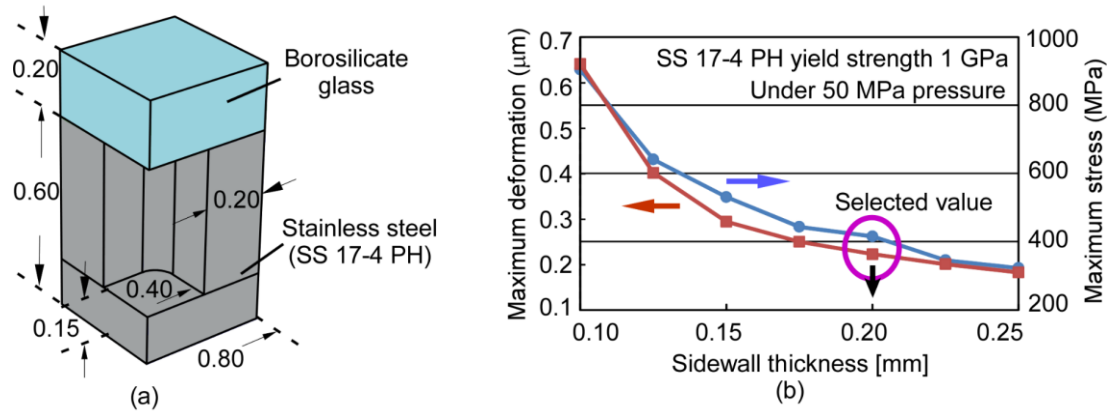
Figure 2.2: (a) Simplified geometry used in COMSOL simulation for 0.8 mm packages. Dimensions shown are used in fabrication. (b) Simulation results for package under 50 MPa with different sidewall thickness and 0.15 mm bottom wall thickness.

Table 2.2: Simulation results for 8 mm packages.

	SS shell	Sapphire lid	Stress distribution under 50 MPa
Maximum stress (MPa)	662	774 (comp.) 605 (tens.)	
Factor of safety (Yield strength / max. stress)	1.77	2.58 (comp.) 1.75 (tens.)	

The thickness of the lid selection was matched to the selected thickness of the sidewalls of the metal shell. Therefore, for 0.8 mm packages, the borosilicate lid was 0.2 mm thick, and for 8 mm packages, the sapphire lid was 1 mm thick. The maximum compressive stress in the sapphire lid is 774 MPa and the maximum tensile stress there is 605 MPa, resulting in factors o safety of 2.58 and 1.75, respectively. As the sapphire is a brittle material, the FEA simulation results may not be accurate.

The adequacy of these values were verified by experiments, considering the limited effectiveness of strength simulations for brittle materials.

25

2.2. Fabrication of 0.8 mm Packages

To assess the feasibility of the packaging approach, sealed, empty packages were fabricated using three major steps: micromachining of metal cans; attachment of glass lids; and coating with anti-corrosion layers. Test results of packages are detailed in Section 2.4. Additionally, dummy Si chips were electrically connected by flexible polyimide cables that were subsequently folded to fit within the interior cavity of packages.

2.2.1. Metal Shell and Glass Lid

Metal shells were fabricated using micro electro-discharge machining (µEDM) (SmalTec^{TM} EM203) [Mas90]. This process was selected because it has high machining precision and allows micromachining of high strength conductive materials such as stainless steel. A rotating tungsten electrode wire of 125 µm diameter was used as the cutting tool. During µEDM, the discharge energy, and thus the material removal rate and finish of the machined surface, is controlled by the applied voltage (V) and a capacitor (C). Discharge energy can be estimated by $\frac{1}{2}CV^2$ [Mas90]. Larger discharge energy provides faster machining speed but larger surface roughness. During the first machining step for the metal shell, the maximum capacitor available with this equipment (3300 pF) and an intermediate voltage (80 V) were selected for machining speed. In the polishing step, to reduce surface roughness, the smallest capacitor (10 pF) was used while the 80 V voltage was maintained [Mas90]. The corresponding discharge energy is about 3% of that used in the machining step. An SEM image of a machined metal shell is shown in Figure 2.3 (a). After the polishing step is performed with smaller discharge energy (Figure 2.3b), the area roughness (S_a) of the surface to be used for bonding is <100 nm, and the height variation

is <1 µm. These characteristics were provided by an interferometer (LEXT®, Olympus

Corporation, PA, USA).

Glass lids were formed by cutting VWR® cover glasses (Model No. 2 with ≈0.2

mm thickness) into 560×560 µm^2 pieces using a dicing saw (ADT 7100).

(a)

(b)   (c)
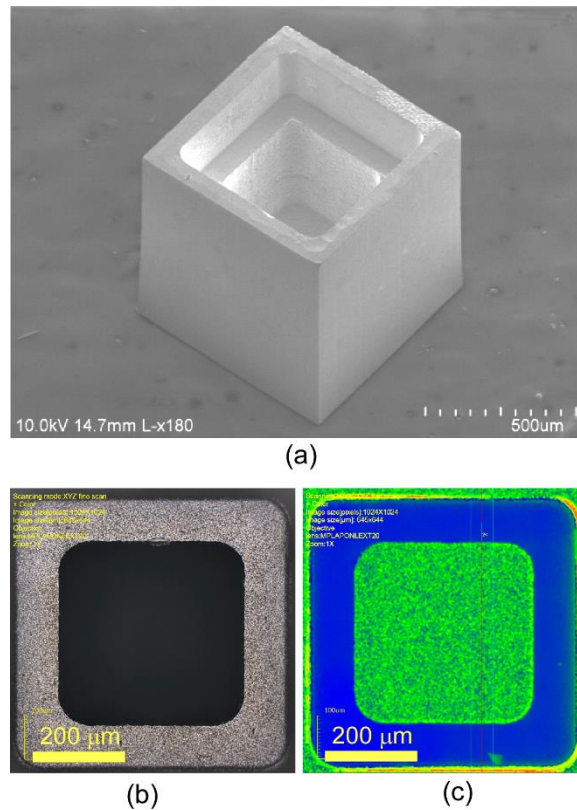
Figure 2.3: (a) SEM image of a metal shell made by µEDM from SS17-4 PH. (b) Optical photograph of a typical bonding surface rim on a metal shell, polished using µEDM with low discharge energy. (c) Interferometric measurements of the same surface rim. Surface roughness: $S_a = 65$ nm. Height variation across bonding area: <1 µm.

2.2.2. Package Bonding and Sealing

For sealing the glass lid to the metal shell, gold-indium (Au-In) bonding was

selected because of its low bonding temperature compared to other options [Wel08].

Different Au-In compositions (with In weight percentage varying from 13.14% to 90.5%)

have been reported [Wel08, Akt09, So00, Lee93, Shi99, Soh07]. Although an In-rich bond

(with In weight percentage >54%) has a lower re-melting temperature (156°C), the excess indium can relieve the stress generated between bonded parts, and can also reflow to compensate roughness and unevenness of the bonding surfaces [Akt09, So00, Str11]. Given the target deployment temperature, In weight percentage of ≈70% was selected.

The bond layers were designed with 100 nm Pd (for adhesion), 300 nm Au, and 2000 nm In on both rims of the metal shell and the glass lid. The 4 µm total thickness of indium was considered adequate for planarizing the metal shell, which had topographical variations of <1 µm on the bonding surface. The resulting weight percentage of indium was 71.6%. The thin film metal layers were deposited by evaporation. In order to provide a transparent window on the glass lid after bonding, sacrificial material (*i.e.*, photoresist) was placed in the center of the glass lid before the deposition of Pd/Au/In layers, and subsequently dissolved in acetone to lift off the metal layers.

The parts were bonded in a vacuum chamber (≈50 mTorr) with a bonding pressure of ≈10 MPa at 200°C for 2 hours. Bonded packages were left inside the vacuum chamber to cool down to room temperature. The bonding pressure was applied using a customized fixture. A metal shell bonded to a glass lid is shown in Figure 2.4. Top view of a bonded package is shown in Figure 2.6(a).
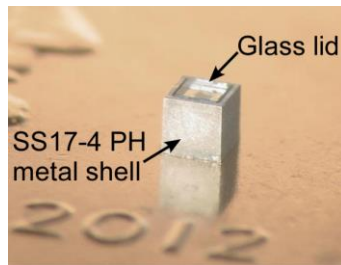
Figure 2.4: Photograph of a bonded package placed on a US penny.

2.2.3. Anti-Corrosion Coating

To protect indium layers used in sealing the package from corrosion in the hot brine environment, the bonded packages need to be further coated with anti-corrosion layers. As described in Section 1.3.2, ALD Al_2O_3 and Parylene-C^{TM} have good chemical resistance to brine. Since a thin under-layer of ALD Al_2O_3 can improve the adhesion of the Parylene-C^{TM} layer to many substrates, a bi-layer coating consisting of ALD Al_2O_3 and Parylene-C^{TM} was deposited on the exterior of packages.

In this work, thermal ALD of alumina was performed on the sealed packages at 150°C using Oxford^{TM} Instruments OpAL. Reactants are trimethylaluminium (TMA, $Al(CH_3)_3$) and water vapor. The base pressure before deposition was less than 20 mTorr and the deposition pressure was 300 mTorr. The deposited thickness was ≈220 nm, provided by 2000 deposition cycles. The packages were then coated with an adhesion promoter A174, which was deposited in the vapor phase. Following this, 12.8 µm thick Parylene-C^{TM} was deposited by a PDS 2035 Parylene Deposition System (Specialty Coating Systems, Indianapolis, IN). Figure 2.6(f) shows one of the packages after the two-layer coating.

2.3. Experimental Results of 0.8 mm Packages

The sealed, empty packages were subjected to a series of high pressure, high temperature, and hot corrosion tests. In addition, the shear strength of the bonded lids was tested using special structures. The sequence of tests conducted is shown in Figure 2.5; details are provided below. Additionally, the electrical connectivity of the dummy chips and the flexible polyimide cables were evaluated.
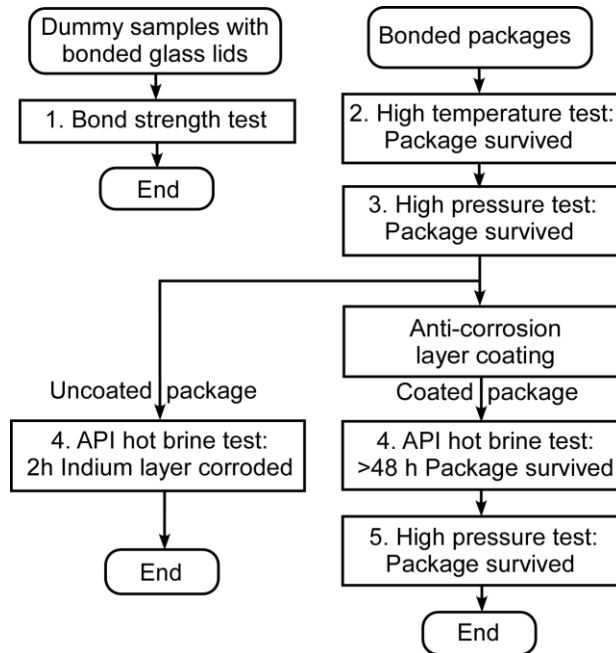
Figure 2.5: Test flowcharts of the bond strength test samples and bonded packages.
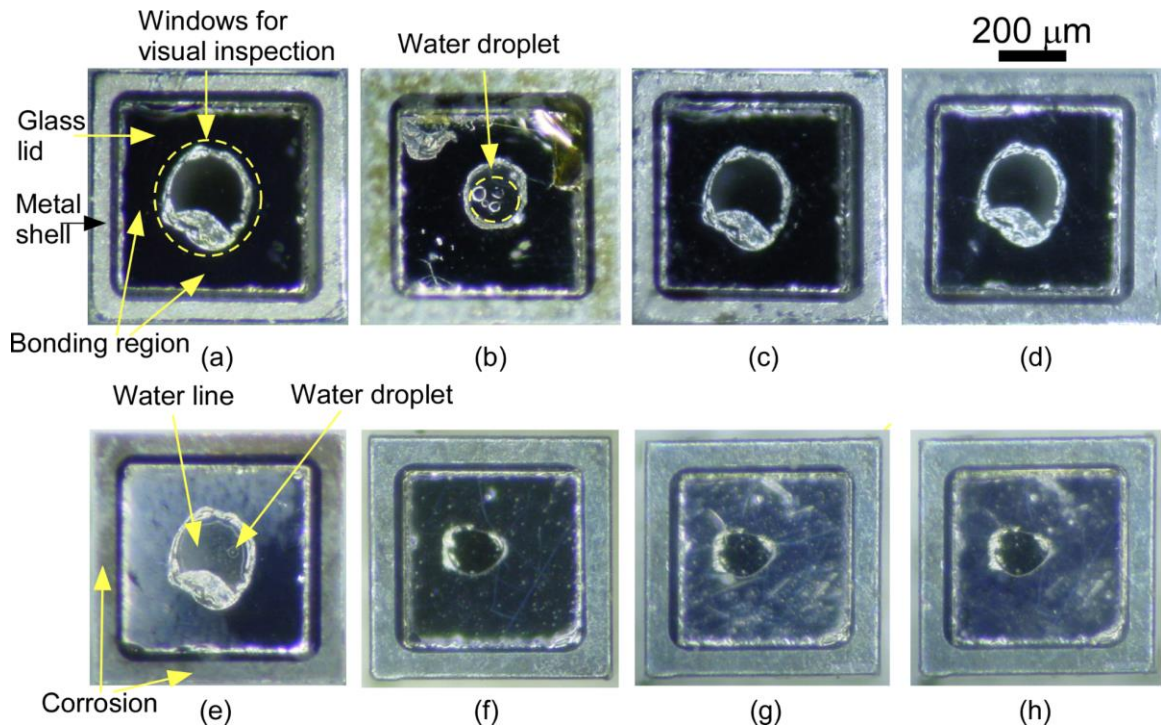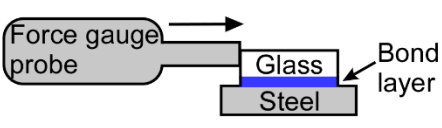
Figure 2.6: Top view photos of packages: (a) Uncoated sample after bonding; (b) Uncoated leaky sample after 4 h water soak; (c) Uncoated sample after high temperature test and 4 h soak; (d) Uncoated sample after high pressure test and 4 h soak; (e) Uncoated sample after 2 h hot brine test; (f) Sample after bonding and coating; (g) Coated sample after 48 h hot brine test; (h) Coated sample after 50 MPa post-brine high pressure test.

2.3.1. Lid Bond Strength Test

The shear strength of the Au-In bond used to attach the glass lid to the metal shell was experimentally evaluated. Test samples were prepared by bonding glass lids to a SS17-4 PH substrate using the same bonding conditions as for the actual packages. The shear strength tests were performed using a force gauge to determine the lateral force necessary to detach the bond. This force was divided by the 0.3136 mm^2 bond area to determine the shear strength (Table 2.II). The mean of the measured shear strength was ≈ 13 MPa, which is comparable to Au-In bonding results in the literature [Akt09, So00, Lee93, Shi99, Soh07, Str11]. Visual observation under an optical microscope indicated that the bond tended to break within the indium layer.

Table 2.3: Results of shear strength test of Au-In bond used for sealing of packages.

Bond area	0.3136 mm^2
Mean Breaking Force	4.170 N
Mean Shear Strength*	13.3 MPa

*Typical Au-In bond strength reported in literature: 1.5-40 MPa

2.3.2. High Temperature Test

The bonded packages were subjected to a high temperature (HT) bake followed by a room temperature hermeticity test. During the HT bake, sand in a glass beaker was heated to 125°C by a hot plate, with a thermocouple monitoring the temperature in the sand. A bonded package was buried in sand near the thermocouple for 5 minutes. The hot plate was then turned off and the package cooled down with sand.

After the HT bake, every package was soaked in water for at least 4 hours to determine gross leakage. In leaky packages, water droplets condensed on the inner surface of the transparent lids (Figure 2.6b). These packages likely had defects in the Au-In bond. In a typical well-bonded package, no leakage was observed after soaking in water for >100 h. A photo taken after the HT test followed by a 4 h soak is shown in Figure 2.6(c).

Only the packages that passed this gross leak check were subjected to later tests. Quantitative hermeticity test methods can provide more accurate results, though there are challenges for the application of such methods due to the extremely small volume of the inner cavity of the package. This is discussed in more detail in Section 2.6.

2.3.3. High Pressure Test Before Anti-Corrosion Coating

Bonded packages after HT test were subject to high pressure (HP) tests prior to deposition of the anti-corrosion coating in order to determine structural robustness at the target pressure. An Enerpac^{TM} hydraulic pump P142 was used to apply hydraulic pressure to an oil-filled testing chamber where the packages were housed (Figure 2.7). Packages were pressurized at 50 MPa (≈7250 psi) for 5 min. intervals.
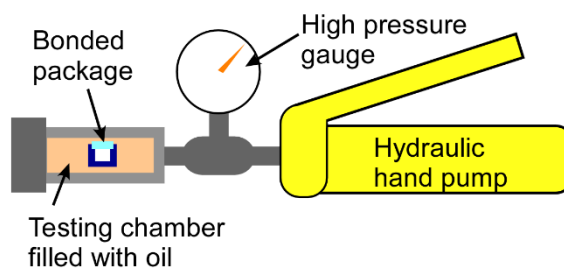
Figure 2.7: Schematic of high pressure test setup.

Packages with leaks are less likely to show mechanical deformation, as the oil from the hydraulic pump can enter the package and reduce the pressure difference across the

package walls. Therefore, only the packages passed the gross leakage test either from the previous HT test were used in this HP test.

After the high pressure test, neither plastic deformation on the metal shell nor leakage of pump oil into the package were observed. A SEM image of a package after the high pressure test is shown in Figure 2.8(a). To further evaluate if the metal shell was deformed in the high pressure test, the surface profile of the bottom wall was measured by an interferometer (LEXT®, Olympus Corporation, PA, USA). The bottom surface is the thinnest side of the package, and is expected to be the first to plastically deform by bowing under high pressure. Typical results are shown in Figure 2.8(b). The height variation across the entire width is ≈1.7 μm, which is also typical of the profile before the high pressure tests, indicating the absence of plastic deformation. The glass lids also survived the high pressure tests, with all samples remaining intact.

(a)   (b)
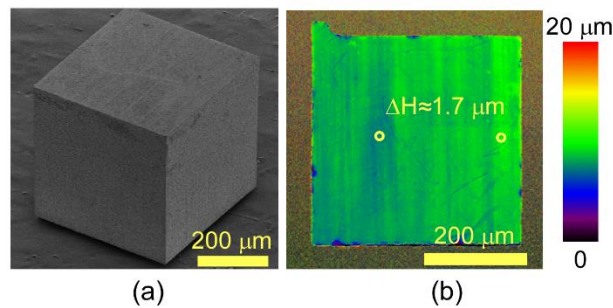
Figure 2.8: A typical sealed but uncoated package after high pressure test at 50 MPa: (a) SEM image. No deformation is evident. (b) Interferometric measurements of the bottom surface. Typical results show ΔH < 2 μm.

2.3.4. API Hot Brine Test

The anti-corrosion capability of the packages was tested in brine at 80°C and atmospheric pressure. The brine composition was 8 wt% NaCl and 2 wt% $CaCl_2$, in deionized water, in accordance with the American Petroleum Institute (API) testing

standard [Cha12]. Packages coated with 0.22 µm ALD Al_2O_3 and 12.8 µm Parylene-C^{TM} (Figure 2.6f) were subjected to the API hot brine test. Visual inspection was performed hourly during the first 4 h of the test, then every 2 h until the 24 h time point, and every 4 h until the 48 h time point. The time frame reported for a sensing microsystem to circulate in a wellbore is about one hour [Yu12]; although circulation through hydraulic fractures will likely take longer, 48 hours is expected to be enough for initial testing. Figure 2.6(g) shows a package after 48 h test. There was no sign of corrosion of the indium layer on the top surface of the metal shell, and no water droplet was evident in the window of the package, indicating the effectiveness of the anti-corrosion coating.

For comparison, an uncoated package was soaked in the solution. As the In in the bond layer can be attacked by NaCl solutions [Sai91], the bond was broken and water leaked into the package after a 2 h soak (Figure 2.6e). The glass lid easily separated from the metal shell with gentle rubbing.

2.3.5. Post-Brine High Pressure Test

In order to assess whether the 48 h brine test compromised the attachment of the lid, the 5-min. 50 MPa pressure test was applied once again. The metal shell and glass lid remained intact, and the bond remained unbroken after this test (Figure 2.6h). The absence of plastic deformation was confirmed by the same method as described in Section 2.3.3.

2.4. Fabrication of 8 mm Packages

The fabrication process for 8 mm packages is similar to the one for 0.8 mm packages, also consists of the same major steps: machining of metal shells; attachment of

glass lids; and coating with protective layers. There is a major difference in the method of attaching the sapphire lids to the metal shells, and a slight change in the coating process, which is described later in this section.

The machining of 8 mm metal shells was performed using a commercial service provided by SmalTec (SmalTec International, IL, USA). The machining process was a combination of traditional milling and μEDM: the majority of the inner cavity was removed by milling, and then the metal shell was machined to the final geometry by μEDM. In some of the metal shells, the milling tool slightly cut into the bonding surfaces, causing surface unevenness there (Figure 2.9a). The unevenness was undesirable, because it causes stress concentrations at the lid and may contribute to premature failure when pressure is applied.

The sapphire lid was machined by dicing. A C-plane sapphire wafer with 1 mm thickness was purchased from MTI corporation (MTI corporation, CA, USA), and diced into 7.6×7.6 mm^2 using a dicing saw (ADT 7100).

The glass lids were sealed with the metal shells using Masterbond® epoxy EP42HT-2 (Masterbond, NJ, USA). Epoxy bonding was selected to replace the Au-In bonding method, because epoxy bonding had less stringent requirement for the flatness of bonding surface. The epoxy has a glass transition temperature approximately between 150 to 160°C, and can be used at high temperature up to 232°C. However, preliminary test shows that this epoxy generates microcracks at elevated temperature which can induce leakage under high pressure. Therefore, protective layers were coated on the exterior surfaces.

The protective layer for the 8 mm package was a continuous Parylene-C^{TM} film formed on all surfaces of the package; as this continuous layer can effectively prevent brine

from attacking the interface between the coating and the package surface, the ALD Al_2O_3 under-layer was not used. To ensure a continuous coverage on all six surfaces of the package, the coating was done in two sessions of 5 µm coating. In each session, the package was supported with minimum contact area, and after the first session the package orientation were changed. A total of 10 µm thick Parylene-C^{TM} was formed on all the 8 mm packages.

Most of the 8 mm packages were sealed with ELM1.0 systems inside, while only a few were sealed empty to assess package performance. The ELM1.0 system was developed for temperature logging by a collaborating researcher, Mr. Yu Sui, using commercial components. It includes a microcontroller, a CMOS temperature sensor, a lithium ion battery, a solar cell, and an optical communication module. Photos of 8 mm packages with ELM1.0 systems inside are shown in Figure 2.9. Test results of these packages are detailed in Section 2.5.
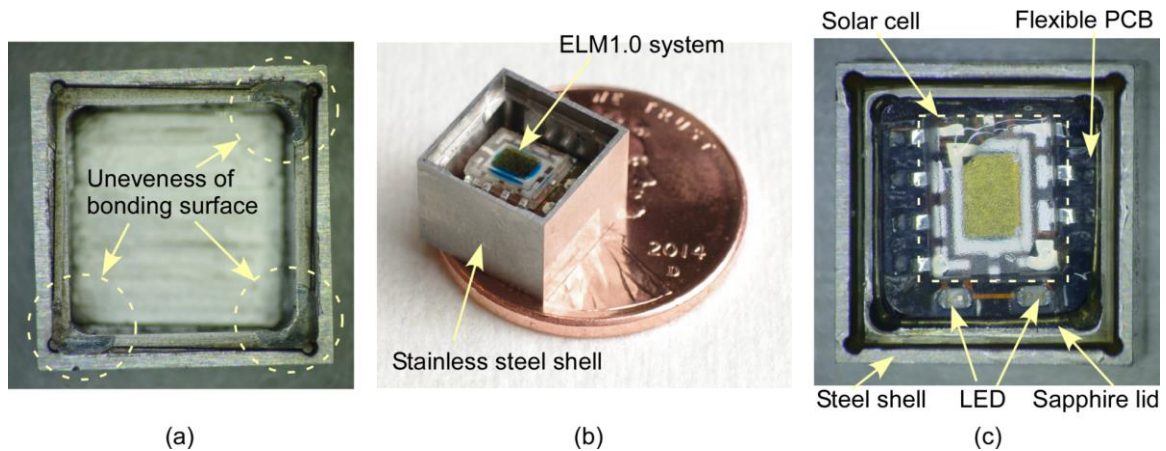
Figure 2.9: Fabrication results of the 8 mm packages: (a) example of a metal shell with unevenness on the bonding surface; (b) 8 mm package with ELM1.0 system before attaching the sapphire lid; (b) 8 mm package with ELM1.0 system after attaching the lid and coating with Parylene-C^{TM}.

2.5. Experimental Results of 8 mm Packages

Combined high pressure and high temperature (HPHT) tests were performed on the 8 mm sapphire-on-SS packages with ELM1.0 systems at RTI International (Research Triangle Park, NC, USA) on December 8-9, 2014, and at Total (Exploration and Production R&D Division) in Pau, France on February 2-5, 2015. The test equipment at RTI was HPHT Consistometer Model 275 (Fann Instrument, Houston, TX), whereas at Total a custom-built instrument was used. For both sets of tests, the ramping up and ramping down time for temperature and pressure was about 30 min. The target test conditions were 125ºC and 50 MPa in API brine. Extended conditions, including higher pressure up to 172 MPa (25,000 psi), and Isopar^{TM}-L, emulsion, and cement slurry were also tested. Details of the test media are listed in Table 2.4. The test duration at each programmed test condition ranged from 5 min to 3 h.

Table 2.4: Four types of test medium used in the HPHT tests.

Testing medium	Description
API Brine*	$CaCl_2$ 2 wt% + NaCl 8 wt%, downhole simulant
Isopar^{TM}-L#	Synthetic isoparaffinic hydrocarbon solvent from Exxon Mobil, oil simulant
Emulsion#	API Brine + Isopar-L + surfactants
Cement#	Uncured cement slurry, pH >2.4

*In specification. #Beyond specification.

A total of 12 packages were tested in 18 HPHT tests. Twelve out of the eighteen tests succeeded, and the packaged ELM 1.0 systems successfully performed temperature logging and reporting functions. At the target conditions of 125ºC and 50 MPa in API brine, the packaged ELM 1.0 systems successfully survived 60 min with without any functional issue, and the packages were not deformed or did not lose hermeticity based on

visual inspection under microscope. Typical photos of the packages before and after the
HPHT test in brine are shown in Figure 2.11. The packaged ELM 1.0 systems also survived
up to 70 MPa pressure, and in Isopar-L and in cement slurry, with a shorter test duration.
A summary of successful test results is shown in Figure 2.10.
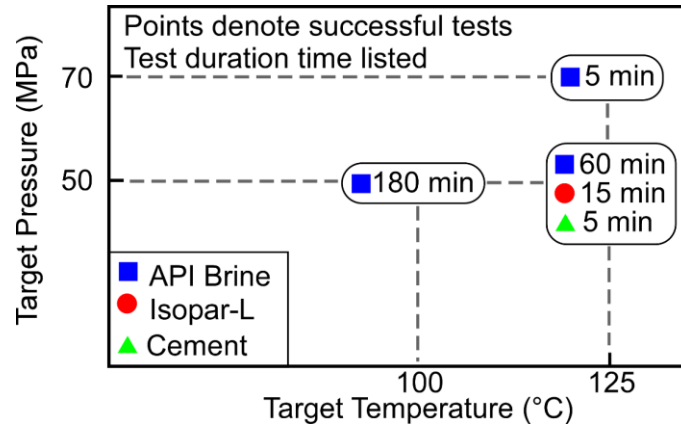
Figure 2.10: Summary of successful HPHT test results performed at RTI and Total.

Table 2.5: Types of failure in the six failed packages

Package quantity	Test pressure (MPa)	Test temp. (°C)	Test medium	Test duration (min)	Type of failure
1	50	125	Brine	30 min	Hermeticity failure
1	50	125	Brine	180 min	Lid cracked
1	50	125	Isopar-L	15 min	Lid shattered
1	103	125	Emulsion	10 min	Lid cracked
2	172	125	Brine	40 min	Lid shattered
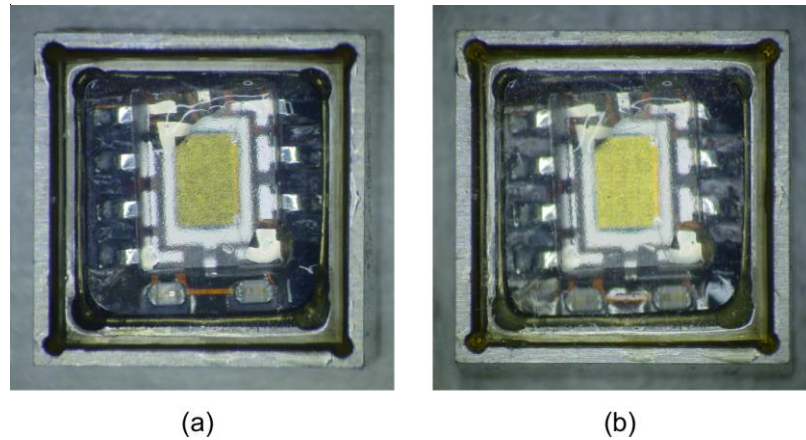
Figure 2.11: Photo of the top surface of a typical package (a) before any test, and (b) after HPHT test. No deformation in the SS shell, cracks in the sapphire lid, nor hermeticity lost was observed. Test conditions for this particular package were 125°C, 50 MPa (7,200 psi), 60 min hold.

Six packages failed in the tests. The type of each failed package is summarized in Table 2.5. The major package failure observed during the HPHT tests was the crack in the sapphire lid. This happened to all packages in the test at 103 MPa or above, which significantly exceeds the target pressure (50 MPa) in the design specifications. In one test at 103 MPa, the sapphire lids cracked, and the protective coating was pealed (Figure 2.12). For two packages, the sapphire lid cracked at 50 MPa, probably because of material or fabrication defects in the sapphire lids, or the stress concentration from the unevenness of the bonding surface. Another package failure observed is hermeticity failure without deformation in the SS shell or cracks in the sapphire lid. Only one package failed in this way. Immediately after the HPHT test of the package that was conducted at RTI, when the package was withdrawn from the brine, a droplet was released at a corner on the top surface, indicating a compromise of the epoxy bond (Figure 2.13). Upon further inspection of this location, a broken bubble was found in the epoxy, which appeared to be the cause of the compromise. The cause of the bubble was hypothesized to be inadequate degassing

of the epoxy during the sealing step. As a consequence of this observation, a degassing step for the epoxy was added in the packaging process, and the same issue did not occur again in later HPHT test at Total. The degassing was performed by placing the package in a vacuum chamber at room temperature for about 30 min.

(a)   (b)
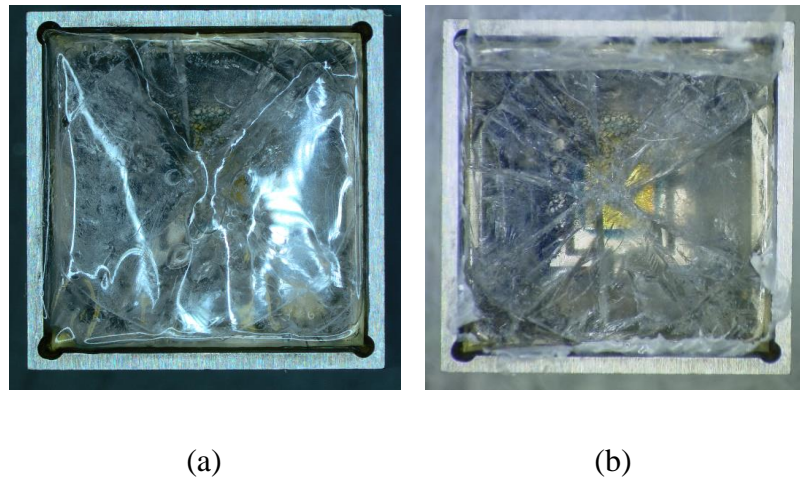
Figure 2.12: Package after a test performed at pressure that were twice as high as the design target: (a) Photo of the package immediately after test, showing peeled protective coating above the sapphire lid. (b) Photo of the same package after removing the peeled protective coating, showing the cracks in the sapphire lid. The set condition for this test were 125°C and 103 MPa (15,000 psi) in emulsion. The hold time at the set conditions was 10 min.
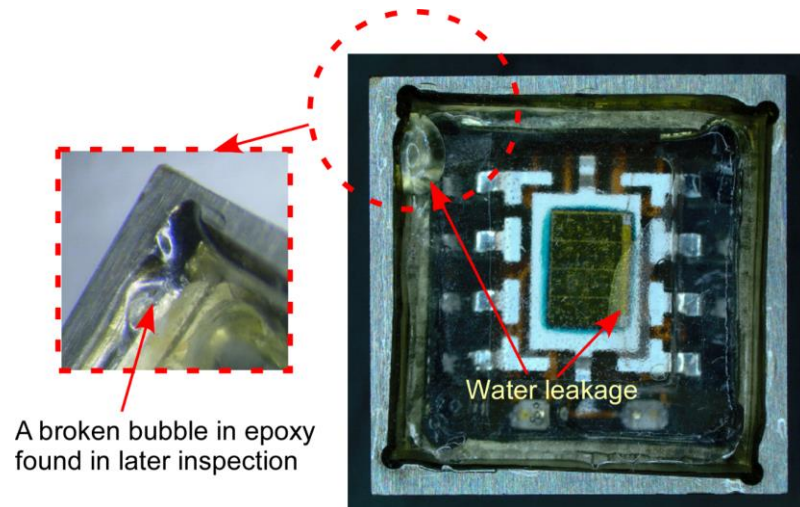
Figure 2.13: Photo of the top surface of a package with hermeticity loss after the test. Water leaked into the package and a water droplet was at a corner, indicating hermeticity failure. At the same corner a broken bubble was found in epoxy in later inspection. Neither

40

deformation in the steel shell nor crack in the sapphire lid was observed. The set condition for this test were 125°C and 50 MPa in API brine. The hold time at the set conditions was 30 min.

2.6. Discussion

The corrosion lifetime of the coated packages can be limited by several factors, including the thickness and quality of the alumina and Parylene-C[TM] layers, the surface adhesion between alumina and stainless steel, and between Parylene-C[TM] and alumina [Día11b, Pot11, Li08]. Moisture penetration through the Parylene-C[TM] coating can compromise adhesion [Li08]. The underlying ALD alumina slowly dissolves in NaCl solution, and the porosity of the remaining layer gradually increases [Día11b]. The use of ALD alumina as an interlayer and a thicker Parylene-C[TM] layer provided adequate protection for packages for >48 h in hot brine. However, in this work, the bi-layer coating was not applied to the bottom surface of the cubic packages, which faced the carrier substrate during the coating process. The exposed alumina at the edges of the coating could be more easily attacked by brine. This has caused gradual undercut of the Parylene-C[TM] coating on the sidewalls of the packages during the brine test, and limited the long-term viability. An all-round bi-layer coating will likely provide better corrosion resistance and longer lifetime.

For the 0.8 mm packages, the fabricated packages survived separate tests for high temperature, high pressure, and high salinity. However, the test setup at that time did not permit the simultaneous application of all three stressors. Further, although several packages were fabricated and tested, the quantity was insufficient for statistical evaluation. These aspects of evaluation are complemented by the combined HPHT tests in various test media on the 8 mm packages.

As indicated in Section II, the dimensions of the packages can be scaled as needed. The lower limit on the size of the inner cavity of the metal shell is determined by the minimum feature size of the μEDM technique, which is typically ≈5 μm [Asa07]. Alternative techniques such as laser machining may generate smaller features, though the machined structures may be subject to higher thermal stress. The design values used in this work, such as the wall thickness of the metal shell, were cautiously chosen with relatively large safety factors. For smaller safety margins, thinner walls can extend the interior volume available for components.

Although serial mode μEDM was used in this work for fast prototyping, a batch-mode μEDM method using lithographically-defined electrodes can be applied for high throughput production and potentially lower unit cost to fabricate the 0.8 mm metal shells [Tak02, Li13]. In batch-mode μEDM, high aspect-ratio microstructures with patterns defined by lithography on a silicon substrate are used as a cutting electrode. The entire pattern can be transferred to the workpiece in one machining cycle, resulting in multiple pieces fabricated in parallel. However, the batch-mode μEDM cannot be easily applied to the 8 mm packages, because a large volume of material needs to be removed to form the large cavity.

The method used to evaluate leakage of the 0.8 mm packages was to visually inspect for condensation in the package interior. Alternative methods may be considered for quantitative analysis in the future. The commonly used helium bombardment test specified in the MIL-STD 883 standard, however, may not be suitable for two reasons. First, the inner cavity volume of the package is only 7.2×10^{-5} cm^3, whereas the helium test is not suitable for packages with inner cavity less than 10^{-3} cm^3 [Tao05]. Second, the

package uses a glass lid, which absorbs helium, thus affecting the accuracy of the helium test result [Cos12]. Other methods have been reported to test hermeticity of devices with small cavities, including through-hole [Ant12], cap deflection [Elg04], internal pressure sensor [Tsu01, Che02, Mit09], FTIR spectroscopy [Vey05], Raman spectroscopy [Web97], residual gas analysis [Mor03], etc. These test methods and their limitations have been summarized [Cos12, Mi09, Ant13]. However, proper pass/fail leakage thresholds that can be used as a widely-accepted standard are not available yet [Cos12].

2.7. Summary

The concept of sapphire-on-SS packages with optical communication capability have been successfully demonstrated. Two different sizes of the package, 0.8 mm and 8mm, have been designed and fabricated. The packages consisted of stainless steel shells, borosilicate glass or sapphire lids and protective coatings (Al_2O_3 and Parylene-C^{TM}, or Parylene-C^{TM} alone). The 0.8 mm packages survived high temperature tests at 125°C, high pressure tests at 50 MPa, and corrosion tests in API standard brine at 80°C. The 8 mm packages survived combined HPHT conditions up to 70 MPa, 125°C, and 60 min, in various test media including API brine, Isopar^{TM}-L, and cement slurry. ELM1.0 systems packaged in them successfully performed logging and reporting functions in these tests. The overall size and the resistance to harsh conditions suggest that the sapphire-on-SS packaging approach is suitable for downhole environments and the exploration and production of fossil fuels.

CHAPTER 3:

POLYMER-IN-TUBE PACKAGES WITH PRESSURE TRANSFER CAPABILITY

The microsystems packages introduced in Chapter 2 are closed structures with rigid walls that isolate all microsystem components from external pressure. These packages are suitable for microsystems with temperature, magnetic, or inertial sensors that do not require physical interaction with external environments. However, these packages are not suitable for pressure sensors, as external pressure cannot be effectively transferred to the interior of the package for sensing. This chapter focuses on an alternative packaging approach that provides the pressure transfer capability. In order to demonstrate the efficacy of this approach, the second generation of environmental logging microsystems (ELM 2.0) that includes a temperature sensor and a pressure sensor are packaged and tested.

3.1. Comparison of Pressure Transfer Approaches

3.1.1. Transferring Pressure to Pressure Sensor Only

The system package can be designed in a way that the external pressure is only transferred to the pressure sensor but isolated from all other components. This essentially requires the pressure sensor to be a part of the package wall. Two examples of this approach are shown in Figure 3.1. In the first example (Figure 3.1a), a through-hole is machined on the top wall of the SS package. The periphery of the pressure sensor has to be completely fixed with the wall in order to balance all the external pressure. The hole is

filled with a soft polymer to allow pressure transfer while prevent direct exposure to corrosive chemicals in environment. The second example (Figure 3.1b) is similar to the first one, except that the mounting hole for the pressure sensor is only partially machined, leaving a thin SS diaphragm to prevent direct exposure to the environment. It also requires the pressure sensor to be fixed with the wall.
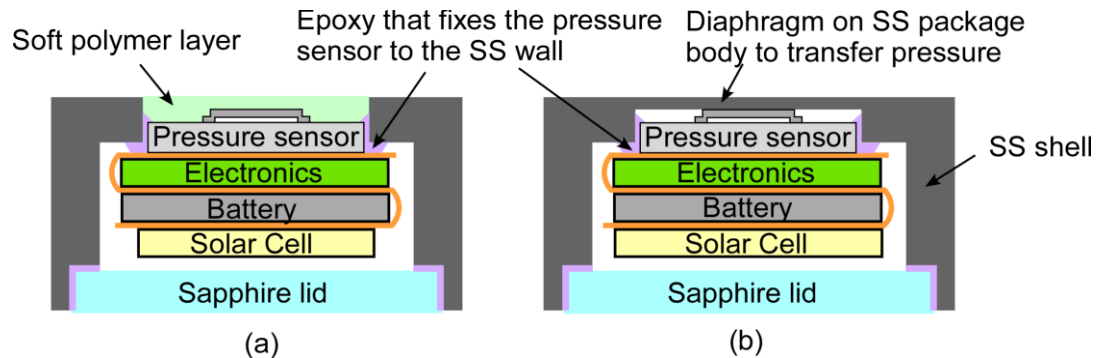
Figure 3.1: Two examples of transferring external pressure to the pressure sensor only: (a) using soft polymer to transfer pressure; (b) using thin diaphragm on SS package to transfer pressure. In both cases the pressure sensor should be completely fixed with the SS package wall.

The advantage of this pressure transfer approach is that the other components are not under high pressure; as long as the package does not leak, there is little concern in the reliability of the microsystem components. However, several disadvantages are obvious. In the design of Figure 3.1(a), the epoxy or other type of bond between the pressure sensor and the package wall has to withstand all exterior pressure. Any defects in the bond may lead to failure of the entire system package, limiting the packaging yield. In the design of Figure 3.1(b), at high temperature, the thermal expansion mismatch between the SS diaphragm and the pressure sensor diaphragm can affect the pressure sensor performance. This effect depends on material properties and also manufacturing factors including the SS

diaphragm thickness, residual stress, etc., and therefore is undesirable. In brief, this packaging approach is very challenging in manufacturing.

3.1.2. Transferring Pressure to Encapsulated Microsystems

In this approach, the microsystem is encapsulated by a soft material, and the external pressure can be transferred to all the components including the pressure sensor (Figure 3.2). Since the pressure sensor diaphragm is much stiffer than the soft polymer, most of the pressure can be transferred to the pressure sensor. Some studies have shown that many electronic devices are able to function well under high pressure condition for years. These are summarized below. Therefore, microsystems packaged in this way might be able to survive in the target application.
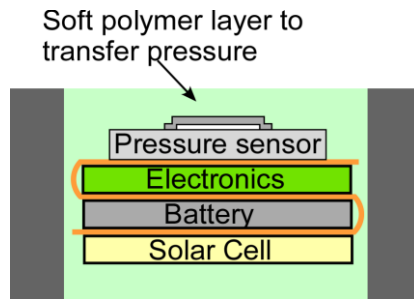
Figure 3.2: Transferring external pressure to the encapsulated microsystems.

Although there is a concern about the reliability of the microsystems under high pressure, this pressure transfer approach is simple to implement, and therefore is selected to pursue.

Pressure Tolerant Electronics

Pressure tolerant electronics (PTE) refer to electronics that can maintain normal functionality under high pressure. Such devices do not need a rigid pressure-proof enclosure, and can be protected either by a water-proof coating or by an oil-filled thin-

walled container which has the internal and external pressure balanced. This concept was introduced in 1960s, when the solid-state electronics was apparently replacing the vacuum-tube-based electronics. The major motivation was from the U.S. Navy. At that time more and more electronic devices were adding to submarines. Since the internal space was tight, the U.S. Navy considered moving some electronics outside submarines [Bar76, Mar78].

Multiple tests in the 1960s and 1970s showed that the functions of transistors and passive devices were not affected by high pressure and inert oil environment [Mar78]. It was believed that electronic devices with homogeneous structure and free from air voids could be potential PTEs. In one paper [Mar78], 750 individual components of six classes, including resistors, capacitors, diodes, integrated circuits, inductors, and preamplifier modules, had been tested under 69 MPa (10,000 psi) in silicone oil for five years. Five pressure cycles had been done. The components did not have special packaging. Only three failures occurred out of the 750 components. The results indicate that many electronic components can function well both under high pressure and after long-term exposure to high pressure.

The fact that PTEs survive high pressure can be understood from mechanical and electronic aspects. In the mechanical aspect, a stress tensor can be broken down into two parts: an isotropic part which is the mean stress, and a deviatoric part which is the rest. The stress generated in solid materials under hydrostatic pressure is on the same order of the applied pressure, as long as there is no significant stress concentration. In this stress, the isotropic part takes a large portion, while deviatoric part which relates to material failure only takes a small part. Most electronic devices are fabricated based on silicon wafers. The yield strength of silicon is about 7000 MPa, which is much higher than the applied

pressure (in the range of 50 – 100 MPa), and therefore is even higher than the deviatoric stress. Therefore, mechanically the material is safe. In the electronic aspect, there is limited effect on the band gap of semiconductor materials from pressure <100 MPa. At 100 MPa, conduction band minima increased by 0.005 eV or 0.76% from the 0.66 eV at atmospheric pressure [Pau61].

The discussions above are only on the device level. The high pressure compatibility of assembled electronic stacks needs to be verified experimentally. The ELM2.0 stacks used in this work have been demonstrated working under 50 MPa pressure.

3.2. Polymer-in-Tube Package Design

3.2.1. Design Concept

In the polymer-in-tube package design, a hard tube is filled with a soft polymeric material within which the electronics and sensors are located. The hard tube is resistant to abrasion and impact. The soft polymer protects the electronics from impact while permitting pressure transfer from the environment to the pressure sensor in an accurate manner. The transparency of polymer can be selected to facilitate certain function, for example, transparent polymer permits optical communication and charging of the battery through solar cells, and opaque polymer shields the electronics.
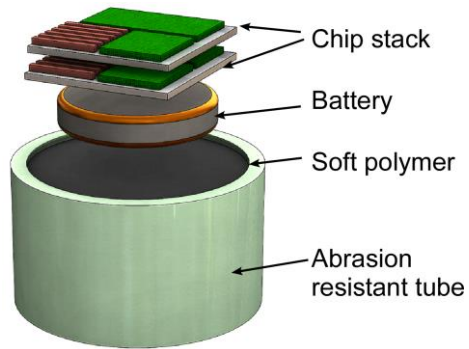
Figure 3.3: Schematic of the Polymer-in-Tube Package Design

The soft nature of polymer is essential to transfer the environment pressure to the pressure sensor in an accurate manner. The polymeric material should be significantly less stiff than the pressure sensor diaphragm. This is necessary to reduce the temperature coefficients of the polymer-encased pressure sensor and to mitigate the impact of unit-to-unit variations in the thickness of the polymer. This is because the soft polymer only counteracts a small fraction of the environment pressure. Its fluctuation due to temperature change or unit-to-unit variations in thickness has limited influence on the pressure measurement.

To demonstrate the pressure transfer function of this new package design, a new version of environmental logging microsystems with capacitive pressure sensors (ELM2.0) developed by colleague researchers are packaged in this design. The ELM2.0 system consists of commercial electronic components and a customized capacitive pressure sensor. All components are assembled into a stack with a folded flexible polyimide cable. The size of the ELM2.0 stack is $7.6{\times}6.6{\times}5.9$ mm^3.

3.2.2. Selection of the Tube

The tube material should be mechanically robust to resist abrasion and impact in the target environment. Two types of materials, stainless steel (SS) and ceramic, are suitable for this application. Stainless steel has a better resistance to impact because it is a ductile material. Ceramic is non-metallic, and a more suitable choice if the enclosed microsystems utilizes RF communication.

The SS 304 tubes and alumina ceramic tubes are selected. The SS 304 has a yield strength of 204 MPa, which is strong enough for this package design. It is also resistant to brine and hydrocarbons. Other types of stainless steel, such as type 316 or 17-4 PH, which have higher yield strength and better chemical resistance, can also be used. Alumina is the most commonly used material for high performance ceramics, and has a tensile strength is 241 MPa. It is also resistant to brine and hydrocarbons. Parameters for the tubes evaluated in this effort are listed in Table 3.1.

The SS tube was an off-the-shelf tube made from SS 304 (American Stainless Steel Tubing, Inc, NC, USA). It was selected because the inner size was closed to the ELM2.0 stack size. The ceramic tube was customized by commercial service (LSP Industrial Ceramics, Inc, SC, USA).

Table 3.1: Information of Selected Tubes [Web-Che, Web-Sta]

Tube material	Material property			Tube geometry			
	Strength (MPa)	Resistance to brine	Resistance to hydrocarbons	Shape	Inner size (mm)	Outer size (mm)	Length (mm)
Alumina Ceramic	241	Good	Excellent	Rectangular	7.7×7.5	9.7×9.5	6.5
SS 304	205	Good	Excellent	Square	7.8×7.8	9.5×9.5	6.5

3.2.3. Selection of the Polymer

The filling polymer should fulfill the following requirements. First, the polymer should be much less stiff than the pressure sensor diaphragm, which is necessary to reduce the temperature coefficients of the polymer-encased pressure sensor and to mitigate the impact of unit-to-unit variations in the thickness of the polymer. Second, it should be compatible with high temperature of at least 125°C. Third, it should be chemically resistant to the corrosion environment represented by API brine. Fourth, for the purposes of solar cell charging and optical communication, the polymer should be available in a transparent form. Fifth, the polymer should be able to cure at low temperature, to avoid degradation of the embedded battery.

Silicone is a type of polymer that can fulfill all the requirements above. Silicone is soft, clear, serviceable over 200°C, has good chemical resistance, and can be cured at room temperature. Two specific silicone products, Do It Best™ silicone sealant (referred to as caulk) and Dow Corning™ Sylgard 184 (referred to as PDMS), are selected for packaging, and their properties are listed in Table 3.2. The chemical composition of the caulk is mainly hydroxyl-terminated dimethyl siloxane, and of the PDMS is dimethylvinylsiloxy-terminated dimethyl siloxane. The different end functional groups cause some differences in their properties. The caulk has good resistance to brine and moisture, and also has good adhesion to many materials. The PDMS does not chemically degrade in brine; however, it readily absorbs moisture. It has very low viscosity before curing, which is desirable for filling folded PCB structures. Additionally, cured PDMS is also very clear and transparent, so it does not impede optical communication between the embedded electronics and

external systems. Therefore, PDMS is also selected as a candidate of filling polymer. The calculations of the spring constant of these materials are described later in this section.

Table 3.2: Properties of Selected Silicone Products

Product	Do It Best™ Silicone Sealant ("caulk")	Dow Corning™ Sylgard 184 ("PDMS")
Main composition	Dimethyl siloxane, hydroxyl-terminated	Dimethyl siloxane, dimethylvinylsiloxy-terminated
Spring Constant	$\approx 2 \times 10^4$ N/m	$\approx 2 \times 10^4$ N/m
Color	Translucent	Transparent
Service temp.	-50°C – 230°C	-45°C – 200°C
Curing temp.	25°C	25°C – 150°C
Viscosity before curing	≈ 50 (toothpaste-like)	≈ 3.5 (tooPa·s (honey-like)
Compatibility with brine	Compatible	Compatible

Here is a detailed explanation on how to determine whether a polymeric material is soft enough. A layer of polymer on the top of the pressure sensor diaphragm can be roughly considered as two springs in parallel, as two layers share the same displacement change. Each layer has its own spring constant. For the pressure sensor diaphragm, which has a touch-mode transition around 15 MPa, the spring constant is estimated from the non-touching regime. At pressure of 10 MPa, the center displacement of diaphragm is designed to be 0.745 µm, as the diameter of the diaphragm is 100 µm, the formula to calculate the spring constant of diaphragm is:

$$k_{sensor} = \frac{Force}{Displacement} = \frac{\pi(d/2)^2 P}{y} \tag{3.1}$$

where k_{sensor} is the spring constant of the pressure sensor diaphragm, P is the applied pressure, d is the diameter of diaphragm, and y is the center deflection. Inserting in all the data, the spring constant of the diaphragm is:

$$k_{sensor} = \frac{10\text{MPa} * \pi * (100\mu\text{m}/2)^2}{0.745\mu\text{m}} = 1.05 \times 10^5 \text{ N/m} \tag{3.2}$$

The spring constant of the polymer layer can be estimated as the applied force divided by the change of polymer thickness. The polymer layer can be considered as a combination of a polymer cylinder on the top of the pressure sensor diaphragm and the rest part confining it. When pressure is applied, the polymer cylinder is deformed because of material compression. Due to the confinement from adjacent polymer, the polymer cylinder can only deform vertically. The relationship between the deformation and applied pressure is:

$$\Delta l = \frac{P}{B} l \tag{3.3}$$

where Δl is the polymer deformation, P is the applied pressure, l is the polymer thickness, and B is the bulk modulus. Therefore, the spring constant of the polymer cylinder is:

$$k_{polymer} = \frac{Force}{Displacement} = \frac{\pi(d/2)^2 P}{\Delta l} = \frac{\pi(d/2)^2 B}{l} \tag{3.4}$$

Typical polymer thickness in the package design is l = 0.75 mm, and the diameter of the pressure sensor used is d = 0.1 mm. The typical bulk modulus of silicone at 50 MPa is about 2 GPa, and for epoxy is about 5 GPa [Smi73]. Inserting in the data above, the spring constants of silicone and epoxy are about:

$$k_{polymer} = 2.09 \times 10^4 \text{ N/m} \tag{3.5}$$

$$k_{epoxy} = 5.24 \times 10^4 \, \text{N/m} \tag{3.6}$$

Compared with the spring constant of the pressure sensor which is $k_{sensor} = 1.05 \times 10^5 \, \text{N/m}$, it is clear that $k_{silicone}$ is only about 20% of k_{sensor}, while k_{epoxy} is about 50% of k_{sensor}. Therefore, if the polymer layer above the pressure sensor is epoxy or other hard polymers, it will have larger effect on the pressure sensor response than silicone. This leads to two problems. First, the thickness of the polymer layer affects the pressure sensor response after packaging. This requires a precise control in polymer layer thickness, which will increase the complexity in manufacturing. Second, the temperature coefficients of the polymer layer will add to the temperature coefficients of the pressure sensor. Furthermore, the temperature coefficients of the polymer layer are also thickness-dependent, making it more troublesome in sensor calibration. In brief, a soft polymer like silicone is essential to mitigate the impact of unit-to-unit variations in the thickness of the polymer and to reduce the temperature coefficients of the polymer-encased pressure sensor.

3.3. Modeling of Polymer-in-Tube Package

The goals of package modeling can be categorized into mechanical and electrical aspects. In mechanical aspect, first is to examine package integrity at target pressure and temperature, and second is to estimate the efficiency of pressure transfer to pressure sensor through package. In electrical aspect, first is to estimate the parasitic capacitance, and second is to examine how the package materials and various environmental conditions affect it. The same model implemented in COMSOL® 5.0 was used for both aspects.

3.3.1. Model Setting and Hyperelastic Material Model

As shown in Figure 3.4, the package structure contains a tube, a block representing the folded ELM2.0 system stack at the center, and a polymer filler between the tube and the block. On the top surface of the block are two pads representing the pads to mount the pressure sensor. The detailed pressure sensor structure was not included, because its diameter was only 0.1 mm, much smaller than the package size of 9.5 mm. The tube was either stainless steel or alumina ceramic, the block was polyimide, and the polymer filler was silicone. Since the mechanical properties of silicone caulk and PDMS were very similar, they were considered as one material in modeling. Properties of these materials used in the simulation are listed in Table 3.3. Since the package structure was symmetric about three axes, only one-eighth (1/8) segment of the structure was used for simulation.
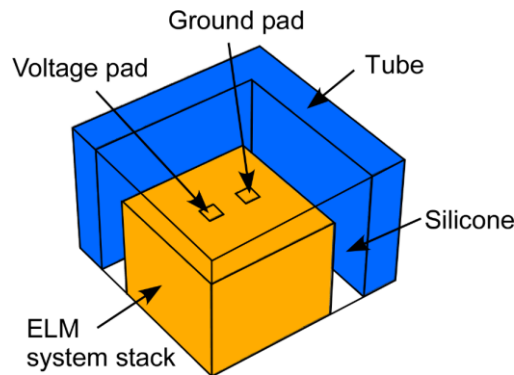
Figure 3.4: One-eighth segment of the symmetric package structure for FEA modeling

Pressure up to 50 MPa was applied on all the exterior surfaces. For high temperature simulations, thermal expansion up to 125°C was applied to the polymer filler only, because the thermal expansion coefficients of stainless steel (10 ppm/°C), alumina ceramic (8 ppm/°C), and polyimide (20 ppm/°C) were significantly smaller than that of silicone (300 ppm/°C). The temperature dependence of relative permittivity of silicone

and polyimide was considered. Other material properties were assumed to be constant from room temperature to 125°C. This is a reasonable simplification, because for stainless steel and ceramics, the temperature dependency of these properties can be negligible in this temperature range, and for silicone, this temperature range is well beyond its glass transition temperature ($T_g \approx$ -125°C [Gub07]). For electrical modeling, the parasitic capacitance was acquired between two pads on the top surface of the block. All dimensions used in modelling approximated actual sample.

Table 3.3: Materials properties used in modeling of polymer-in-tube package

Material	Material Model	Parameters	Source of Properties
Stainless Steel	Linear elastic	Density 7850 kg/m^3 Young's modulus 205 GPa Poisson's ratio 0.28	COMSOL built-in material
Alumina Cceramic	Linear elastic	Density 3900 kg/m^3 Young's modulus 300 GPa Poisson's ratio 0.22 Relative permittivity 9.1	[Web-Acc]
Silicone	Hyperelastic	Mooney-Rivlin parameters: c_{10} = 0.14 MPa, c_{01} = 0.023 MPa Initial bulk modulus 2.2 GPa Density 970 kg/m^3 Relative permittivity: RT 3, 125°C 2.69 Thermal expansion 310x10^{-6}/K	[Meu08, Joh14, Nol68]
Polyimde	Linear elastic	Density 1300 kg/m^3 Young's modulus 3.1 GPa Poisson's ratio 0.34 Relative permittivity: RT 3.4, 125°C 3.2	COMSOL built-in material [Web-Dup]

It is worthwhile to emphasize that the material model used for the silicone is hyperelastic material instead of linear elastic material. This is because a linear elastic modulus of 1 MPa, which is typical for silicone at low force values, is not suitable to describe the stress-strain relationship in silicone under high pressure, such as 50 MPa. Therefore, a hyperelastic material model has to be used. The hyperelasitc material model defines an elastic material by energy elastic strain energy density W_s, and the stress-strain

relationship is derived from it. Details about the relationship and its derivation are illustrated in the Appendix.

The COMSOL® 5.0 has several built-in hyperelastic material models. The Mooney-Rivlin model is used in the simulations in this chapter, as it corresponds well with experimental results and has low computational burden [Mar06, Meu08]. The energy elastic strain energy density W_s in this model is:

$$W_s = C_{10}(I_1 - 3) + C_{01}(I_2 - 3) + \frac{1}{2}B(J_{el} - 1)^2 \qquad (3.7)$$

where C_{10} and C_{01} are material parameters related to hyperelasticity, B is the initial bulk modulus which is also a material parameter, whereas I_1, I_2, and J_{el} are variables related to deformation. Definitions of I_1, I_2, and J_{el} are given in the Appendix. Values of the three material parameters used in the simulations are listed in Table 3.3.

3.3.2. Mechanical Behavior at Target Temperature and Pressure

The deformation and stress distribution of the package were modeled under three conditions: at the target pressure (50 MPa) only, at the target temperature (125°C) only, and at the combined target temperature and pressure (125°C and 50 MPa). The simulation results are shown in Figure 3.5. In this simulation the tube material was stainless steel. Ceramic tube gave similar results, and therefore was not repeated here.

The deformation mainly occurred in the silicone filler. With 50 MPa pressure at room temperature, the silicone was deformed inward; the maximum deformation was 157 μm, located between the tube and the system stack. At 125°C, without applying pressure, the silicone expanded outward. A ridge was formed between the tube and the system stack,

and the maximum deformation there was 399 µm. Comparison of the conditions showed that the thermal expansion and pressure had the opposite effect on silicone deformation. In the combined HT/HP condition, thermal expansion had larger effect than the high pressure, as the silicone between the tube and the system stack was deformed outward. The maximum deformation was 252 µm, smaller than the condition with high temperature only.

The Von Mises stress distribution in the tube and in the silicone are shown separately in Figure 3.5. In the tube, the maximum stresses under the three conditions were 24.4 MPa (at the target pressure), 80.3 MPa (at the target temperature), and 49.5 MPa (at the target temperature and pressure). They are located at the inner corners of the tube. For all the three conditions, the maximum stresses are much smaller than the yield stress of SS 304 (205 MPa [Web-Sta]). In the silicone filler, the maximum stresses are 0.298 MPa (at target pressure), 1.09 MPa (at target temperature), and 0.586 MPa (at the target temperature and pressure). They are located at the surfaces attached to the tube. These values are much lower than the compressive strength of silicone (at least 10 MPa [Web-Sil]).

These simulation results indicate that the package will not be damaged by the target temperature and pressure, but the silicone filler will have deformation in the order of hundreds of microns, which is acceptable.
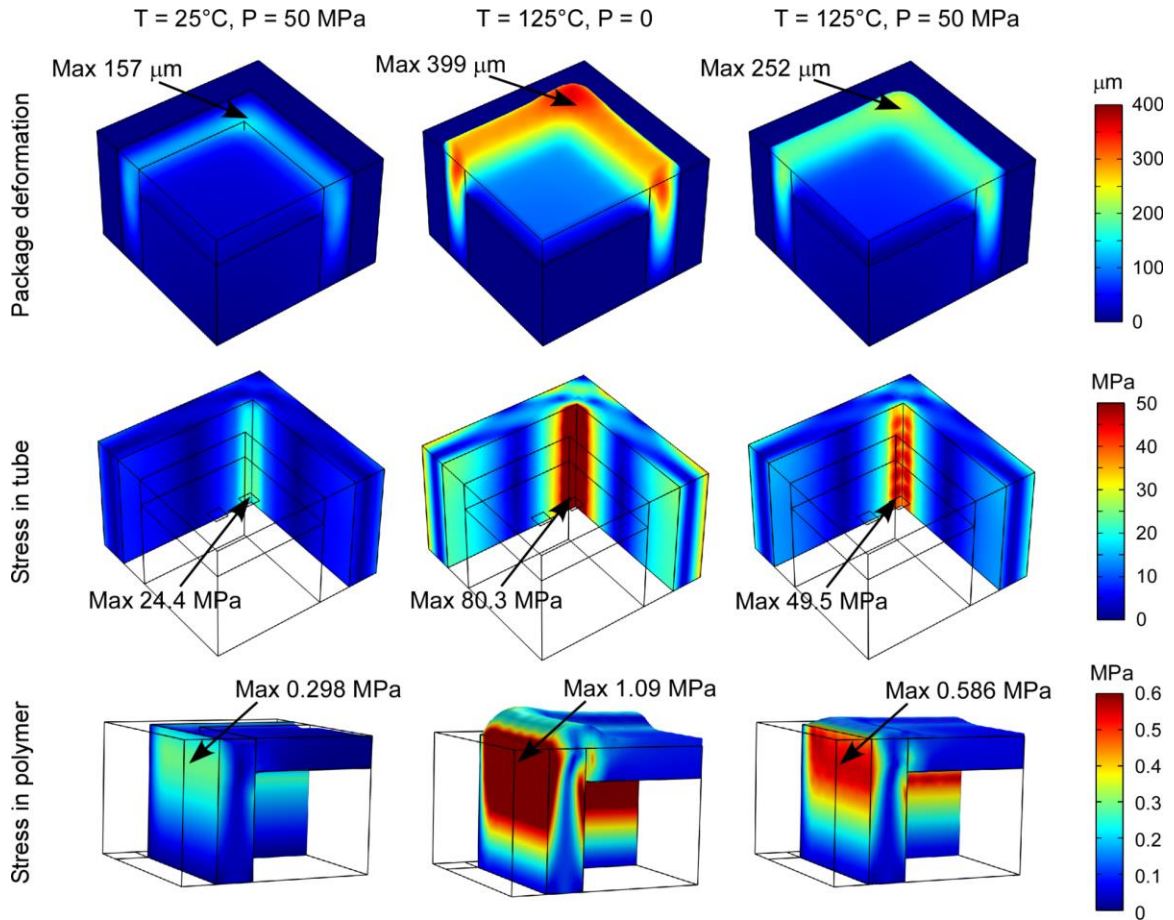
Figure 3.5: Simulation results of package mechanical behaviors under HP, HT, and combined situation. Deformation in all the images are exaggerated by 2 times.

The external pressure transferred to the pressure sensor location through the silicone was also investigated. To determine the proper parameter describing the transferred pressure, it is necessary to clarify how the pressure transfer occurs. The external pressure first deforms the silicone layer, and stress is generated inside the silicone layer. To balance this, the system stack surface and the pressure sensor diaphragm beneath the silicone layer are deformed and stressed. In this process, the normal stress in z direction (σ_{zz}), which is perpendicular to the pressure sensor diaphragm, plays the role of "pressure" that deforms it. Therefore, the effective pressure transferred through the silicone can be represented by σ_{zz} at the contact surface. The distribution of σ_{zz} on this surface at room

temperature and at 125°C with 50 MPa applied pressure are shown in Figure 3.6 (a) and
(b), respectively. The pressure sensor diaphragm is in the rectangular areas surrounded by
the dashed grey lines. In this area, the average stress is 49.90 MPa, which means 99.98%
of external pressure is transferred to the pressure sensor.
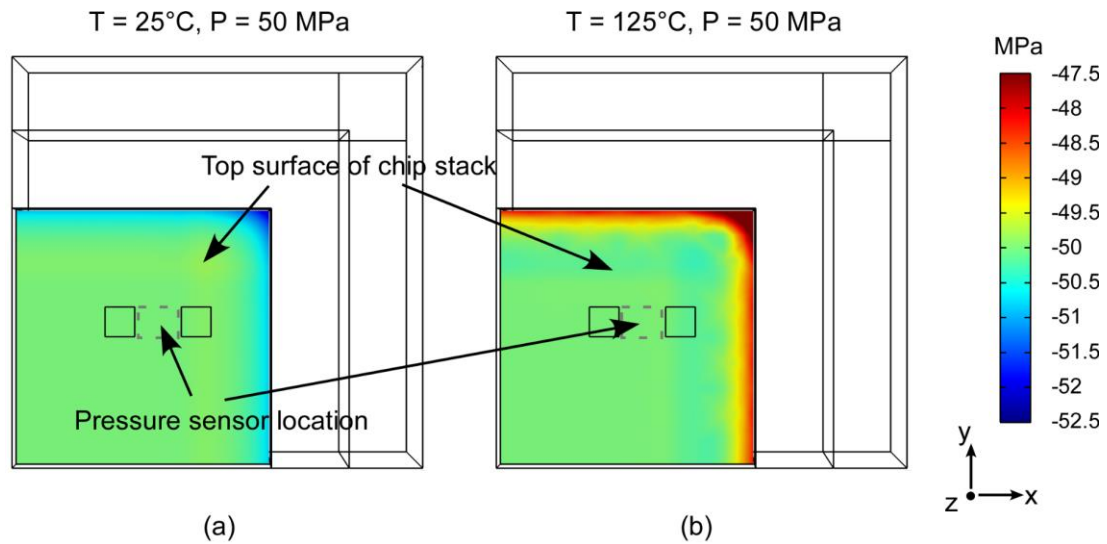
Figure 3.6: The normal stress (σ_{zz}) distribution on the system stack surface: (a) at 25°C,
under 50 MPa pressure; (b) at 125°C, under 50 MPa pressure. The rectangular areas
surrounded by the dashed grey lines are pressure sensor locations.

3.3.3. Effects on Parasitic Capacitance from Package and Environmental Factors

In the ELM system, the capacitance measured across the two metal pads of the
pressure sensor is actually the summation of two components: the capacitance from the
pressure sensor diaphragm and parasitic capacitance from the surroundings. The ELM
system cannot distinguish between the two components. Since the total capacitance change
will be interpreted as pressure change, the change from parasitic capacitance can affect the
pressure measurement results. Therefore, it is important to evaluate the change of parasitic
capacitance when the environmental factors change, and minimize the change as much as
possible.

The factors affecting the parasitic capacitance fall into two categories: environmental factors and package factors. Environmental factors include temperature, pressure, and conductivity of the ambient fluid (e.g. brine). At high temperature, the dielectric constants of silicone and polyimide change, and the expansion of silicone may change the electric field lines and further affect parasitic capacitance. At high pressure, the silicone is deformed, which may also change the parasitic capacitance. Since the brine is conductive, the exterior surfaces of the package will be at the same electric potential, which results in redistribution of the electric field lines. The package factors include the tube materials and electrical connection with the ELM system stack. Three conditions are of particular interest: stainless steel tube without electrical connection ("SS floating"), stainless steel tube with electrical connection ("SS grounded"), and ceramic tube without electrical connection ("ceramic"). The condition of using a ceramic tube with an electrical connection is not considered because ceramic is not conductive. With different package conditions, the degree to which the environmental factors affect parasitic capacitance may be different.

A summary of the parasitic capacitance in the 24 combined environmental and package conditions is listed in Table 3.4. The parasitic capacitance at room temperature, no pressure, and no brine condition can be treated as a basic capacitance (C_0) for each package condition. For easier comparison, the capacitance differences between each environmental condition and C_0 are also listed. For the three package conditions, SS floating and ceramic conditions not only have low C_0 (32.62 fF and 32.49 fF) but also have low capacitance change (3.71 fF and 3.81 fF) in different environment conditions, while SS grounded condition has significantly larger C_0 (51.14 fF) and capacitance change (13.23

fF). The difference in C_0 can be illustrated by the electric field lines distribution (Figure 3.7). In the SS floating and ceramic conditions (Figure 3.7a and c), the electric field lines start from one pad and terminate at the other one; while in SS grounded condition (Figure 3.7b), the lines still start from one pad but terminate at both the other pad and the SS tube. Therefore, the SS grounded condition has a larger effective pad area, resulting in a larger C_0.
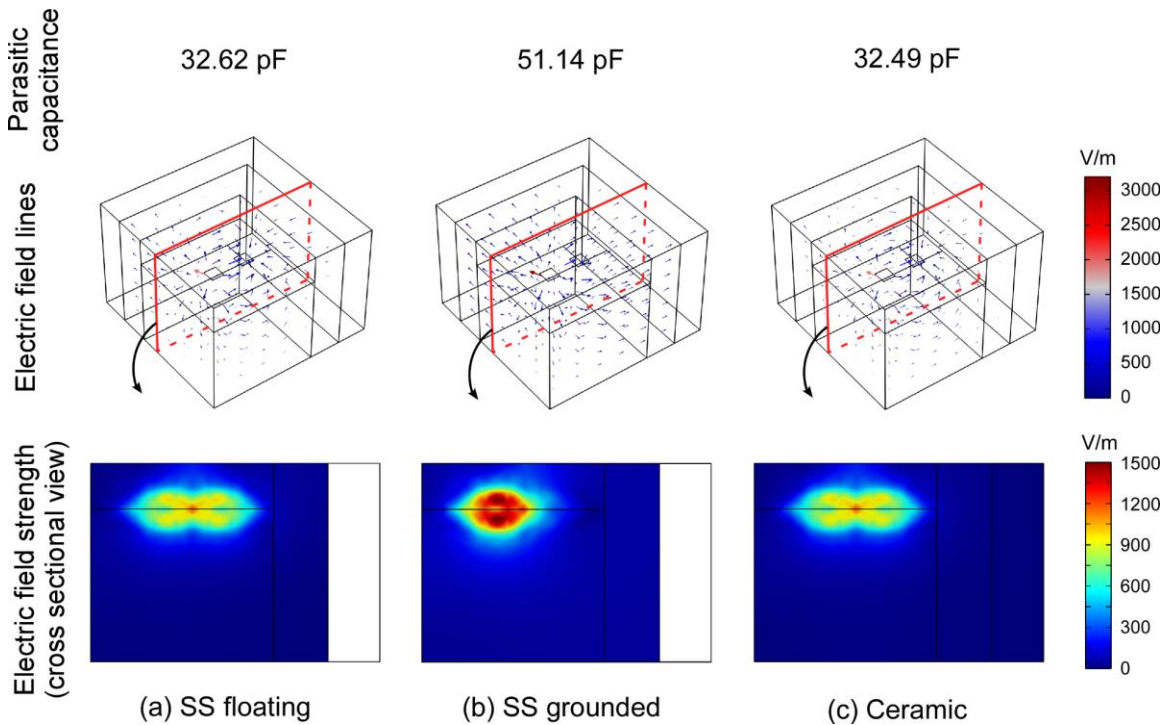
Figure 3.7: The 3D view of electric field lines and cross sectional view of electric field strength in three package conditions: (a) SS floating; (b) SS grounded; (c) ceramic. Environment conditions are 25°C, no pressure, and no brine. In these, (b) has the largest parasitic capacitance (C_0).

In the SS grounded condition, the large capacitance change is mainly contributed by brine (≈9 fF); high temperature has a small contribution (≈3 fF), while high pressure has a very limited effect (≈0.5 fF). Unlike this, in the SS floating and ceramic conditions,

the capacitance change from brine is only about 1 fF, making it less significant than temperature (capacitance change ≈2 fF), but more significant than pressure (≈0.2 fF).

Table 3.4: Summary of parasitic capacitance in different environmental and package conditions

| | | | | Package Factors | | | | | |
| | | | | SS Floating | | SS Grounded | | Ceramic | |
	Temp.	Brine	Pressure	$C_{parasitic}$ (fF)	$\Delta C_{parasitic}$ * (fF)	$C_{parasitic}$ (fF)	$\Delta C_{parasitic}$ * (fF)	$C_{parasitic}$ (fF)	$\Delta C_{parasitic}$ * (fF)
Environment Factors	25°C	w/o Brine	0	32.62	0	51.14	0	32.49	0
		Brine	50 MPa	32.40	-0.22	50.61	-0.53	32.28	-0.21
		w/ Brine	0	33.79	1.17	60.61	9.47	33.78	1.29
			50 MPa	33.66	1.04	60.43	9.29	33.65	1.16
	125°C	w/o Brine	0	30.27	-2.35	47.83	-3.31	30.16	-2.33
		Brine	50 MPa	30.08	-2.54	47.38	-3.76	29.97	-2.52
		w/ Brine	0	31.03	-1.59	55.08	3.94	31.02	-1.47
			50 MPa	30.89	-1.73	54.90	3.76	30.88	-1.61
Max. $C_{parasitic}$ Change (fF)				3.71		13.23		3.81	

*$\Delta C_{parasitic}$ is the capacitance difference with the first environmental condition (25°C, w/o brine, and no pressure)

Pressure has little effect in all package conditions, because the high electric field zone is away from the significantly deformed zone (Figure 3.8). Temperature can change about 7% of the parasitic capacitance in all package conditions, mainly because of the decrease in dielectric properties of silicone and polyimide at high temperature.
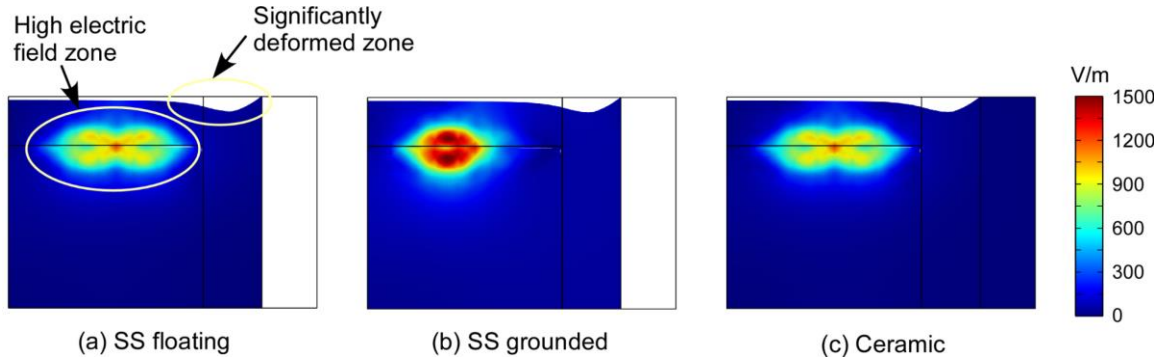
Figure 3.8: Cross sectional view of electric field strength in three package conditions: (a) SS floating; (b) SS grounded; (c) ceramic. Environment conditions are 25°C, 50 MPa pressure, and no brine. Pressure has little effect in parasitic capacitance, because the high electric field zone is away from the significantly deformed zone.

Brine has the largest effect in SS grounded package, but has low effect in the other two package conditions. The reasons are as follows. The way that brine changes parasitic capacitance is by re-distributing electric field, as the conductive brine forces equal electric potential on exterior surfaces. Without brine, SS grounded package has lager potential difference on exterior surface than the other package conditions (Figure 3.9). As can be seen in the figure, the potential distribution changes significantly in the presence of brine in SS grounded package.
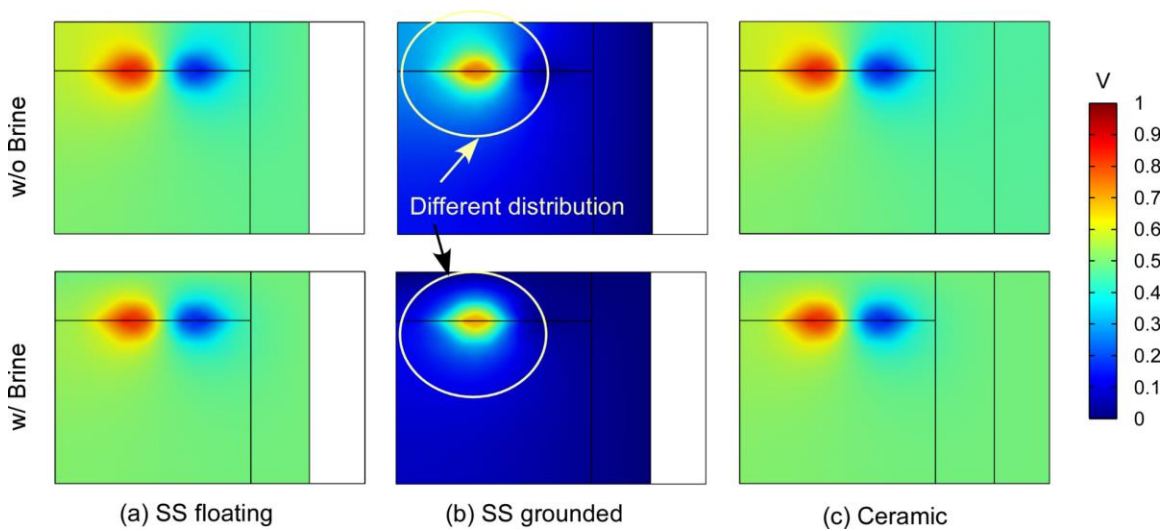
Figure 3.9: Brine effects on electric potential distribution (cross sectional view) at the following package conditions: (a) SS floating; (b) SS grounded; (c) ceramic. Environment conditions are 25°C and no pressure.

As the parasitic capacitance of the SS floating and ceramic package is more resistant to environmental factors change, these two package conditions are selected.

3.4. Packaging Process

Two types of tube (SS 304 and alumina ceramic) were used to package the ELM systems. The SS tubes were cut into designed lengths from an off-the-shelf long tube (American Stainless Steel Tubing, Inc, NC, USA) by a commercial wire EDM service

(MILCO Wire EDM, CA, USA). The alumina ceramic tubes were custom manufactured to designed length (LSP Industrial Ceramics, Inc, SC, USA). The filling polymer also had two types, which were the caulk and the PDMS, as described in Section 3.2.3. Although the PDMS had some undesirable features including high permeability to moisture and weak adhesion to many materials, it was still used in some packages because of the following advantages. First, it had very low viscosity before curing, which was desirable for filling folded PCB structures. Second, cured PDMS was very clear and transparent, so it did not impede optical communication between the embedded electronics and external systems. The packaging process flows for the caulk and the PDMS were slightly different.

The packaging process with caulk is shown in Figure 3.10 (a). In Step 1, the tubes are arranged in an array on a flat substrate. Then in Step 2, the bottom of each tube is covered with a small amount of caulk. In Step 3, the ELM stacks are placed inside the tubes and inserted into the caulk. Since caulk has a high viscosity, the ELM stacks do not fall down and touch the substrate even though the caulk is not cured. In Step 4, the tubes are flipped over to allow the caulk contacting air for curing. In Step 5, after the caulk is cured, the tube is flipped back on the substrate and filled up with more caulk. After the second caulk is cured, the packages can be removed from the substrate, finishing the packaging process.

The packaging process with PDMS is shown in Figure 3.10 (b). In Step 1, the tubes are arranged in an array on a flat substrate coated with a demoulding film. In Step 2, the bottom of each tube is covered with a small amount of PDMS, which is then partially cured. The partially cured PDMS can support the ELM stacks placed in Step 3 and also form a better bond with following PDMS. In Step 4, an additional small amount of PDMS is

added into each tube and degassed under vacuum. In Step 5, more PDMS is added to fill up the tube. After curing the PDMS, the packages can be released from the substrate. Some packages with PDMS fillers are coated with an UV curable epoxy coating for additional protection against chemicals. This epoxy was based on EPON^{TM} Resin SU-8 but further customized by RTI International (Research Triangle Park, NC, USA). It can be peeled off after HPHT tests.

Photos of ELM systems after packaging in the polymer-in-tube packages are shown in Figure 3.11.

Step 1: Align tubes on a flat substrate

Caulk

Step 2: Deposit a base layer of caulk

ELM stack

Step 3: Place ELM stacks in tube

ELM stack

Step 4: Flip over the tubes and cure the caulk

Step 5: Flip the tubes back, fill up the top part with more caulk and cure it

Step 6: Release packages from substrate

(a)

Step 1: Align tubes on a flat substrate coated with a demoulding film

PDMS

Step 2: Deposit a base layer of PDMS and partially cure it

ELM stack

Step 3: Place ELM stacks in tubes

ELM stack

Step 4: Add more PDMS and vacuum them to degas

Step 5: Fill up the top part with more PDMS and cure it

Step 6: Release packages from substrate and apply optional UV curable coating

(b)

Figure 3.10: Process flow of integrating ELM stacks into the polymer-in-tube package: (a) with silicone caulk as the filling polymer; (b) with PDMS as the filling polymer
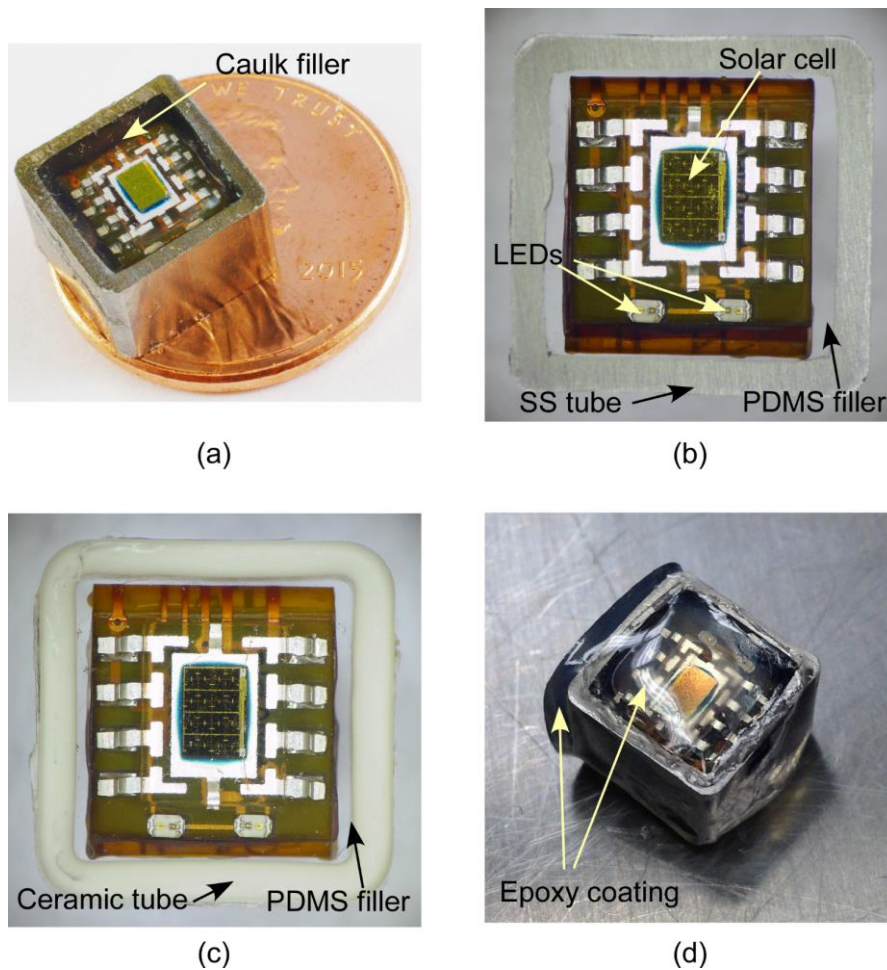
Figure 3.11: ELM systems after packaged in polymer-in-tube packages: (a) SS tube and caulk filler; (b) SS tube and PDMS filler; (c) ceramic tube and PDMS filler; (d) SS tube and PDMS filler with epoxy coating.

3.5. Test Results and Discussion

3.5.1. Combined High Temperature and High Pressure Test Results

Packaged ELM systems were tested at combined high pressure and high temperature (HPHT) conditions at RTI International (Research Triangle Park, NC, USA) on July 27-28, 2016. The test equipment was HPHT Consistometer Model 275 (Fann Instrument, Houston, TX). The target HTHP condition was 125°C and 50 MPa, with a hold time between 5 min to 1 h. The ramping up and ramping down time for both

temperature and pressure was about 30 min. In each test, the packaged ELM systems were double bagged in individual test pouches filled with test media. Three types of test media were used for the HPHT tests: silicone oil, API brine, and Isopar™-L. In these, silicone oil provides a chemically inert environment with HPHT condition, API brine is the simulated environment for the target applications, while Isopar™-L is of interest to other potential oil-well applications. The details of these media are listed in Table 3.5.

Table 3.5: Three types of test medium used in the HPHT tests.

Testing medium	Description
Silicone Oil*	Liquid silicone oil, non-conductive, chemical inert
API Brine*	$CaCl_2$ 2 wt% + NaCl 8 wt%
Isopar™-L#	Synthetic isoparaffinic hydrocarbon solvent from Exxon Mobil

*In specification. #Beyond specification.

In summary, the packaged ELM 2.0 systems survived the target HPHT conditions (125ºC and 50 MPa in API brine). A total of 18 packaged ELM 2.0 systems were tested. Detailed test results are summarized in Table 3.6. Photos of two packaged ELM 2.0 systems after HPHT tests in API brine are shown in Figure 3.12.

Packaged ELM 2.0 systems with caulk filler survived the HPHT tests in API brine. The packaged ELM 2.0 systems with PDMS can survive HPHT tests in silicone oil; for API brine environment, the ones with additional epoxy coating can survive, while the ones without coating became malfunctioned after the tests. Although the epoxy coating improved the protection against brine, it could not prevent chemical attack from Isopar™-L, as none of the packaged ELM 2.0 systems survived HPHT tests in Isopar™-L. Packaged ELM 2.0 systems with caulk were not tested in Isopar™-L, but based on the fact that silicone materials can be attacked by hydrocarbons, they would unlikely survive.

Table 3.6: Summary of the HPHT test results of the Packaged ELM 2.0 systems

Package Information[*]	Test medium	Number of ELMs Tested	Number of Tests	Failure due to package
Caulk	API brine	2	6	0/6
PDMS	Silicone oil	9[**]	11	0/11
	API brine	1	1	1/1
	Isopar™-L	1	1	1/1
PDMS with coating	API brine	4	4	1/4
	Isopar™-L	2	2	2/2

[*] Tube material has no effect in failure, therefore is not specified here.
[**] After the test, one of the packages was coated with epoxy and reused in API brine test.

(a)   (b)
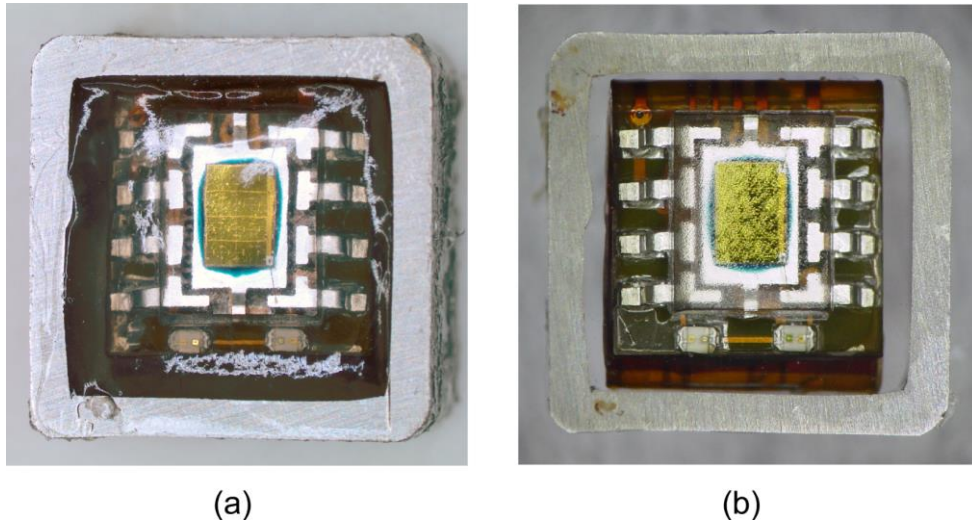
Figure 3.12: Packaged ELM systems after HPHT test in API brine: (a) package filled with caulk; (b) package filled with PDMS, and protected by epoxy coating during the test (the coating was peeled off after test for data retrieval). Photos were taken at least 4 hours after the test.

3.5.2. Discussion of Package Failure Types

Two types of package failure or and two types of package compromise were found after the HPHT tests. The first failure type was brine leakage which only occurs in packages with PDMS filler. Compared to the caulk, PDMS has much weaker adhesion to the tube materials and ELM stack surface. Under pressure, brine may go into the seam between the tube and PDMS filler. If the ELM stack is completely encapsulated inside

70

PDMS layer, the brine cannot reach ELM stack and affect its function. However, if the ELM stack touches the tube, a leakage path is created for brine. Figure 3.13 shows the leakage path in one package after pressurizing at 50 MPa for 1 h in DI water with blue dye. This leakage issue significantly reduces the package reliability under HPHT in brine. The same issue seldom occurs in packages with caulk filler, because the caulk can adhere well to both the tube and the ELM stack, preventing the brine from getting in.
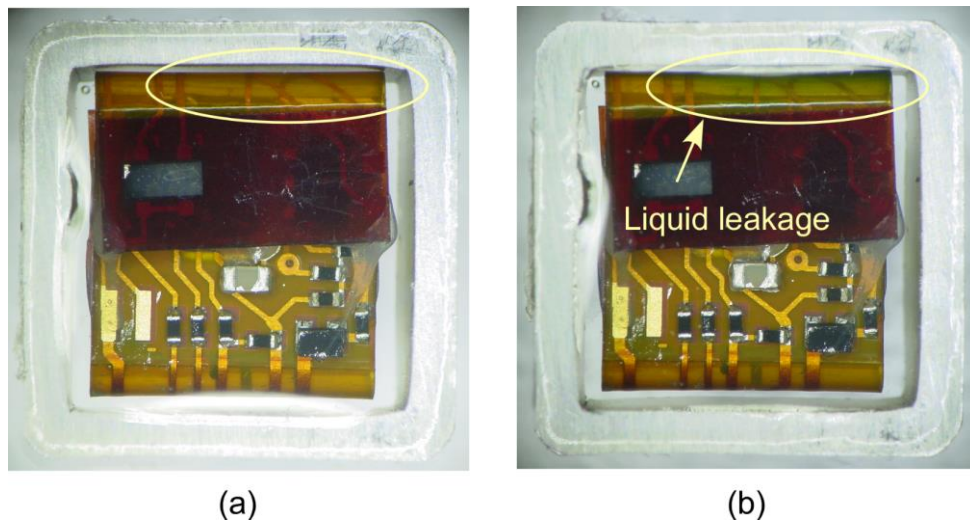
Figure 3.13: Leakage path in package with PDMS filler at where ELM stack touches tube. Photos of a package with PDMS filler: (a) before any test; (b) after pressurized at 50 MPa for 1 h in DI water with blue dye.

The second failure type is chemical attack from test media. Isopar™-L, which is a type of synthetic hydrocarbon solvent, can damage PDMS even in short term (Figure 3.14). When the packages were inspected in laboratory condition after the test, the PDMS fillers expanded by about 50% in volume compared to their pre-test volume in laboratory condition. The damage is mainly because silicone materials have large volume expansion after exposure to non-polar hydrocarbons, although silicone material does not decompose or dissolve [Web-Cha].
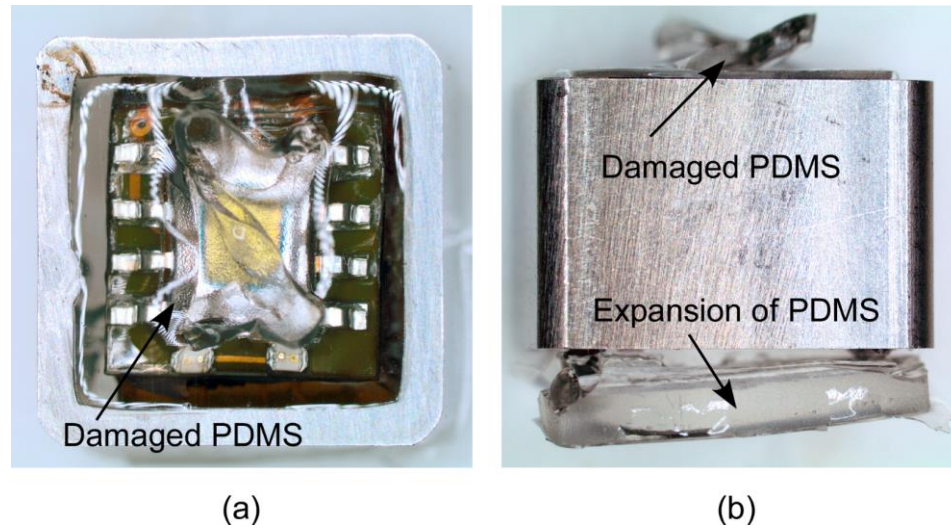
Figure 3.14: Photos of a package damaged by Isopar^{TM}-L after HPHT test: (a) top view; (b) bottom view.

The first compromise type is that the silicone becomes less transparent after long time exposure to hot brine. This does not affect the optical communication in a short duration of a few hours. One of the packaged ELM system with caulk filler was able to report data after two HPHT tests in API brine (one with 5 min hold, the other with 1 h hold, total of 3 h including ramping time). Another one with caulk filler could report data after 16 h in 80°C API brine at atmospheric pressure (shown in Figure 3.15).
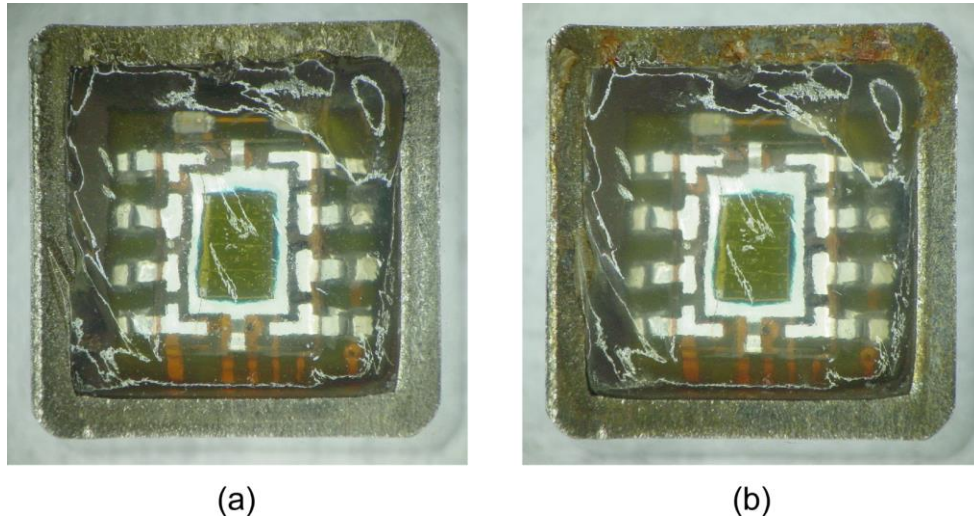
Figure 3.15: A packaged ELM system with caulk filler: (a) before any brine test; (b) after 16 h in 80°C API brine at atmospheric pressure. After test, the caulk becomes less transparent, and the SS tube becomes rusty.

The second compromise type is the bulge of silicone layer, which usually disappears over time and does not affect the ELM system function. While this happened to all types of packages and in all types of test media, the packages with additional epoxy coating had less chance of this issue. The bulge may appear on either one side or two sides, with height ranging from ≈0.5 to 2 mm. Photos of a typical bulge are shown in Figure 3.16. The cause of this failure is likely the air diffusion into silicone layer under HPHT. When the packaged ELM systems were double-bagged in individual pouches for test, air bubbles were not completely eliminated. Silicone materials in general have large gas permittivity, and the HTHP condition also facilitates the diffusion process [Ger01]. With a large amount of gas diffused in silicone, if the environment pressure decreases quickly, rapid gas expansion may result in damage in silicone. This phenomenon is known as explosive decompression, which poses a concern in prolonged HTHP applications [Ski04].
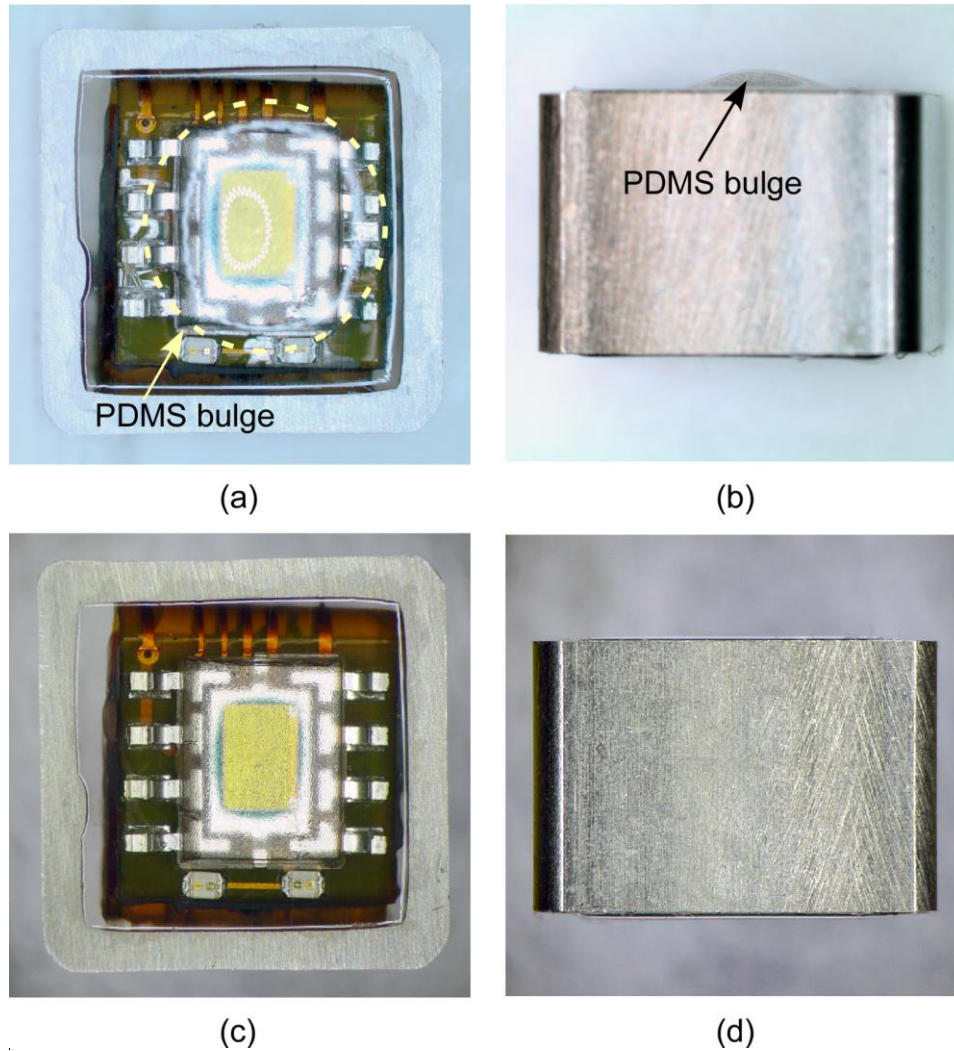
Figure 3.16: Photos taken right after the test and showing the bulge of silicone layer: (a) top view; (b) side view. Photos of the same package after a few days: (c) top view; (d) side view.

3.6. Summary

Polymer-in-tube packages were designed to protect ELM systems in downhole environment while allowing pressure measurement. The packages consisted of hard tubes made of SS or ceramic, and soft fillers made of caulk or PDMS. Some of the packages with PDMS fillers also had an epoxy coating for additional protection against chemicals. The mechanical behaviors and parasitic capacitance of the packages were carefully

investigated by simulations. ELM systems in the packages with caulk fillers survived combined HPHT conditions at 50 MPa and 125°C in API brine, and successfully performed the temperature/pressure logging and reporting functions during the HPHT tests. The successful test results suggest that this packaging approach is promising for microsystems in downhole applications.

CHAPTER 4:

POLYMER FILM ENCAPSULATION APPROACH TO PROTECT

MICROSYSTEM FROM CHEMICALS

The variety of chemicals found in downhole ambient conditions presents a significant challenge for packaging microsystems. For example, brine and hydrocarbons, which have vastly different chemical properties, may attack the system package and eventually affect the microsystems in different ways. To prevent such attacks, a bi-layer coating consisting of ALD alumina and Parylene-C^{TM} is applied to the sapphire-on-SS packages as described in Chapter 2. This coating successfully protects the packages from chemicals including brine, hydrocarbons, and cement slurry, but still has some limitations. For example, it can compromise the clarity of certain options for the optical window. Additionally, this coating is incompatible with system packaging that permits the transmission of pressure. To address these limitations and to achieve a general approach of chemical protection, this chapter aims at evaluating a thin film encapsulation approach. Chemically inert transparent thin films wrapped around the microsystems can form a protective barrier against chemicals, while allowing optical communication and pressure transfer. Such polymer films encapsulation can support packages in Chapter 3 with significantly higher chemical resistance, and can also be an alternative for the Al_2O_3 and Parylene-C^{TM} bi-layer coatings for packages developed in Chapter 2. The film material

selection, encapsulation process, and test results of this approach are presented in this chapter.

4.1. Motivation

The ALD alumina and Parylene-C^{TM} bi-layer coatings developed in Chapter 2 have been proved to protect packages from multiple chemical environments, including brine, hydrocarbons, and cement slurry, without any degradation in the packages. However, there are still several limitations. First, it is difficult to form a continuous Parylene-C^{TM} coverage all around the package, which requires special holding structures during the coating process and two consecutive coating sessions. Second, this coating strategy cannot be applied to the polymer-in-tube packages developed in Chapter 3, because the Parylene-C^{TM} coating can significantly reduce the transparency of silicone (Figure 4.1a and b), and the large deformation of silicone under high pressure can stretch and degrade the Parylene-C^{TM} layer (Figure 4.1c). Third, Parylene-C^{TM} coating needs specific facilities, increasing the cost of packaging process. Uncoated polymer-in-tube packages can survive in brine, but can be severely attacked by hydrocarbons and acids. Therefore, it is necessary and important to find a better approach to protect the microsystems against these chemicals in environments.
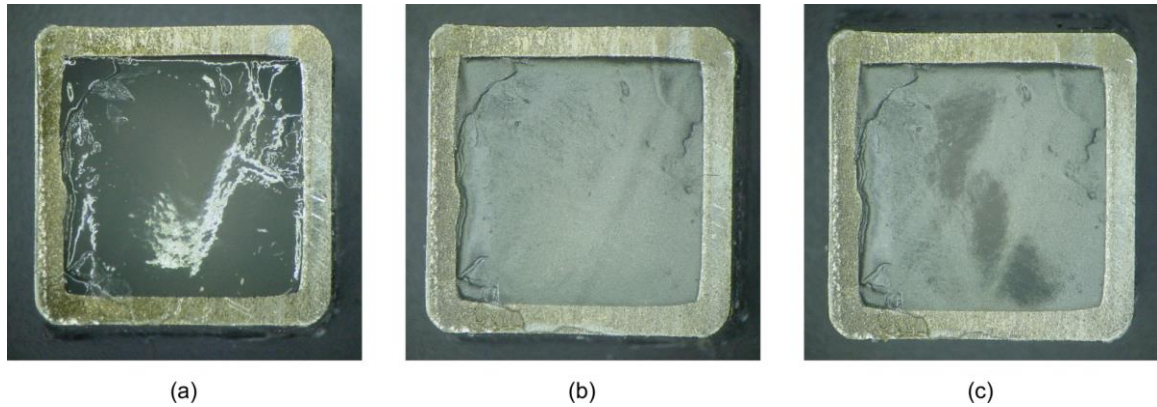
Figure 4.1: A SS tube filled with silicone caulk: (a) before any coating, the silicone is translucent; (b) after coating with Parylene-C^{TM}, the silicone becomes much less transparent; (c) coated package after high pressure test at 50 MPa, some part of the Parylene-C^{TM} is stretched.

One approach is to replace the silicone with curable epoxies. However, epoxies that can serve at high temperature and with good chemical resistance generally require high temperature for curing as well. Considering the epoxy fills the entire depth of the tube, curing will take long time to ensue all the solvents to evaporate out. This long time baking at high temperature will significantly degrade the batteries in microsystems, and has to be avoided. Also, epoxies have higher bulk modulus than silicone, and as discussed in Chapter 3, this will increase the temperature dependence of pressure sensors being encapsulated.

Instead of replacing silicone with epoxy, the microsystem can by protected with a polymer film encapsulation. Unlike the Parylene-C^{TM} coating, the polymer film does not adhere to the package or the stack, and therefore can allow relatively large deformation. This approach can be combined with different package designs to significantly improve chemical resistance. Depending on the specific package design, the film can be either outside the entire system package, or outside the microsystem stack. With the advantages

of versatility, low cost, and keeping the microsystem stack at room temperature, this polymer film encapsulation approach is selected to proceed in this Chapter.

4.2. Design of Film Encapsulation

The protective film encapsulation approach can be incorporated within the system package in two ways.

The first way is to encapsulate the microsystem stack with the protective polymer film (Figure 4.2a). Soft silicone polymer can be applied only on the pressure sensor part or the entire microsystem stack before the film encapsulation. The polymer film can be heat sealed, and during this process vacuum can be applied to remove trapped air. This film encapsulation can provide chemical protection and allow pressure transfer to the microsystem, but cannot provide mechanical protection. It is suitable if abrasion and impact are of less concern in the target application.

The second way is to encapsulate the microsystem stack with the film and insert it into a tube (Figure 4.2b). This is an improved version of the polymer-in-tube package with better chemical resistance. The stack inserted into the tube can stay there in actual deployment because hydrostatic pressure cannot generate imbalanced force to push it out. The tube can protect the encapsulated microsystem stack from abrasion and impact.
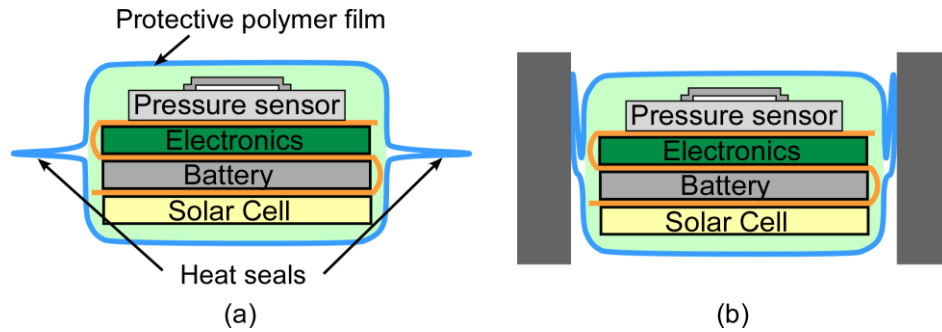
Figure 4.2: Two ways of protective film encapsulation: (a) encapsulate the microsystem stack with the protective polymer film; (b) insert the encapsulated microsystem stack into a tube

4.3 Selection of Film Material

The film material should fulfill the following requirements. First, the film should be thermally stable up to at least 125ºC. Second, it should be inert to multiple chemicals, at least including brine and hydrocarbons in downhole environments. Resistance to acidic environments is also of interest, considering that the uncured cement slurry used in the downhole drilling process has low pH. The wider range of chemicals the film can resist, the more applications the film encapsulation approach can be applied to. Third, the material should be transparent to allow optical communication. Fourth, the film should be heat sealable to form a fusion seal that can prevent leakage.

Commercially available plastic film materials that can withstand elevated temperatures are listed in Table 4.1: polycarbonate (PC), polyethersulfone (PES), polyamide 6 (Nylon 6), polyamide 66 (Nylon 66), polytetrafluoroethylene (PTFE), and fluorinated ethylene propylene (FEP). Among all these film materials, FEP has the best chemical resistance to virtually all chemicals and can also be heat sealed; therefore, it is the top selection in this chapter. Although PTFE also has similar chemical compatibility, it is not transparent and cannot be heat sealed, and therefore is not applicable in this process.

The molecular structure of FEP is very similar to PTFE (Figure 4.3). Both of the plastics have abundant carbon-fluorine bonds (C-F), which are very inert to almost all chemicals. These contribute to the superior chemical resistance of these plastics [Car00].

The Nylon 6 and Nylon 66 are compatible with brine and oils conditions but not with acids. This is because the peptide bonds (-CO-NH-) in their molecular structures are inert to brine and oils, but can be hydrolyzed by acids [Her00]. These films can be used in general downhole environment. Since Nylon 66 can serve at a higher temperature than Nylon 6, it is also considered in chapter.

Since the maximum service temperature of PC is relatively low and the PES has an amber color, these two materials are not considered in this dissertation, but can be potentially used in other applications with the same film encapsulation approach evaluated in this chapter.

Table 4.1: Comparison of Commercially Available High Temperature Film Materials ([Web-Pla], [Web-Pol], [Web-Che])

Material	Color	Max. Temp. (^oC)	Heat sealable?	Chemical resistance					
				Brine	Acids	Alkalis	Aromatic hydrocarbons	Halogenated hydrocarbons	Grease and oils
PC	Transparent	130	Yes	Good	Good	Good-poor	Poor	Good-poor	Good-fair
PES	Clear amber	180	Yes	Good	Good-poor	Good	Good	Good	Good-fair
Nylon 6	Transparent - translucent	177	Yes	Good	Poor	Good-fair	Good	Good-poor	Good
Nylon 66	Transparent - translucent	230	Yes	Good	Poor	Good-fair	Good	Good-poor	Good
PTFE	White	260	No	Good	Good	Good	Good	Good	Good
FEP	Transparent	205	Yes	Good	Good	Good	Good	Good	Good
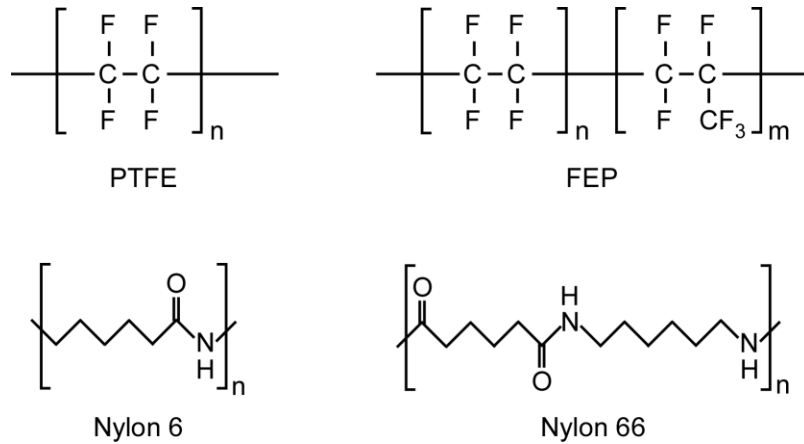
Figure 4.3: Molecular structures of PTFE, FEP, Nylon 6, and Nylon 66.

4.4. Film Encapsulation Process

4.4.1. Process Flow

The film encapsulation process is shown in Figure 4.4. In this process, a microsystem stack encapsulated in soft polymer is shown as an example. The soft polymer encapsulation is intended to cover sharp corners in the system stack to avoid film piercing, as well as to allow pressure transfer in a more uniform way. Alternatively, soft can be applied only at sharp corners. Step 1 is to form an open pouch by heat sealing three sides. An inlet structure is also made in this step by making a heat seal line close to one side and only half way toward the bottom. Later the inlet structure will be used to vacuum the pouch. In Step 2, the microsystem stack to be encapsulated is placed inside the pouch, and a needle connected to a vacuum pump is inserted into the inlet. Then the top side is heat sealed except the needle part. In Step 3, trapped air in the pouch is pumped out, and the inlet of the pouch is heat sealed while retracting the vacuum needle. Additional heat seal lines can be made close to the system stack, to reduce the pouch size. Finally in Step 4, the pouch is trimmed to remove extra film.
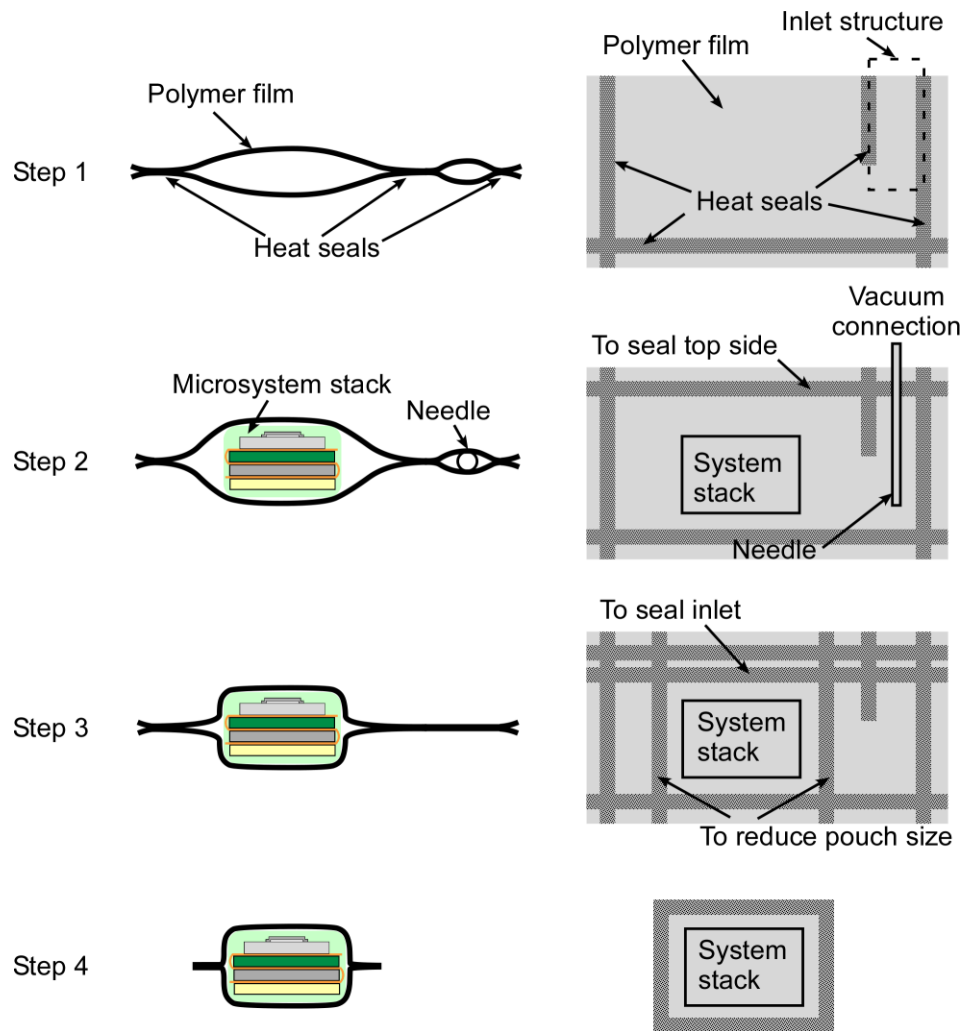
Figure 4.4: Process flow for film encapsulation. Step 1: form an open pouch with an inlet structure. Step 2: place microsystem stack and needle in the pouch, then seal the top side. Step 3: vacuum to pump out trapped air, then seal the inlet. Step 4: trim the sealed pouch.

The vacuum system used in this process is customized in house. A schematic of this vacuum system is shown in Figure 4.5.
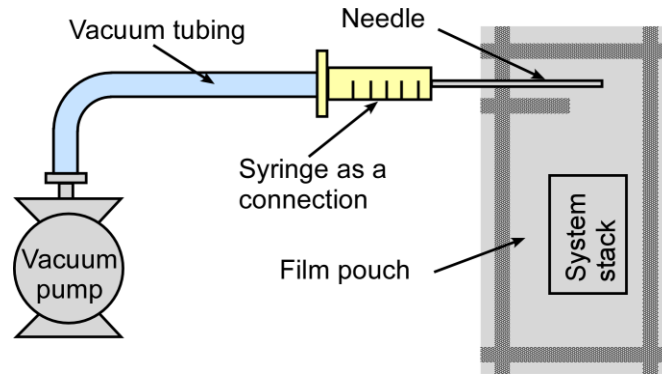
Figure 4.5: A customized vacuum system for the film encapsulation process.

As stated in Section 4.2, this film encapsulation approach can be used in different ways to protect microsystems. For applications where abrasion and impact are less concerns, the microsystem encapsulated in the film can be deployed without further protection (Figure 4.6a). If abrasion and impact are expected to occur, the encapsulated microsystem stack can be inserted or fixed inside a stainless steel or ceramic tube for further protection (Figure 4.6b).

(a)   (b)
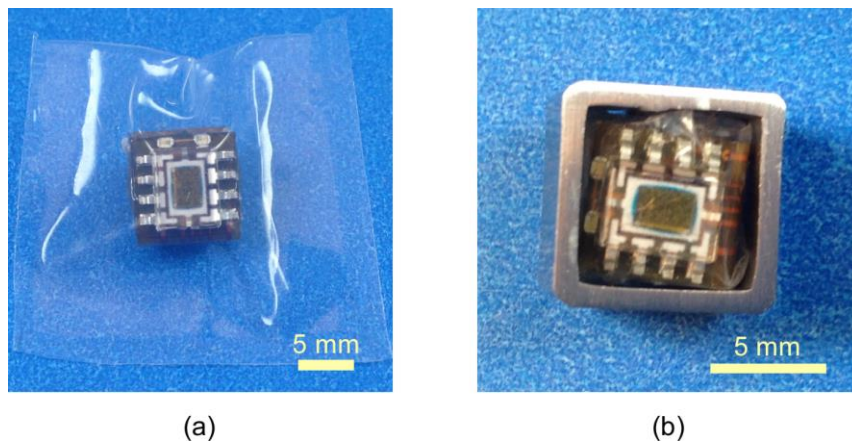
Figure 4.6: Three different ways to protect microsystems with the film encapsulation approach: (a) film encapsulation as a standalone package for microsystem stack; (b) film encapsulated microsystem stack inserted in tube.

4.4.2. Heat Sealing Parameters for FEP and Nylon Films

The heat sealer Model PW7016HT (PackworldUSA, PA) was used in sealing the FEP and Nylon 66 films. The sealer had two 4 mm wide seal bands equipped on both sides of the jaw, providing heat from both sides of the films. In the heat sealer operation, the jaws first clamped the films and provided a constant force of 200 N on the films. After the seal bands reached the pre-specified sealing temperature and stayed at this temperature for a pre-specified sealing time, the bands started to cool down. The jaws retained the clamping force until a pre-specified cooling temperature was reached.

The heat sealing parameters used in this dissertation are summarized in Table 4.2.

Table 4.2: Parameters in heat sealing process for films

Film	Sealing temperature (°C)	Sealing time (s)	Cooling temperature (°C)
Nylon 66, 2 mil	230	4	100
FEP, 3 mil	285	4	200
FEP, 5 mil	295	10	200
FEP, 10 mil	330	10	200
FEP, 20 mil	380	20	200

4.5. Experiment Results

Pouches made from Nylon 66 and FEP films were tested in either boiling API brine or mineral oil at 125°C to check the chemical compatibility with brine and hydrocarbons and the sealing performance to prevent leakage. To address the vapor permeation issue, two post-test processes were investigated. In addition, the pouches were filled with silicone oil, to evaluate the possibility of using silicone oil as a liquid phase vapor barrier.

4.5.1. Brine and Hydrocarbon Tests for Sealed Pouches

Five pouches were prepared for the brine test (Figure 4.7a). Each pouch contained a small metal ball to prevent floating and a moisture strip to indicate brine leakage. The moisture strip was the cobalt chloride test paper from Flinn Scientific, Inc, IL, which was in blue at low moisture level and changed to pink at high moisture level. The size of the moisture strip was approximately 6 mm×18 mm. The films used for these pouches include Nylon 66 films with 2 mil thickness, and FEP films with four different thicknesses: 3 mil, 5 mil, 10 mil, and 20 mil.

These pouches were tested in boiling API brine ($\approx$100.9°C) for 3 h. After the test, none of the five pouches showed any visible degradation in film material. No gross leakage occurred in any pouch, as indicated by the moisture strips that stayed in blue color during the test. However, water vapor intrusion was evident in all the pouches after the test, and all the moisture strips changed color to pink after cooling down (Figure 4.7b). These results indicated that vapor diffused into the pouch through the films.

As the vendor of the moisture strip does not provide the humidity level above which the strip changes color, calculations were done to estimate the amount of moisture that led to the color change. The worst case scenario when the moisture got saturated in the pouch was used in the calculations. The saturation pressure of water vapor at room temperature is 3.13 kPa or equivalently about 3% of the atmospheric pressure [Web-Wat]. This means when the moisture volume exceeds 3% of the pouch volume, the moisture strip will change color for sure. The pouch volume is about 1 mL, and therefore 0.03 mL moisture is enough to change the color of the moisture strip.

Figure 4.7: Sealed pouches for 3 h brine test at boiling temperature: (a) before test; (b) after test. No degradation in Nylon and FEP after the test. No gross leakage, but water vapor permeated through all films, changing the color of the moisture strips from blue to pink.

Another five pouches were prepared for the mineral oil test (Figure 4.8a). These pouches were similar to the ones for brine test; the only exception was that oil strips were encapsulated instead of the moisture strips. The oil strips were cut into approximately 6 mm×18 mm pieces from Clean & Clear® Oil Absorbing Sheets (Johnson & Johnson Consumer Products Company, NJ). These oil strips were in light blue without any oil, changed to deep blue with a small amount of oil, and to transparent with a large amount of oil.

These pouches were tested in mineral oil at 125°C for 3 h. After the test, the FEP film did not show any visible degradation, while the Nylon pouch was discolored. No gross leakage occurred in any pouch. However, all the oil strips changed to deep blue color after the tests, indicating a small amount of oil moisture permeated through the films (Figure 4.7).

Before mineral oil test:

(a) Nylon 2 mil | FEP 3 mil | FEP 5 mil | FEP 10 mil | FEP 20 mil

After 3 h test in mineral oil at 125°C:

(b) Nylon 2 mil | FEP 3 mil | FEP 5 mil | FEP 10 mil | FEP 20 mil
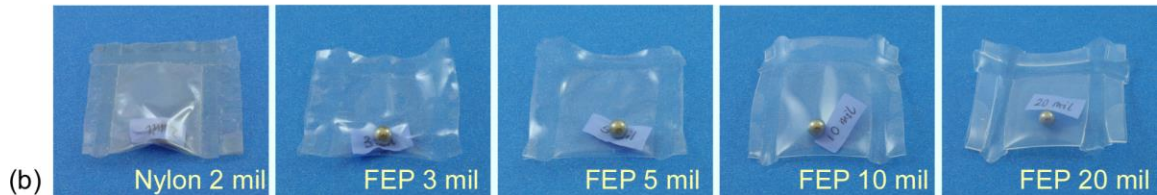
Figure 4.8: Sealed pouches for 3 h mineral oil test at 125°C: (a) before test; (b) after test. No degradation in FEP after the test, but Nylon discolored. No gross leakage, but mineral oil vapor permeated through all films, changing the color of the oil strips from light blue to deep blue.

Calculations show that a non-negligible amount of water and organic vapor can diffuse into the pouch through the film. The mass of the vapor diffuses through the film is given by:

$$m_{vapor} = P_{vapor} \cdot A \cdot t \qquad (4.1)$$

where m_{vapor} is the mass of the vapor through the film, P_{vapor} is the permeability of vapor in the unit of g/m^2×day, A is the area of the film, and t is the time. In the test, the pouch can be estimated as 20 mm by 20 mm so that the area is 800 mm^2 considering two sides. The test time was 3 h. The equivalent vapor volume under atmospheric pressure and room temperature can be calculated by:

88

$$V_{vapor} = \frac{m_{vapor}}{M_{vapor}} \cdot 22.4 \text{ L/mol} \qquad (4.2)$$

where m_{vapor} is the mass of vapor and M_{vapor} is the Molar weight of vapor. The permeability

values are available for water vapor through 1 mil, 3 mil, 5 mil, and 10 mil thick FEP films

at 25°C, as well as for hexane (a type of hydrocarbon) vapor through 1 mil thick FEP films

at 25°C, as listed in Table 4.3 [Web-Dup2].

Table 4.3: Calculation results of vapor permeation through FEP films at 25°C.

Vapor	FEP film thickness (mil) [Web-Dup2]	P_{vapor} (g/(m²×day))	M_{vapor} (mg)	V_{vapor} (mL)
Water	1	7.0	0.70	0.87
	3	2.33	0.23	0.29
	5	1.24	0.12	0.15
	10	0.62	0.06	0.08
Hexane (a hydrocarbon)	1	8.7	0.87	0.23

The calculated mass and volume of vapor permeation at 25°C are also listed in

Table 4.3. The results show that for 1 mil thick FEP films, 0.87 mL water vapor and 0.23

mL hexane vapor can permeate the pouches after 3 h at room temperature. Thicker films

can reduce the permeated vapor amount; however, even for 10 mil thick FEP film, there is

still 0.08 mL water vapor that can permeate the films. This amount of water vapor is

sufficient to change the color of moisture strips as described at the beginning of this section.

In the actual test situations where the temperature is 100°C or 125°C, the permeability will

be higher than the values at 25°C, and therefore the actual vapor amount will be higher

than the calculated results here. Even the 0.08 mL moisture amount is not negligible,

considering the volume of the ELM 2.0 stack is only about 0.26 mL. Simply increasing the thickness of film cannot fully address the vapor permeation issue.

4.5.2. Brine Tests for Sealed Pouches with Post-Test Processes

Two post-test processes were investigated separately: dry baking and vacuum baking.

Five pouches were prepared for the brine test followed by dry baking (Figure 4.9a). These pouches were made of the same five types of films (Nylon 2 mil, FEP 3 mil, 5 mil, 10 mil, and 20 mil), containing moisture strips and metal balls, same as the pouches for the brine test as described in 4.5.1. After being tested in boiling API brine (≈100.9°C) for 3 h, the pouches were immediately transferred into dry rice preheated at ≈100°C, and kept being baked at 100°C for 0.5 h. After cooling down from the dry baking, the moisture strips in Nylon 2 mil and FEP 3 mil pouches changed color to pink partially, while the moisture strips in FEP 5 mi, 10 mil, and 20 mil pouches did not change color. In all these pouches, there was still water permeated inside after baking, but water droplets condensed away from the moisture strip location. These results suggested that controlling the moisture condensation may be a way to keep liquid away from the microsystem stacks encapsulated inside films.

Figure 4.9: Sealed pouches for 3 h boiling brine test followed by dry baking: (a) before test; (b) after test and dry baking. Water vapor permeated into the pouches, and the baking process did not evaporate all the vapor. In the cases of FEP 5 mil, 10 mil, and 20 mil, vapor condensed away from the moisture strip area, and therefore the moisture strip did not change color.

Another five pouches were prepared for the brine test followed by vacuum baking (Figure 4.10a). These pouches were made in the exactly same way as the ones in the last test. After being tested in boiling API brine (≈100.9°C) for 3 h, the pouches were immediately transferred into dry rice preheated at ≈100°C, and then placed inside a vacuum oven at 100°C. Vacuum level of about 1.7 Torr had been applied to the pouches for 0.5 h, during which the oven temperature was kept at 100°C. After cooling down from the vacuum baking, none of the moisture strips in the pouches changed color, indicating all the water vapor was driven out (Figure 4.10b). These results suggested that post-test vacuum baking may be used to remove vapor from the FEP film encapsulation.
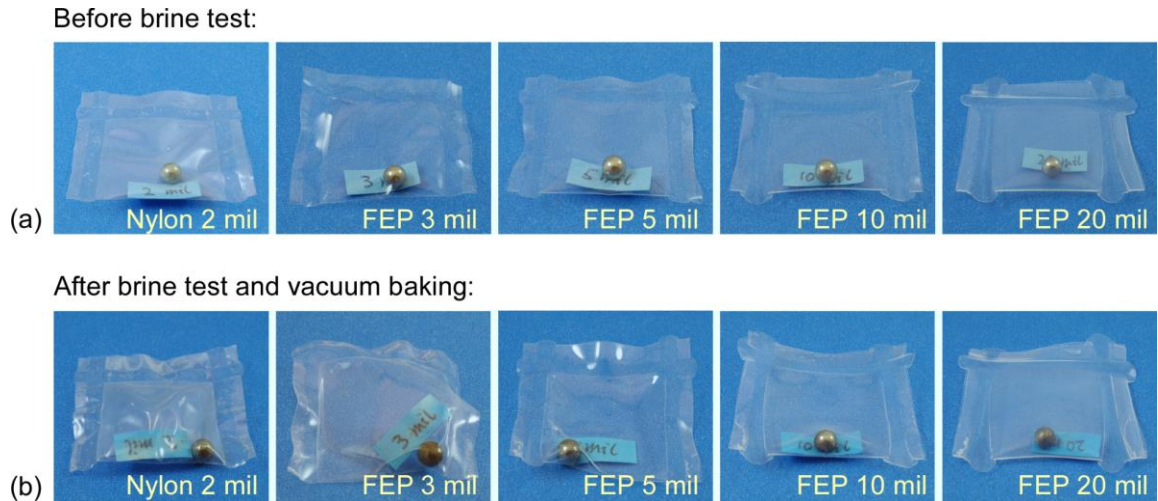
Figure 4.10: Sealed pouches for 3 h boiling brine test followed by vacuum baking: (a) before test; (b) after test and vacuum baking. Moisture strips in all the pouches stayed in blue color, indicating all water vapor was driven out of the pouches.

4.5.3. Brine Test for Sealed Pouches with Silicone Oil

Additional layer between the FEP film and microsystem stack may help to prevent vapor diffusion. Silicone oil was investigated as a liquid phase vapor barrier, as it is inert to the ELM system stacks.

Four pouches were prepared with silicone oil for the brine test (Figure 4.11a). In these pouches, two were made of 3 mil thick FEP films, containing 0.6 mL and 1.8 mL silicone oil in each pouch. The other two were made of 5 mil thick FEP films, also containing 0.6 mL and 1.8 mL silicone oil, respectively. Moisture strips were encapsulated in all the pouches to indicate brine leakage.

These pouches were tested in boiling API brine ($\approx$100.9°C) for 3 h. After the test, the moisture strips in all the four pouches changed color to pink, indicating that moisture penetrated through the films still reached the moisture strips. The silicone oil became foggy after the test. No obvious difference was observed between different film

thicknesses or encapsulated silicone oil amounts. These results indicated that silicone oil may not be sufficiently effective as a moisture barrier layer.

Figure 4.11: Sealed pouches with silicone oil for 3 h boiling brine test: (a) before test; (b) after test. Water vapor permeated into all the pouches, and changed the color of moisture strips into pink.

4.6. Summary

The polymer film encapsulation approach was investigated. Two ways of incorporating the film encapsulation into the system packaging were shown: film encapsulation as a standalone system package and film encapsulation inside a tube. While both FEP films and Nylon 66 films were compatible with API brine, the FEP films were demonstrated to be better than Nylon 66 films in compatibility with hydrocarbons. The test results of FEP and Nylon pouches in boiling API brine and mineral oil at 125°C for 3 h showed that water and mineral oil vapor penetrated the films with thicknesses ranging from 2 mil to 20 mil. Post-test dry baking at 100°C for 0.5 h partially removed the moisture vapor in pouches and resulted in vapor condensation away from pouch center. Post-test

vacuum baking at 100°C for 0.5 h completely removed the moisture vapor in pouches. These two post-test processes may be useful to reduce negative effects from brine on encapsulated microsystem stacks. Additionally, brine test results for FEP pouches with silicone oil inside showed that silicone oil was not sufficiently effective as a moisture barrier layer.

CHAPTER 5:

A ROOM TEMPERATURE BATCH MODE PACKAGING PROCESS OF SUB-MILLIMETER PACKAGES BASED ON MICRO-CRIMPING

In Chapter 2 a sub-millimeter package has been successfully developed for the downhole harsh environments. It consists of a metal shell and a glass lid, which need to be assembled individually and bonded at >160°C by Au-In bond. In order to further reduce process temperature to avoid degradation of battery and polymeric sensors, in this chapter a room-temperature assembly method called micro-crimping is pursued. To increase packaging throughput and meet the need of mass manufacturing, a batch mode packaging process based on the micro-crimping is pursued.

This chapter presents a low temperature batch mode packaging process for microsystems that are intended for harsh environments, in particular those with high pressure and high salinity such as encountered in downhole data logging for oil exploration and production. The package consists of a shell made from a high strength material such as stainless steel, and an insert made from a deformable material like aluminum. The process includes a batch mode method for chip integration and a batch mode micro-crimping method for package assembly. In a process demonstration, a 5×5 array of packages was made from stainless steel 316 and aluminum alloy 3003, with dummy silicon chips encapsulated inside. Each package had an outer dimension of 0.5 mm along each axis. Two layers of coatings were deposited on the packages, including 50-nm thick Al_2O_3

deposited by atomic layer deposition and 5 μm thick Parylene-C™ made by vapor phase deposition to protect against corrosion. The packages survive at least 72 hours in the standard American Petroleum Institute hot brine at 80°C. The packages also survive pressure >200 MPa.

5.1. Package Design and Modeling
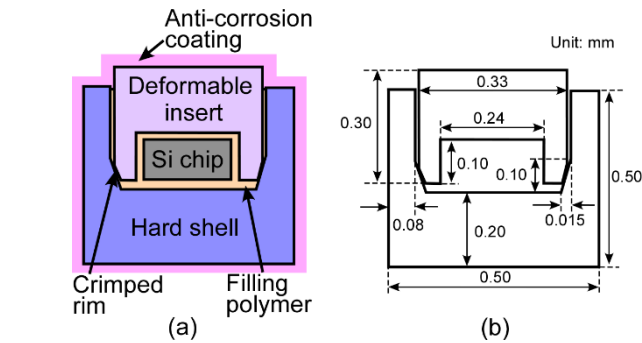
Figure 5.1: Cross-sectional view of the micropackage: (a) package design; (b) selected dimensions.

Each package consists of a hard metal shell and a deformable insert (Figure 5.1a). The hard metal shell provides the major structural strength of the assembly. The inner sidewall surfaces of the hard metal shell are tapered near the bottom of the cavity. A deformable insert is plugged into this cavity to seal the opening. The rim of the deformable insert is pressed against the tapered surfaces of the hard metal shell, and slightly crimped during sealing. Silicon chips, and any other components to be packaged, are housed in a cavity within the deformable insert. The hard shell is made from cold-rolled stainless steel 316 (SS), which provides excellent structural strength while allowing RF transparency as discussed in Section 5.4. The deformable insert is made from aluminum alloy 3003 (Al). Other materials may also be used as appropriate. The narrow gaps between the deformable insert and the hard shell are filled with a sealing polymer such as silicone. After assembly

96

and singulation, two anti-corrosion coating layers, Al_2O_3 and Parylene-C^{TM}, are coated on the exterior surface of the entire package, to further protect the package from the target corrosive environment. The deformable insert is expected to stay reliably inside the hard shell after the deformation during assembly; any exterior pressure in the target environment will push the deformable insert against the hard shell and result in a tighter seal.

Finite element analysis modeling was used to help the dimensional design of the package. Using COMSOL$^{®}$ Multiphysics 4.3, the structural integrity of the package was simulated under the target pressure (50 MPa). The dimensions were selected to provide a large safety margin for the structures under the target pressure. For a package with exterior dimensions of 500×500×500 μm^3, the selected dimensions for the shell were: 200 μm bottom wall thickness and 80 μm sidewall thickness (Figure 5.1b). The tapered region at the bottom of inner sidewall surfaces was 100 μm in height and 15 μm in width. For the inserts, the selected dimensions were: 330×330×300 μm^3 (L×W×H) exterior size, 200 μm bottom wall thickness, 45 μm sidewall thickness, and 240×240×100 μm^3 for the cavity for Si chips. The modeled maximum stress and the safety factor of each of the package components with a 50-MPa hydrostatic load pressure applied are listed in Table 5.1. The safety factors, defined as the yield strength of the material divided by the maximum stress, were >3.1 and >2.4 for the SS shell and the deformable insert, respectively. These dimensions were used in the demonstration of the batch packaging process, and can be optimized in future efforts as needed.

Table 5.1: Simulation results for an assembled package with selected dimensions under 50 MPa exterior pressure.

	Max. Stress (MPa)	Yield Strength (MPa)	Safety Factor
SS 316 (cold-rolled) Hard Shell	350	>1100 [Web-All]	>3.1
Al 3003 Deformable Insert	50*	>120 [Web-Alu]	>2.4

Max stress outside the regions that have plastic deformation designed for micro-crimping packaging.

5.2. Process Description and Characterization
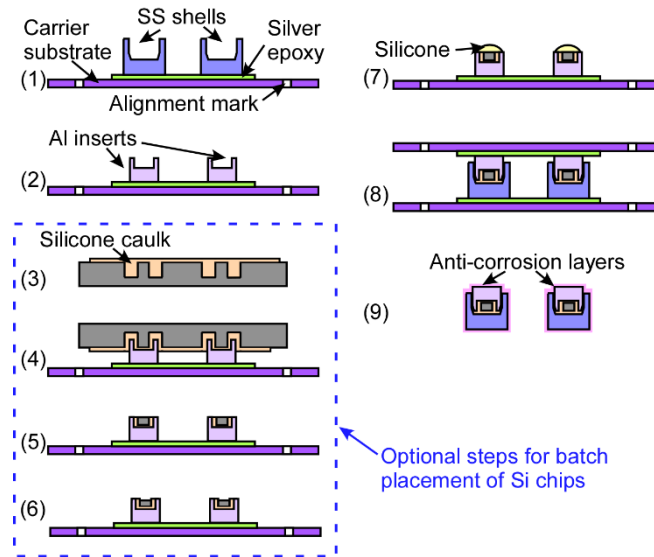
Figure 5.2: Low temperature batch packaging process flow: (1) EDM array of SS shells; (2) EDM array of Al inserts; (3) Partially diced Si wafer with device regions and apply silicone coating; (4) Bond Al insert and Si wafer; (5) Lap away Si wafer; (6) Isotropic Si plasma etch (optional); (7) Apply additional silicone; (8) Align and assemble Al inserts into SS shells (micro-crimping process); (9) Release assembled packages and coat anti-corrosion layer.

The process flow is shown in Figure 5.2. Steps (1) and (2) are used to fabricate the arrays of SS shells and Al inserts, respectively. This is done by attaching a metal substrate to a conductive carrier using electrically conductive epoxy, and then performing batch mode (or serial mode for rapid prototyping) μEDM for the desired patterns. Alignment

marks are machined on the carrier substrate using µEDM in this step for assembly of the SS shells and Al inserts. Fabricated shells and inserts arrays are shown in Figure 5.3.

(a)   (b)
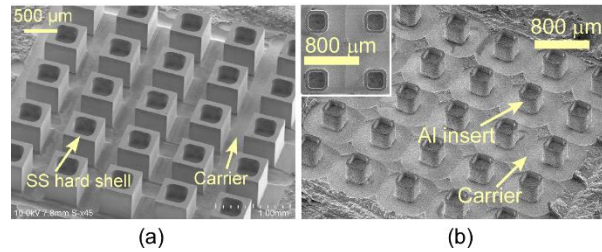
Figure 5.3: SEM images of the 5×5 arrays of: (a) SS shells (outer dimensions: 500×500×500 µm^3; inner dimensions: 340×340×300 µm^3); (b) Al inserts (outer dimensions: 330×330×300 µm^3; inner dimensions: 240×240×100 µm^3).

Steps (3)-(6) are used to place silicon chips inside the cavities of deformable inserts array. This is a batch insertion method. The silicon wafer is partially diced through the wafer thickness (Step 3). A layer of silicone is applied on the top surface of the partially diced wafer. This wafer is then aligned and assembled with the array of deformable inserts so that the silicon chips are placed inside the cavities of the inserts (Step 4). The alignment marks on the array carrier and the wafer are used during this step. The excess thickness of the silicon wafer is lapped away (Step 5), completing the batch insertion method (Figure 5.4a). An optional plasma etch can be used to further recess the Si below the surface of the metal, enhancing the mechanical isolation of the silicon when assembly is completed (Step 6). Alternatively, a pick-and-place method can be used (Figure 5.4b). The silicon chips are placed into the cavities that are coated with silicone. High volume production can be carried out using commercial pick-and-place machines. The accuracy and speed of pick-and-place machines are adequate for this process.
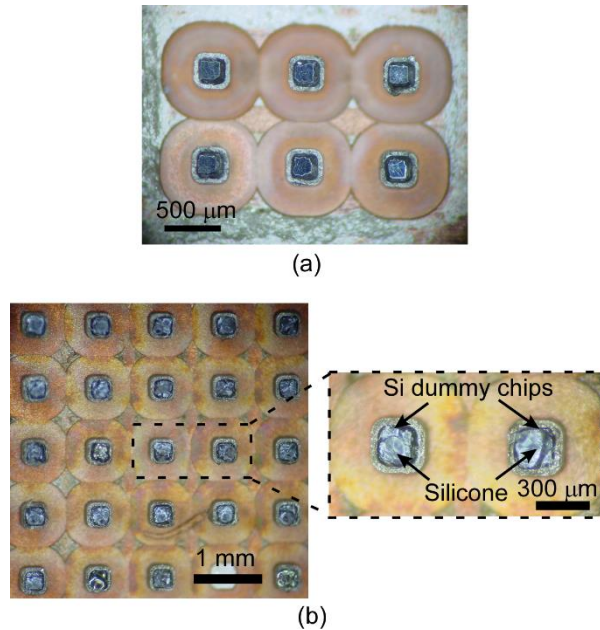
Figure 5.4: Dummy Si chips placed in cavities in the deformable inserts: (a) by the batch placement method (photo taken after lapping from the backside of the Si wafer); (b) by the pick-and-place method.

After placing silicon chips, silicone is applied on the top of the silicon chips in the cavities of the deformable inserts (Step 7). The array of deformable inserts is then aligned with and inserted into the array of hard shells (Step 8). This can be performed using a simple approach illustrated in Figure 5.5. Controlled pressure is uniformly applied for insertion to get desired amount of deformation on the inserts. Maximum nominal pressure applied on the deformable inserts is typically 150 MPa. This allows the sidewalls of the inserts to deform for a better seal without damaging the Si chips embedded inside. This assembly step executes the batch mode micro-crimping process. The alignment marks on the carriers for the two arrays are again used in alignment. The assembled arrays are immersed in acetone to dissolve the conductive epoxy and release the assembled packages. Finally the individual packages are coated with Al_2O_3 deposited by atomic layer deposition (ALD) and then Parylene-C^{TM} formed by vapor phase deposition as anti-corrosion coatings

100

(Step 9). The usage of a bi-layer of ALD Al_2O_3 and Parylene-C^{TM} coating to protect samples from corrosive environments has been reported in previous studies [Ma14, Xie12, Xie13].
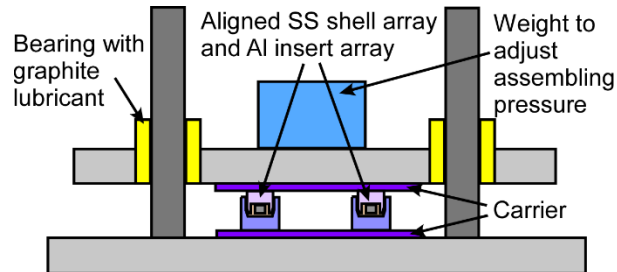
Figure 5.5: Custom-built fixture to apply controlled and uniform assembly pressure to crimp the Al inserts.

An SEM image of an assembled package after release from the carriers is shown in Figure 5.6. The assembled packages were reopened, and the silicon chips inside were found to remain intact after the micro-crimping step. To evaluate the effect of the micro-crimping process on the inserts, five packages were disassembled and the 3D geometries of the inserts were measured by a LEXT® laser confocal microscope (Olympus Corporation, PA, USA). The photos of a corner of an insert before and after the micro-crimping process are shown in Figures 5.7(a) and (b). Both structural bending and local plastic deformation were observed on the sidewalls of the inserts as expected. This deformation is also clearly shown in Figures 5.7(c), an SEM image of an insert after the micro-crimping process. A typical angle of about 5°-17° was formed at the top portion of exterior sidewalls of the Al inserts. This generally agrees with the 8.5° designed taper of the inner sidewalls of SS shells. The yield in the initial two trials was 48% (12/25) and 83% (5/6). The losses were mainly due to the failure of adhesives used for attachment of the package components to the carriers during manual handling in this proof of concept.
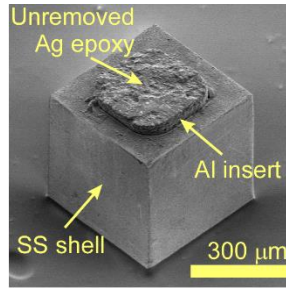
Figure 5.6: A released package assembled by the batch mode micro-crimping method.
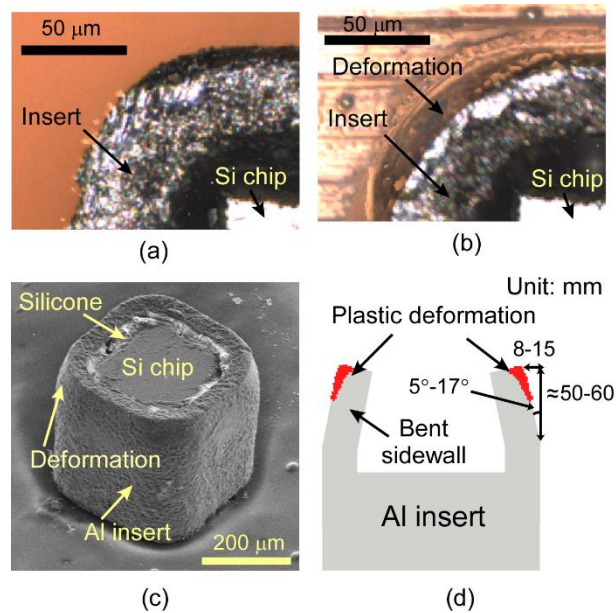
Figure 5.7: Validation of micro-crimping. Images of: (a) a corner of an insert with a Si chip before micro-crimping; (b) the same insert with the Si chip after micro-crimping and disassembly. (c) SEM image of a typical insert with Si chip after micro-crimping and disassembly. (d) Typical measured values of structural bending and plastic deformation after the micro-crimping process.

To effectively monitor any leakage through the anti-corrosion coatings, a corrosion indicator layer was deposited by sputtering before the transparent anti-corrosion coatings were deposited. A Cr/Cu coating of 20/200 nm was deposited by sputtering for this purpose. To provide a seamless coating covering all 6 surfaces of the packages, ALD Al_2O_3 and Parylene-C^{TM} were each deposited in two steps, with reversed package orientation. The Al_2O_3 deposition was performed at 150°C using thermal ALD (Oxford^{TM} Instruments

OpAL), while the Parylene-C^{TM} was deposited by a PDS 2035 Parylene Deposition System (Specialty Coating Systems, Indianapolis, IN). The coating thickness from each deposition session for ALD Al$_2$O$_3$ was 50 nm, and 5 μm for Parylene-C^{TM}. Overall, the expected thickness of ALD Al$_2$O$_3$ is 100 nm on sidewalls and 50 nm on the top and bottom surfaces, and the thickness for Parylene-C^{TM} is 10 μm on sidewalls and 5 μm on top and bottom surfaces.

5.3. Test Results

The batch fabricated packages were tested in hot brine and separately at high pressure. The survival of the packages in both testing conditions suggests the capability to survival in the target harsh environment.

5.3.1. Hot Brine Test

American Petroleum Institute (API) specified brine (8 wt% NaCl and 2 wt% CaCl$_2$ in deionized water) at 80°C was used to test the anti-corrosion capability of the batch fabricated packages [Cha12]. This test was performed at atmospheric pressure. As described in Section 5.2, these packages have a corrosion indicator layer of 200 nm thick copper film underneath the two anti-corrosion coatings. Any leak of corrosive brine through the anti-corrosion coatings will cause the copper film to discolor. A typical color change in the copper film that has been attacked by hot brine leaked through intentionally created defects in the anti-corrosion coatings is shown in Figure 5.8(a). Since the only path for corrosive chemicals to enter the package is through the interface between the SS shell and the Al insert, copper discoloration on the side of the package where the interface is located provides an early warning of package leakage.
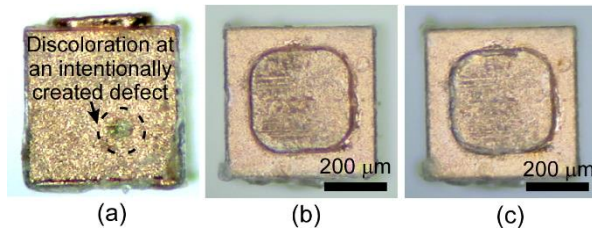
Figure 5.8: (a) Copper as a corrosion indication layer and its color change after being attacked by hot brine. The green area corresponds to a local defect intentionally created in the anti-corrosion layers. Photos of the top surface of a package: (b) before hot API brine test; (c) after 72 h in 80°C API brine. No color change observed in the copper film, indicating no leakage through the anti-corrosion layers.

During the hot brine test, the copper layers on the top surfaces of the packages were inspected every 2 h during the first 16 h of the test, then every 4 h until the 48 h time point, and every 12 h until the 72 h time point. Figures 5.8(b) and (c) show the photos of a typical package before the hot brine test and after 72 h in the test, respectively. There was no copper discoloration observed on the top surface, indicating the effectiveness of the anti-corrosion coatings and the capability of the package to survive in hot brine for at least 72 h.

5.3.2. High Pressure Test

The first set of pressure tests was performed to check whether the packages could survive the target pressure of 50 MPa. An Enerpac™ hydraulic pump P142 was used to apply pressure. A customized pressure head sealed the oil-filled test chamber, in which the package was housed. The packages were pressurized up to 62 MPa (≈9000 psi) and then retrieved. The packages remained intact without deformation when viewed under a microscope. To check whether deformation or bowing under the high pressure occurred on the sidewalls of one of the packages, surface height profiles along the diagonal axes of both the Al insert top surface and the SS sidewall surface were measured using the LEXT

laser confocal microscope. The results are shown in Figure 5.9, indicating that no deformation occurred on the package sidewalls.
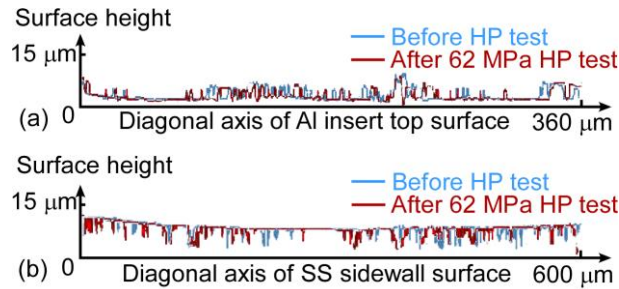
Figure 5.9: Deformation check for high pressure test. Surface height profiles of (a) diagonal axis of Al insert top surface; (b) diagonal axis of SS sidewall surface.

The second set of pressure tests was performed to evaluate the packages at the extreme pressure conditions. This test was performed at Prof. Adam Simon's lab in the Department of Earth and Environmental Sciences at the University of Michigan and with the help of Ms. Laura Bilenker and Mr. Brian Konecke. A customized high pressure test system was used to test the packages. Using a motorized pump, this system can generate up to 200 MPa (≈29,000 psi) pressure in water in a test chamber. The pressure was calibrated against a high precision pressure gauge (factory calibrated Heise model C-53275, Stratford, CT, USA). With this system, the packages were pressurized at 50, 70, 90, 120, 150 and 200 MPa successively, for a 5-min. duration at each pressure. The packages were retrieved after each pressure step for visual check under microscope. No deformation on the packages was observed. Top view photos of one of the package after each pressure test steps are shown in Figure 5.10.
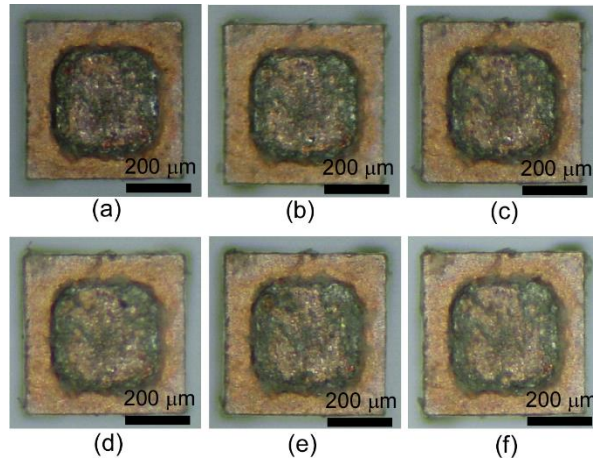
Figure 5.10: Top view photos of a package during high pressure test: (a) after 50 MPa; (b) after 70 MPa; (c) after 90 MPa; (d) after 120 MPa; (e) after 150 MPa; (f) after 200 MPa.

During these pressure tests, the Al inserts further deformed and went into the SS shell cavity by additional 5 to 10 µm. After disassembling these packages, the Si chips were visually inspected. No damage on the silicon chips was observed as shown in Figure 5.11, confirming the robustness of the packages under the extreme pressure condition.
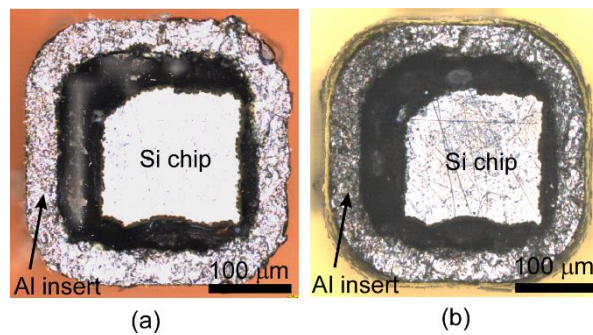
Figure 5.11: Photos of (a) an Al insert before micro-crimping, with a Si chip integrated by the batch mode method; (b) the same Al insert with the Si chip disassembled from the package after a 200 MPa high pressure test. No damage on the Si chip was observed.

5.4. Discussion

There are five advantages of this packaging process. First, the process is compatible with many different types of packaging materials, as long as one of the two selected materials is hard and the other is deformable. This would allow selection of

packaging materials according to the requirements of the application environments. For different materials, the approaches to fabricate arrays of hard shells and soft inserts (step 1-2 in Figure 5.2) will be different, while the same approaches for batch mode chip insertion and assembly process may still apply. For example, another possible combination is a ceramic hard shell and a metal deformable insert. Ceramics are attractive as packaging materials, providing high hardness, chemical resistivity, and thermal and electrical insulation. Batch mode micro ultrasonic machining (μUSM) can be used to fabricate an array of ceramic shells. This process uses a lithographically defined tool to remove material from a ceramic substrate through ultrasonic vibrations [Li06, Li10].

Second, there is no high temperature step during the packaging process. The only step that goes above the room temperature is the ALD coating step, which can be performed at a low temperature of 80°C if necessary. It may also be skipped if significant corrosion is not a concern for the packages. Moreover, the fabrication of package components (hard shells and deformable inserts) is separate from the rest of the packaging process. High temperature processes, if needed for alternative packaging materials, may be used to fabricate hard shells and deformable inserts without affecting the chips to be encapsulated.

Third, the package design for this process is inherently immune to high pressure. Higher exterior pressure will press the deformable insert harder to form a better seal.

Fourth, unlike the traditional bonding methods where accurate alignment is necessary with an error less than 20% of the width of the bonding rim [Web-Far], only rough alignment is needed in this process for the deformable inserts to enter the cavities of the hard shells. The rest of the insertion and assembly are self-aligned.

Fifth, although the whole package in this work is made from metal, RF signals can still pass through the package sidewall if the sidewall thickness is less than the skin depth of the metal. This can be used for communications as needed in future implementation. The skin depth (δ) in an electrically conductive material is determined by the frequency of the electromagnetic wave (f) and the material properties including electrical resistivity (ρ) and magnetic permittivity (μ) [Kar98]:

$$\delta = \sqrt{\frac{\rho}{\pi f \mu}} \tag{5.1}$$

For a 2 MHz RF signal, the skin depth in SS 316 is ≈300 µm. In this work, the bottom wall thickness of the hard shell is 200 µm; therefore a 2 MHz RF signal is expected to pass through the package and can be used for communications as needed in future implementations.

In this work, the feasibility of the batch mode packaging process was successfully demonstrated. The package design for the proof of concept used a large safety margin, which could be further optimized if necessary. The arrays of SS shells and Al inserts were fabricated by serial mode µEDM for fast prototyping. Batch mode µEDM may be used to increase the throughput for large volume fabrication [Tak02, Li13].

In order to be able to reopen the assembled package to characterize the micro-crimping process, gaps between the SS shell and Al inserts were designed to be 5 µm wide. This could be further reduced in future implementations. The gaps are the only route by which moisture or corrosive chemicals may enter the package. In this demonstration,

silicone was used to fill the gap. Silicone is liquid-tight but not air-tight. Other polymers with proper moisture barrier capability could replace silicone if necessary.

5.5. Summary

The feasibility of the low temperature batch mode packaging process has been successfully verified. In the process demonstration, a 5×5 array of packages made from SS and Al has been successfully assembled using the batch mode micro-crimping method with intentional deformation. The exterior size of each package was 0.5 mm. For chip integration, both the batch mode method and the pick-and-place method have been demonstrated using dummy Si chips. With anti-corrosion coatings of 50 nm ALD Al_2O_3 and 5 μm Parylene-C^{TM}, the packages survived at least 72 hours in the standard API brine at 80°C. The packages separately survived a pressure of >200 MPa without any crack in the encapsulated Si chip. With the capability of utilizing robust packaging materials and the inherent immunity to high pressure, this low temperature batch mode packaging process can be potentially expanded to a wafer scale and supplement the current WLP technologies, particularly for packaging microsystems that are intended for harsh environment applications.

CHAPTER 6:

CONCLUSIONS AND FUTURE WORK

This chapter summarizes the efforts of developing system packages for microsystems in harsh environment applications. Then, major contributions to the microsystems packaging field are listed. Future work regarding a system package design that only transfers pressure to the pressure sensor while isolating all other components from high pressure is proposed.

6.1. Conclusions and Major Contributions

This dissertation advances packaging technologies to enable the use of microsystems in harsh environment applications such as downhole sensing that involve high temperature, high pressure, and multiple type of chemicals.

Sapphire-on-SS packages capable of isolating high pressure and allowing optical communication were successfully demonstrated with two different sizes (0.8 mm and 8 mm). For the 0.8 mm packages, the outer dimensions were $0.8\times0.8\times0.8$ mm^3, whereas the interior cavities were $0.4\times0.4\times0.45$ mm^3. The packages consisted of SS 17-4 PH metal shells and borosilicate glass lids which were sealed by an Au-In bond, and were coated with alumina and Parylene-C^{TM}. The measured bond strength was ≈13 MPa. The packages survived high temperature tests at 125°C, high pressure tests at 50 MPa, and corrosion tests in API standard brine at 80°C. For the 8 mm packages, the outer dimensions were $8.8\times8.8\times6.85$ mm^3, whereas the interior cavities were $6.8\times6.8\times4.6$ mm^3. The packages

consisted of SS 17-4 PH metal shells and sapphire lids which were sealed by a high temperature epoxy, and were coated by an all-around Parylene-C^{TM} layer. The packages with embedded electronics survived >60 min in API brine at 125ºC and 50 MPa, and also survived extended conditions of 70 MPa pressure, in Isopar-L, and in cement slurry. The embedded microsystems successfully performed the temperature logging and optical communication functions during the tests.

Polymer-in-tube packages with pressure transfer capability were designed for the second generation of environmental logging microsystems (ELM2.0). The outer dimensions of the packages were 9.5×9.5×6.5 mm^3, whereas the interior cavities were 7.85×7.85×6.5 mm^3. The packages consisted of hard tubes made of stainless steel 304 or alumina ceramic, and were filled with soft silicone. The packages with ELM2.0 systems survived at 125ºC and 50 MPa in API brine. The packaged ELM2.0 systems successfully performed the temperature/pressure logging and optical communication functions during the tests.

A chemical protection approach for microsystems using polymer film encapsulation was investigated. Two ways of incorporating the film encapsulation into the system packaging were shown: film encapsulation as a standalone system package and film encapsulation inside a tube. Both ways allowed for chemical protection and pressure transfer. The first approach would be used when abrasion and impact were of less concern in target environment, while the second approach did not have this limitation. While both FEP films and Nylon 66 films were compatible with API brine, the FEP films were better than Nylon 66 films in compatibility with hydrocarbons. The test results of FEP and Nylon pouches in boiling API brine and mineral oil at 125°C for 3 h showed that water and

mineral oil vapor penetrated the films with thicknesses ranging from 2 mil to 20 mil. Post-test dry baking at 100°C for 0.5 h partially removed the moisture vapor in pouches and resulted in vapor condensation away from pouch center. Post-test vacuum baking at 100°C for 0.5 h completely removed the moisture vapor in pouches. These two post-test processes may be useful to reduce negative effects from brine on encapsulated microsystem stacks. Additionally, brine test results for FEP pouches with silicone oil inside showed that silicone oil was not sufficiently effective as a moisture barrier layer.

A low temperature batch mode packaging process was developed for microsystems intended for harsh environments, in particular those with high pressure and high salinity such as encountered in downhole data logging for oil exploration and production. The packages consisted of shells made from a high strength material such as stainless steel, and inserts made from a deformable material like aluminum. The process included a batch mode method for chip integration and a batch mode micro-crimping method for package assembly. In a process demonstration, a 5×5 array of packages was made from stainless steel 316 and aluminum alloy 3003, with dummy silicon chips encapsulated inside. Each package had an outer dimension of 0.5 mm along each axis. Two layers of coatings were deposited on the packages, including 50 nm thick Al_2O_3 deposited by atomic layer deposition and 5 μm thick Parylene-C^{TM} made by vapor phase deposition to protect against corrosion. The packages survived at least 72 hours in the standard American Petroleum Institute hot brine at 80°C. The packages also survive pressure >200 MPa.

Major Contributions

1. Demonstrated **sapphire-on-SS** package design capable of **isolating high pressure and allowing optical communication.**

112

a. Successfully protected **millimeter scale** microsystems with temperature sensors against target harsh conditions.

b. Demonstrated package size **scalable to sub-millimeter scale.**

c. Identified **a bi-layer coating consisted of ALD alumina and Parylene-C™** against multiple chemical environments including API brine, hydrocarbons, and cement slurry.

2. Designed a **pressure transfer method through soft polymer** and successfully verified this method on **millimeter scale microsystems with pressure sensors**.

3. Investigated of a **general** approach which has the potential to significantly improve **chemical resistance** of microsystems based on **polymer film encapsulation.**

4. Developed packaging process based on **micro-crimping.**

a. Enabled **room-temperature** assembly process for **sub-millimeter scale** packages made from **metal alloys.**

b. Demonstrated the process can be used in **batch mode** which is suitable for mass production.

6.2. Future Work

As discussed in Chapter 3, there are two different approaches for pressure transfer: transferring pressure to the pressure sensor only, and transferring pressure to then entire microsystems. For the ease of fabrication, the latter approach was selected in Chapter 4. However, this approach requires every component in the microsystem can survive in the target pressure, which limits the device selection and poses a reliability concern for the assembled stack. Also, further miniaturization of the microsystem requires reduction or even elimination of individual packages of each component, and the new forms may no

longer be able to survive the high pressure. In the long run, the former approach will be inevitable. A few designs of this approach are proposed in Figure 6.1. The key change will be the manufacturability.
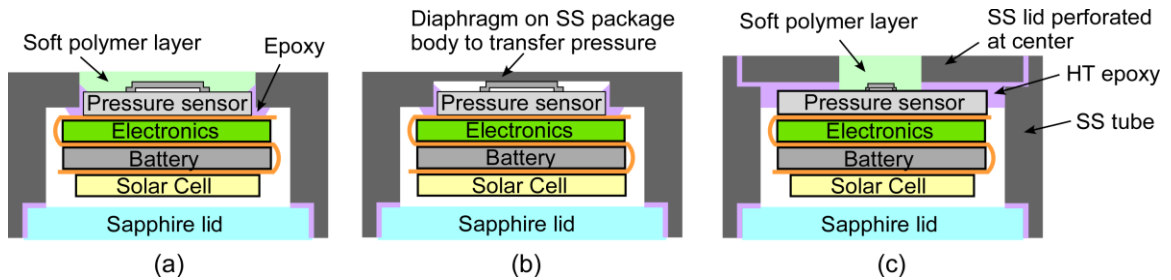
Figure 6.1: Several proposed package designs that only transfer pressure to the pressure sensor.

The packages developed in this dissertation can support three types of sensors: temperature sensors, pressure sensors, and inertial sensors. Temperature sensors and inertial sensors do not require physical interface to the e nvironment, while pressure sensor interface has been developed in Chapter 4. It is foreseeable that some other types of sensors, for example, ion sensors and hydrocarbon sensors, will also be integrated into the microsystems for downhole sensing. Future efforts should also include developing the appropriate physical interfaces in the package design.

APPENDIX

HYPERELASTIC MATERIAL THEORY

Hyperelastic material is a type of ideal elastic material models suitable for large deformation. Unlike the linear stress-strain relationship which is directly defined by Young's modulus in the linear elastic material model, the hyperelastic material model defines non-linear stress-strain relationship in a vague way through elastic strain energy density [Boy00, Mar06]. To help understand this, this appendix first reviews the necessary backgrounds of solid mechanics, then gives the specific forms of two commonly used hyperelastic material models, and finally explains how the stress-strain relationship is derived from these models.

A.1 Basics of Solid Mechanics

A.1.1 Deformation Gradient and Right Cauchy-Green Deformation

Consider a point inside a solid object. Assume that the point, initially locates at the coordinate $\mathbf{X}$, and moves to coordinate $\mathbf{x}$ at the time t due to deformation of this object. Then, the path of this point can be described as [Com13, Dil07]:

$$\mathbf{x} = \mathbf{x}(\mathbf{X}, t) \tag{A.1}$$

The material coordinate refers to $\mathbf{X}$ which is static, and the spatial coordinate refers to $\mathbf{x}$ which is moving. All physical quantities described later in this appendix refer to the

material coordinate, same as the settings in COMSOL®. The current location and initial location can be related by a displacement vector u:

$$\mathbf{x} = \mathbf{X} + \mathbf{u}(\mathbf{X}, t) \tag{A.2}$$

An important quantity, the deformation gradient tensor F, can be acquired by taking the derivative of (A.1):

$$d\mathbf{x} = \frac{\partial \mathbf{x}}{\partial \mathbf{X}} d\mathbf{X} = F d\mathbf{X} \tag{A.3}$$

$$F = F(\mathbf{X}, t) = \frac{\partial \mathbf{x}}{\partial \mathbf{X}} \tag{A.4}$$

This quantity contains complete information about deformation of this particle. It can be decomposed into a pure deformation U and a pure rotation R:

$$F = RU \tag{A.5}$$

The pure rotation R does not contribute to local stress. To extract the pure deformation information, the right Cauchy-Green deformation tensor C is defined as:

$$C = F^T F = U^2 \tag{A.6}$$

Similar to U, C also only considers deformation, but is used much more commonly than U in solid mechanic analysis. The physical meaning of C is the square of local pure deformation. Deformation may cause material density change. The ratio between current volume V and initial volume V_0 is defined as J, which can be proved to be:

$$J = \frac{dV}{dV_0} = \frac{\rho_0}{\rho} = \det(F) \tag{A.6}$$

A general pure deformation F contains an elastic part F_{el} and an inelastic part F_{in}:

$$F = F_{el}F_{in} \tag{A.7}$$

Similar to the linear elastic model, hyperelastic models only take elastic deformation F_{el} into consideration. The elastic right Cauchy-Green deformation tensor C_{el} is computed from F_{el}:

$$C_{el} = F_{el}{}^T F_{el} \tag{A.8}$$

Similarly, the elastic volume change ratio is:

$$J_{el} = \det(F_{el}) \tag{A.8}$$

A.1.2 Invariants of Right Cauchy-Green Deformation Tensor

The three invariants of right Cauchy-Green deformation tensor C are defined as [Com13, Dil07]:

$$I_1 = \lambda_1^2 + \lambda_2^2 + \lambda_3^2 \tag{A.9a}$$

$$I_2 = \lambda_1^2\lambda_2^2 + \lambda_2^2\lambda_3^2 + \lambda_3^2\lambda_1^2 \tag{A.9b}$$

$$I_3 = \lambda_1^2\lambda_2^2\lambda_3^2 \tag{A.9c}$$

where λ_1, λ_2, and λ_3 are the eigenvalues of C_{el}. The physical meanings of λ_1, λ_2, and λ_3 are the stretch ratios in the directions that do not rotate in the deformation, specially termed as principal stretches. An illustration of the principal stretches is in Figure A.1.

Before deformation   After deformation
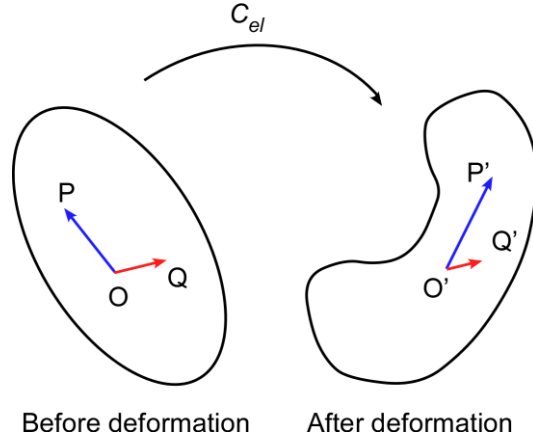
Figure A.1: Illustration of principal stretch. Points O, P, and Q in the continuum body changed to new positions as O', P', and Q' after deformation. Vector OP changes in both direction and magnitude, while vector OQ only changes in magnitude. The stretch ratio of OQ is one of the three principal stretches.

A.2 Hyperelastic Materials Models

The constitutive equation of hyperplastic material models relates elastic strain energy density W_s to the elastic right Cauchy-Green deformation tensor C_{el}. Different hyperelastic models have different constitutive equations. Mooney-Rivlin and Ogden models are commonly used hyperelastic models and correspond well with experimental results for silicone. In Mooney-Rivlin model, the constitutive equation is [Boy00, Mar06, Com13]:

$$W_s = C_{10}(I_1 - 3) + C_{01}(I_2 - 3) + \frac{1}{2}B(J_{el} - 1)^2 \qquad (A.10)$$

where C_{10} and C_{01} are material parameters, B is the initial bulk modulus, J_{el} is the elastic volume ratio, and I_1 and I_2 are the first and second invariants of the elastic right Cauchy-Green deformation tensor C_{el}.

In Ogden model, the constitutive equation is [Boy00, Mar06, Com13]:

$$W_s = \sum_{i=1}^{3} \frac{\mu_i}{\alpha_i}(\lambda_1^{\alpha_i} + \lambda_2^{\alpha_i} + \lambda_3^{\alpha_i} - 3) + \frac{1}{2}B(J_{el} - 1)^2 \tag{A.11}$$

where μ_i and α_i are material parameters, λ_1, λ_2, and λ_3 are the eigenvalues of C_{el}, B is the initial bulk modulus, and J_{el} is the elastic volume ratio.

A.3 Stress-Strain Relationship in Hyperelastic Materials

A strain measures how much the displacement of a given point deviates away from the rigid body displacement. It can be defined with different mathematical formula. Cauchy's strain ε_C, also known as linear strain or Infinitesimal strain, is defined as [Dil07]:

$$\varepsilon_C = \frac{1}{2}((\nabla \mathbf{u})^T + \nabla \mathbf{u}) \tag{A.12}$$

It is used in linear elastic materials or more complicated materials with small deformation. This strain is not suitable for large deformation in non-linear materials, such as hyperelastic materials. In this situation, Green-Lagrange strain tensor ε_{G-L} needs to be used, which is defined as:

$$\varepsilon_{G-L} = \frac{1}{2}(C_{el} - \mathbf{I}) \tag{A.13}$$

where C_{el} is the elastic right Cauchy-Green deformation tensor, and $\mathbf{I}$ is an identity matrix.

A stress describes the internal force in material, and it can also be defined with different mathematical formula. The most commonly used form is Cauchy stress σ. In hyperelastic materials, σ is given by

$$\sigma = \frac{2}{J_{el}} F_{el} \frac{\partial W_s}{\partial C_{el}} F_{el}^{\,T} \tag{A.14}$$

where J_{el} is the elastic volume ratio, F_{el} is the elastic deformation gradient tensor, C_{el} is the elastic right Cauchy-Green deformation tensor, and W_s is the elastic strain energy density of the hyperelastic material. The stress-strain relationship is given by:

$$\sigma = \frac{2}{J_{el}} F_{el} \frac{\partial W_s}{\partial \varepsilon_{G-L}} F_{el}^{\,T} \tag{A.14}$$

where J_{el} is the elastic volume ratio, F_{el} is the elastic deformation gradient tensor, $\varepsilon_{G\text{-}L}$ is the Green-Lagrange strain tensor, and W_s is the elastic strain energy density of the hyperelastic material.

REFERENCES

[Ahm06] K. A. Ahmad, J. L. Drummond, T. Graber, and E. BeGole, "Magnetic strength and corrosion of rare earth magnets," *American Journal of Orthodontics and Dentofacial Orthopedics,* vol. 130, no. 3, pp. 275.e11-275.e15, Sept. 2006.

[Akt09] E. E. Aktakka, H. Kim, and K. Najafi, "Wafer level fabrication of high performance MEMS using bonded and thinned bulk piezoelectric substrates," *International Conference on Solid-State Sensors, Actuators and Microsystems (Transducers),* Denver, CO, June 2009, pp. 849-852.

[Ant12] M. Antelius, A. C. Fischer, F. Niklaus, G. O. R. Stemme, and N. Roxhed, "Hermetic integration of liquids using high-speed stud bump bonding for cavity sealing at the wafer level," *Journal of Micromechanics and Microengineering,* vol. 22, no. 4, p. 045021, Apr. 2012.

[Ant13] M. Antelius, *Wafer-Scale Vacuum And Liquid Packaging Concepts For An Optical Thin-Film Gas Sensor*, Ph.D. dissertation, School of Electrical Engineering, Department of Micro and Nanosystems, KTH Royal Instute of Technology, Stockholm, Sweden, 2013

[Arn80] C. Arnold Jr, K. W. Bieg, and J. A. Coquat, "Degradation of elastomers in geothermal environments," *Geothermal scaling and corrosion, ASTM STP 717*, L. A. Casper and T. R. Pinchback, Eds., American Society for Testing and Materials, 1980, pp. 155-163.

[Asa07] A. B. M. A. Asad, T. Masaki, M. Rahman, H. S. Lim, and Y. S. Wong, "Tool-based micro-machining," *Journal of Materials Processing Technology,* vol. 192–193, no. 0, pp. 204 - 211, 2007.

[Bar76] H. E. Barnes and J. J. Gennari, "A review of pressure-tolerant electronics (PTE)," Naval Research Laboratory, 1976.

[Bea02] W. F. Beach, "Xylylene Polymers," in *Encyclopedia of Polymer Science and Technology*, ed: John Wiley & Sons, Inc., 2002.

[Boy00] M. C. Boyce and E. M. Arruda, "Constitutive Models of Rubber Elasticity: A Review," *Rubber Chemistry and Technology,* vol. 73, pp. 504-523, 2000.

[Car00] D. P. Carlson and W. Schmiegel, "Fluoropolymers, Organic," in *Ullmann's Encyclopedia of Industrial Chemistry*, Weinheim, Germany: Wiley-VCH Verlag GmbH & Co. KGaA, 2000.

[Cha08] J. Chae, J.M. Giachino, K. Najafi, "Fabrication and Characterization of a Wafer-Level MEMS Vacuum Package With Vertical Feedthroughs," *IEEE Journal of Microelectromechanical Systems (JMEMS)*, Vol. 17, Issue 1, pp. 193-200, 02/2008

[Cha12] D. Chapman and W. Trybula, "Meeting the challenges of oilfield exploration using intelligent micro and nano-scale sensors," in *IEEE Conference on Nanotechnology (IEEE-NANO)*, Birmingham, 2012, pp. 1-6.

[Cha15] D. Chapman and W. Trybula, "Autonomous micro and nano sensors for upstream oil and gas," in *Proc. SPIE 9467, Micro- and Nanotechnology Sensors, Systems, and Applications VII*, 2015, p. 94671F.

[Che02] Y. Cheng, W. Hsu, K. Najafi, C. Nguyen, and L. Lin, "Vacuum packaging technology using localized aluminum/silicon-to-glass bonding," *Journal of Microelectromechanical Systems,* vol. 11, no. 5, pp. 556-565, Oct. 2002.

[Cie11] M. Cieślik, K. Engvall, J. Pan, and A. Kotarba, "Silane - parylene coating for improving corrosion resistance of stainless steel 316L implant material," *Corrosion Science,* vol. 53, no. 1, pp. 296-301, Jan. 2011.

[Com13] COMSOL, Nonlinear Structural Materials Module User's Guide, Burlington, MA, USA: COMSOL, Inc., 2013.

[Cos12] S. Costello, M. P. Y. Desmulliez, and S. McCracken, "Review of test methods used for the measurement of hermeticity in packages containing small cavities," *IEEE Transactions on Components, Packaging and Manufacturing Technology,* vol. 2, no. 3, pp. 430-438, Mar. 2012.

[Día11a] B. Díaz, E. Härkönen, J. Światowska, V. Maurice, A. Seyeux, P. Marcus, and M. Ritala, "Low-temperature atomic layer deposition of Al_2O_3 thin coatings for corrosion protection of steel: Surface and electrochemical analysis," *Corrosion Science,* vol. 53, no. 6, pp. 2168-2175, June 2011.

[Día11b] B. Díaz, E. Härkönen, V. Maurice, J. Światowska, A. Seyeux, M. Ritala, and P. Marcus, "Failure mechanism of thin Al_2O_3 coatings grown by atomic layer deposition for corrosion protection of carbon steel," *Electrochimica Acta,* vol. 56, no. 26, pp. 9609-9618, Nov. 2011.

[Dil07] E. H. Dill, *Continuum Mechanics: Elasticity, Plasticity, Viscoelasticity*, Boca Raton, FL, USA: Taylor & Francis Group, LLC, 2007

[Elg04] G. Elger, L. Shiv, N. Nikac, F. Muller, R. Liebe, and M. Grigat, "Optical leak detection for wafer level hermeticity testing," *IEEE/CPMT/SEMI 29th International Electronics Manufacturing Technology Symposium*, July 2004, pp. 326-331.

[Esa08] M. Esashi, "Wafer level packaging of MEMS," *Journal of Micromechanics and Microengineering,* vol. 18, no. 7, p. 073001, 2008.

[Fis90] J. W. Fischer, W. R. Compton, N. A. Jaeger, and D. C. Harris, "Strength of sapphire as a function of temperature and crystal orientation," in *Proc. SPIE 1326, Window and Dome Technologies and Materials II, 11*, 1990, pp. 11-22.

[Geo10] S. M. George, "Atomic layer deposition: an overview," *Polymer,* vol. 110, no. 1, pp. 111-131, 2010.

[Ger01] A. Gerlach, W. Keller, J. Schulz, and K. Schumacher, "Gas permeability of adhesives and their application for hermetic packaging of microcomponents," *Microsystem Technologies,* vol. 7, pp. 17-22, 2001.

[Gil05] K. Gilleo, *MEMS/MOEM Packaging: Concepts, Designs, Materials and Processes*, New York, NY: McGraw Hill Professional, 2005.

[Gub07] F. Gubbels, "Silicones in the Electronics Industries " in *Inorganic Polymers*, R. D. Jaeger and M. Gleria, Eds., Hauppauge, NY: Nova Science Publishers, 2007

[Her00] B. Herzog, M. I. Kohan, S. A. Mestemacher, R. U. Pagilagan, and K. Redmond, "Polyamides," in *Ullmann's Encyclopedia of Industrial Chemistry*, Weinheim, Germany: Wiley-VCH Verlag GmbH & Co. KGaA, 2000.

[Hsu08] T.-R. Hsu, *MEMS & microsystems: design, manufacture, and nanoscale engineering*: John Wiley & Sons, 2008.

[Hyl05] A. Hyldgard, O. Hansen, and E. V. Thomsen, "Fish and chips: single chip silicon MEMS CTDL salinity, temperature, pressure and light sensor for use in fisheries research," in *Micro Electro Mechanical Systems, 2005. MEMS 2005. 18th IEEE International Conference on*, 2005, pp. 303-306.

[Joh14] I. Johnston, D. McCluskey, C. Tan, and M. Tracey, "Mechanical characterization of bulk Sylgard 184 for microfluidics and microengineering," *Journal of Micromechanics and Microengineering,* vol. 24, p. 035017, 2014.

[Kaa06] V. Kaajakari, J. Kiihamäki, A. Oja, S. Pietikäinen, V. Kokkala, and H. Kuisma, "Stability of wafer level vacuum encapsulated single-crystal silicon resonators," *Sensors and Actuators A: Physical,* vol. 130-131, pp. 42-47, 2006.

[Kar98] P. R. Karmel, G. D. Colef, and R. L. Camisa, *Introduction to Electromagnetic and Microwave Engineering,* vol. 53: John Wiley & Sons, 1998.

[Kur68] H. Kurafuji and T. Masuzawa, "Micro-EDM of cemented carbide alloys," *Japan Society of Electrical-Machining Engineers,* vol. 2, no. 3, pp. 1-16, 1968.

[Lap11] M. Lapisa, G. Stemme, and F. Niklaus, "Wafer-Level Heterogeneous Integration for MOEMS, MEMS, and NEMS," *IEEE Selected Topics in Quantum Electronics,* vol. 17, no. 3, pp. 629-644, 2011.

[Lau10] J. H. Lau, C. K. Lee, C. S. Premachandran, and Y. Aibin, *Advanced MEMS Packaging*. New York, NY, USA: McGraw-Hill, 2010.

[Lee93] C. C. Lee, C. Y. Wang, and G. Matijasevic, "Au-In bonding below the eutectic temperature," *IEEE Transactions on Components, Hybrids, and Manufacturing Technology,* vol. 16, no. 3, pp. 311-316, May 1993.

[Lee09] S. Lee, "Wafer-level packaging for environment-resistant micro-instruments," Ph.D. dissertation, Univ. Michigan, An Arbor, MI, USA, 2009.

[Lee10] S.-H. Lee, J. Mitchell, W. Welch, S. Lee, and K. Najafi, "Wafer-level vacuum/hermetic packaging technologies for MEMS," *Proc. SPIE 7592: Reliability, Packaging, Testing, and Characterization of MEMS/MOEMS and Nanodevices IX*, San Francisco, CA, Jan. 2010, p. 759205.

[Lee13] J.-Y. Lee, S.-W. Lee, S.-K. Lee, and J.-H. Park, "Through-glass copper via using the glass reflow and seedless electroplating processes for wafer-level RF MEMS packaging," *Journal of Micromechanics and Microengineering,* vol. 23, p. 085012, 2013.

[Li06] T. Li and Y. B. Gianchandani, "A micromachining process for die-scale pattern transfer in ceramics and its application to bulk piezoelectric actuators," *Journal of Microelectromechanical Systems,* vol. 15, no. 3, pp. 605-612, 2006.

[Li08] W. Li, D. Rodger, P. Menon, and Y. Tai, "Corrosion Behavior of Parylene-Metal-Parylene Thin Films in Saline," *ECS Transactions,* vol. 11, no. 18, pp. 1-6, 2008.

[Li09] T. Li, "Ultrasonic batch mode micromachining and its application to piezoelectric sensors for fine needle aspiration biopsy," Ph.D. dissertation, University of Michigan, 2009.

[Li10] T. Li and Y. B. Gianchandani, "A high-speed batch-mode ultrasonic machining technology for multi-level quartz crystal microstructures," in *IEEE International Conference on Micro Electro Mechanical Systems (MEMS)*, Wanchai, Hong Kong, Jan. 2010, pp. 348-351.

[Li12] T. Li, K. Ding, W. Seyfried, and Y. B. Gianchandani, "A micromachined chemical sensor for sea floor environments: initial results," in *Hilton Head 2012: Solid State Sensor, Actuator and Microsystems Workshop (Hilton Head Island, SC,)*, 2012, pp. 173-6.

[Li13] T. Li, Q. Bai, and Y. B. Gianchandani, "High precision batch mode micro-electro-discharge machining of metal alloys using DRIE silicon as a cutting tool," *Journal of Micromechanics and Microengineering,* vol. 23, no. 9, p. 095026, 2013.

[Luo14] X. Luo, C. K. Eun, and Y. B. Gianchandani, "Fabrication of a monolithic microdischarge-based pressure sensor for harsh environments," *IEEE International Conference on Micro Electro Mechanical Systems (MEMS)*, San Francisco, Jan. 2014, pp. 64-67.

[Ma14] Y. Ma, Y. Sui, T. Li, and Y. B. Gianchandani, "A Submillimeter Package for Microsystems in High-Pressure and High-Salinity Downhole Environments," *Journal of Microelectromechanical Systems,* vol. 24, pp. 861-869, 2015.

[Mar78] R. A. Marquardt, "Five-Year Life Test Data on Pressure (10 000 lbf/in 2) Tolerant Electronic Components," *IEEE Transactions on Components, Hybrids, and Manufacturing Technology,* vol. 1, pp. 365-371, 1978.

[Mar06] P. Martins, R. Natal Jorge, and A. Ferreira, "A Comparative Study of Several Material Models for Prediction of Hyperelastic Properties: Application to Silicone‐Rubber and Soft Tissues," *Strain,* vol. 42, pp. 135-147, 2006.

[Mas90] T. Masaki, K. Kawata, and T. Masuzawa, "Micro electro-discharge machining and its applications," *Proc. IEEE Micro Electro Mechanical Systems: An Investigation of Micro Structures, Sensors, Actuators, Machines and Robots*, Napa Valley, CA, Feb. 1990, pp. 21-26.

[Meu08] L. Meunier, G. Chagnon, D. Favier, L. Orgéas, and P. Vacher, "Mechanical experimental characterisation and numerical modelling of an unfilled silicone rubber," *Polymer Testing,* vol. 27, pp. 765-777, 2008.

[Mor03] M. Moraja, M. Amiotti, and R. C. Kullberg, "New getter configuration at wafer level for assuring long term stability of MEMs," *Proc. SPIE: Reliability, Testing, and Characterization of MEMS/MOEMS II*, San Jose, CA, Jan. 2003, pp. 260-267.

[Mil09] S. Millar and M. Desmulliez, "MEMS ultra low leak detection methods: a review," *Sensor Review,* vol. 29, no. 4, pp. 339-344, 2009.

[Min89] M. L. Minges, *Electronic Materials Handbook: Volume 1, Packaging*, ASM international, 1989.

[Mit09] J. S. Mitchell and K. Najafi, "A detailed study of yield and reliability for vacuum packages fabricated in a wafer-level Au-Si eutectic bonding process," *International Conference on Solid-State Sensors, Actuators and Microsystems (Transducers)*, June 2009, pp. 841-844.

[Mur09] S. Murashige, S. Yamamoto, T. Shiojiri, S. Mitani, T. Suzuki, and M. Hashimoto, "Ultra-small absolute pressure sensor using WLP," *Fujikura Technical Review*, no. 38, pp. 65-70, 2009.

[Naj03] K. Najafi, "Micropackaging technologies for integrated microsystems: Applications to MEMS and MOEMS," in *SPIE Micromachining and Microfabrication*, San Jose, CA, 2003, pp. 1-19.

[Naj07] K. Najafi, "Packaging of Implantable Microsystems," in *Proceedings of IEEE SENSORS*, Atlanta GA, 2007, pp. 58-63.

[Nol68] W. Noll, Chemistry and Technology of Silicones, New York and London: Academic Press Inc, 1968

[Pau61] W. Paul, "Band Structure of the Intermetallic Semiconductors from Pressure Experiments," *Journal of Applied Physics,* vol. 32, pp. 2082-2094, 1961.

[Pot11] S. E. Potts, L. Schmalz, M. Fenker, B. Díaz, J. Światowska, V. Maurice, A. Seyeux, P. Marcus, G. Radnóczi, L. Tóth, and W. M. M. Kessels, "Ultra-Thin Aluminium Oxide Films Deposited by Plasma-Enhanced Atomic Layer Deposition for Corrosion Protection," *Journal of The Electrochemical Society,* vol. 158, no. 5, pp. C132-C138, Mar. 2011.

[Sai91] S. B. Saidman and J. B. Bessone, "Anodic behaviour of indium in sodium chloride solutions," *Electrochimica Acta,* vol. 36, no. 14, pp. 2063-2067, 1991.

[Shi99] F. S. Shieu, C. F. Chen, J. G. Sheen, and Z. C. Chang, "Intermetallic phase formation and shear strength of a Au-In microjoint," *Thin Solid Films,* vol. 346, no. 1‑2, pp. 125-129, June 1999.

[Shi15] Z. Shi, Y. Chen, M. Yu, S. Zhou, and N. Al-Khanferi, "Development and Field Evaluation of a Distributed Microchip Downhole Measurement System," in *SPE Digital Energy Conference and Exhibition*, 2015.

[Ski04] N. G. Skinner and J. J. L. Maida, "Downhole fiber optic sensing: the oilfield service provider's perspective," *Proc. SPIE 5589, Fiber Optic Sensor Technology and Applications III*, Philadelphia, PA, Oct. 2004, pp. 206-220.

[Smi73] A. Smith, S. J. Wilkinson, and W. N. Reynolds, "The elastic constants of some epoxy resins," *Journal of Materials Science,* vol. 9, pp. 547-550, 1974.

[So00] W. W. So and C. C. Lee, "Fluxless process of fabricating In-Au joints on copper substrates," *IEEE Transactions on Components and Packaging Technologies,* vol. 23, no. 2, pp. 377-382, June 2000.

[Soh07] Y. Sohn, Q. Wang, S. Ham, B. Jeong, K. Jung, M. Choi, W. Kim, and C. Moon, "Wafer-level low temperature bonding with Au-In system," *Proc. Electronic components and technology conference (ECTC)*, Reno, NV, May 2007, pp. 633-637.

[Str11] R. Straessle, Y. Pétremand, D. Briand, and N. F. de Rooij, "Evaluation of Thin Film Indium Bonding at Wafer Level," *Procedia Engineering,* vol. 25, pp. 1493-1496, 2011.

[Tak02] K. Takahata and Y. B. Gianchandani, "Batch mode micro-electro-discharge machining," *Journal of Microelectromechanical Systems,* vol. 11, no. 2, pp. 102-110, 2002.

[Tao05] Y. Tao and A. P. Malshe, "Theoretical investigation on hermeticity testing of MEMS packages based on MIL-STD-883E," *Microelectronics Reliability,* vol. 45, no. 3-4, pp. 559-566, Mar.-Apr. 2005.

[Tim87] S. Timoshenko and S. Woinosky-Krieger, *Theory of Plates and Shells*, 6th ed., New York: McGraw Hill, 1987.

[Tsu01] T. Tsuchiya, Y. Kageyama, H. Funabashi, and J. Sakata, "Polysilicon vibrating gyroscope vacuum-encapsulated in an on-chip micro chamber," *Sensors and Actuators A: Physical,* vol. 90, no. 1-2, pp. 49-55, May 2001.

[Tum01] R. R. Tummala, *Fundamentals of Microsystems Packaging*, McGraw-Hill: New York, 2001.

[Vey05] D. Veyrie, D. Lellouchi, J. L. Roux, F. Pressecq, A. E. L. Tetelin, and C. Pellet, "FTIR spectroscopy for the hermeticity assessment of micro-cavities," *Microelectronics Reliability,* vol. 45, no. 9-11, pp. 1764-1769, Sept.-Nov. 2005.

[Web97] W. H. Weber, M. Zanini-Fisher, and M. J. Pelletier, "Using Raman microscopy to detect leaks in micromechanical silicon structures," *Applied Spectroscopy,* vol. 51, no. 1, pp. 123-129, 1997.

[Web-Acc] *Aluminum Oxide Al₂O₃ Ceramic Properties,*

http://accuratus.com/alumox.html, Accessed Aug. 2016

[Web-All] *Alloy Specifications*, http://www.hpmetals.com/metals-alloys/comparative-data.aspx, Accessed Jan. 2015.

[Web-Alu] *Aluminum / Aluminium 3003 Alloy (UNS A93003)*, http://www.azom.com/article.aspx?ArticleID=6618, Accessed Jan. 2015.

[Web-Che] *Chemical Compatibility Database,* http://www.coleparmer.com/Chemical-Resistance, Accessed Sept. 2016.

[Web-Dup] *Kapton Summary of Properties,* http://www.dupont.com/content/dam/dupont/products-and-services/membranes-and-films/polyimde-films/documents/DEC-Kapton-summary-of-properties.pdf, Accessed Aug. 2016

[Web-Dup2] *DuPont FEP Fluorocarbon Film Properties Bulletin*, http://americandurafilm.com/data-sheets/fep-properties.pdf, Accessed Sept. 2016

[Web-Cha] *Characteristic Properties of Silicone Rubber Compounds*, http://www.shinetsusilicone-global.com/catalog/pdf/rubber_e.pdf, Accessed Aug. 2016

[Web-Che] *Chemical Compatibility,* http://www.spectrumlabs.com/dialysis/Compatibility.html, Accessed Sept. 2016

[Web-Far] S. Farrens, *Metal based wafer bonding techniques for wafer level packaging,* http://www.suss.com/fileadmin/user_upload/technical_publications/WP_Metal_Based_Wafer_Bonding_Techniques_for_Wafer_Level_Packaging_1209.pdf, Accessed Nov. 2014."

[Web-Hyd] SMT Learning Channel, *Hydraulic Fracturing- Shale Natural Gas Extraction,* https://www.youtube.com/watch?v=lB3FOJjpy7s, Accessed Aug. 2016

[Web-Pla] *Plastics – Chemical Resistance Chart*, http://www.professionalplastics.com/professionalplastics/ChemicalResistanceChartofPlastics.pdf, Accessed Sept. 2016.

[Web-Pol] *Polyethersulfone (PES) Film Material Information,* http://www.goodfellow.com/A/Polyethersulfone-Film.html, Accessed Sept. 2016

[Web-Sil] *Silicone Rubber*, http://www.azom.com/properties.aspx?ArticleID=920, Accessed Aug. 2016

[Web-Sma] *SmalTec EM203 Micro EDM Machine*, http://www.smaltec.com/resources/SmalTec_EM203_Specs.pdf, Accessed Nov. 2014.

[Web-Sta] *Stainless Steel - Grade 304 (UNS S30400)*, http://www.azom.com/article.aspx?ArticleID=965, Accessed Aug. 2016

[Web-Wat] *Water Saturation Pressure*, http://www.engineeringtoolbox.com/water-vapor-saturation-pressure-d_599.html, Accessed Oct. 2016

[Wel08] W. C. Welch and K. Najafi, "Gold-indium Transient Liquid Phase (TLP) wafer bonding for MEMS vacuum packaging," *IEEE International Conference on Micro Electro Mechanical Systems (MEMS)*, Tucson, AZ, Jan. 2008, pp. 806-809.

[Wij11] M. Wijesundara and R. Azevedo, *Silicon carbide microsystems for harsh environments* vol. 22: Springer Science & Business Media, 2011.

[Wis09] K. D. Wise, "Wireless integrated microsystems: Wearable and implantable devices for improved health care," *International Conference on Solid-State Sensors, Actuators and Microsystems (Transducers)*, Denver, CO, 2009, pp. 1-8.

[Xie12] X. Xie, L. Rieth, S. Merugu, P. Tathireddy, and F. Solzbacher, "Plasma-assisted atomic layer deposition of Al_2O_3 and parylene C bi-layer encapsulation for chronic implantable electronics," *Applied Physics Letters,* vol. 101, no. 9, p. 093702, Aug. 2012.

[Xie13] X. Xie, L. Rieth, P. Tathireddy, and F. Solzbacher, "Atomic layer deposited Al2O3 and parylene C dual-layer encapsulation for biomedical implantable devices," *International Conference on Solid-State Sensors, Actuators and Microsystems (Transducers & Eurosensors XXVII)*, Barcelona, June 2013, pp. 1044-1047.

[Yao95] J. J. Yao and M. F. Chang, "A Surface Micromachined Miniature Switch For Telecommunications Applications With Signal Frequencies From DC Up To 4 Ghz," in *The 8th International Conference on Solid-State Sensors and Actuators, 1995 and Eurosensors IX.. (Transducers '95)*, 1995, pp. 384-387.

[Yaz98] N. Yazdi, F. Ayazi, and K. Najafi, "Micromachined inertial sensors," *Proceedings of the IEEE,* vol. 86, no. 8, pp. 1640-1659, Aug. 1998.

[Yu12] M. Yu, S. He, Y. Chen, N. Takach, P. LoPresti, S. Zhou*, et al.*, "A distributed microchip system for subsurface measurement," in *SPE Annual Technical Conference and Exhibition*, 2012.

[Zos14] K. Zoschke, M. Wilke, M. Wegner, K. Kaletta, C. A. Manier, H. Oppermann*, et al.*, "Capping technologies for wafer level MEMS packaging based on permanent and temporary wafer bonding," *IEEE Electronic Components and Technology Conference (ECTC)*, Orlando, FL, May 2014, pp. 1204-1211.